

MIIKA SORVALI

# Crystallographic Phase Control of Iron Oxide Particles in Liquid Flame Spray and Utilization of Nanoparticles in Applications



MIIKA SORVALI

Crystallographic Phase Control  
of Iron Oxide Particles in Liquid Flame Spray  
and Utilization of Nanoparticles in Applications

ACADEMIC DISSERTATION

To be presented, with the permission of  
the Faculty of Engineering and Natural Sciences  
of Tampere University,  
for public discussion in the Auditorium S203 (S2)  
of the Sähköotalo Building, Korkeakoulunkatu 3, 33720 Tampere,  
on the 12<sup>th</sup> of October 2021, at 12 o'clock.

ACADEMIC DISSERTATION

Tampere University, Faculty of Engineering and Natural Sciences  
Finland

<i>Responsible supervisor and Custos</i>	Professor Jyrki Mäkelä Tampere University Finland	
<i>Pre-examiners</i>	Professor Knut Deppert Lund University Sweden	Professor Esko Kauppinen Aalto University Finland
<i>Opponent</i>	Associate Professor Anna Lähde University of Eastern Finland Finland	

The originality of this thesis has been checked using the Turnitin OriginalityCheck service.

Copyright ©2021 author

Cover design: Roihu Inc.

ISBN 978-952-03-2177-2 (print)

ISBN 978-952-03-2178-9 (pdf)

ISSN 2489-9860 (print)

ISSN 2490-0028 (pdf)

<http://urn.fi/URN:ISBN:978-952-03-2178-9>

PunaMusta Oy – Yliopistopaino  
Joensuu 2021



# Abstract

Nanotechnology has become a very important branch of research and industry especially during this millenium, and it keeps growing constantly. Simultaneously, demand for large volumes of quality nanomaterial is increasing. Flame spray pyrolysis (FSP) is one of the most promising fabrication methods for inexpensive and simple large-scale production. However, the details of the synthesis process still remain reasonably poorly understood. Liquid flame spray (LFS), a certain type FSP method, was chosen as the focal point of this dissertation. Because both the knowledge on the synthesis process and utilization of LFS in applications are essential for capitalizing on its the strengths in the long term, half of this dissertation was dedicated to improving the understanding of the process, and the other half for exploring its potential in two distinct applications.

In the first part, factors determining the crystallographic phase composition of iron oxide particles in LFS synthesis was studied. The synthesis yielded maghemite ( $\gamma\text{-Fe}_2\text{O}_3$ ) and hematite ( $\alpha\text{-Fe}_2\text{O}_3$ ), and the equivalence ratio was found as the best measure for predicting their ratio. However, the correlation between the phase ratio and the equivalence ratio was observed to differ between different experimental setups. Modifying the precursor solution through mixed solvents or additives also had a clear effect on the phase composition, which indicates that the solution chemistry likely has unknown effects on the process.

The first of the two applications was bidisperse magnetorheological (MR) fluids, where LFS-made nanoparticles were added to a more traditional MR fluid to counteract sedimentation. The addition reduced the sedimentation rate considerably without impairing its performance. The second application was a liquid-repellent nanocoating consisting of a nanoparticle layer produced with LFS, an ALD mid layer, and a topmost silane layer. The ultrathin final coating repelled several test liquids effectively, but possessed lower stability than initially hoped.



# Preface

Most of the research in this thesis was conducted during 2016-2021 in the Aerosol Physics Laboratory at Tampere University (Tampere University of Technology until 2019), with some preliminary work was performed earlier. The primary funding came from TUT graduate school, but also Tekes, Academy of Finland, the Jenny and Antti Wihuri Foundation, and the companies that participated in the DIMECC HYBRIDS program are acknowledged for financial support.

First, I want to thank my supervisor, Prof. Jyrki Mäkelä, who took me into the synthesis group as a young summer student. He has helped me in various aspects of research work and given me lots of freedom to find my own way. The pre-examiners Prof. Knut Deppert and Prof. Esko Kauppinen I wish to thank for valuable comments. I am also grateful to Prof. Jorma Keskinen for guiding me in teaching that offered a great counterbalance for research. I thank Mr. Janne Haapanen for teaching me the basics of lab work. Dr. Mari Honkanen and Mr. Leo Hyvärinen deserve my gratitude for characterizing samples for most of my publications. Special thanks go to Dr. Paxton Juuti, with whom I worked together and shared an office for a long time, and who was always ready to discuss any topic and offer assistance. Help of every other co-author was also invaluable for compiling this thesis. Co-workers who haven't directly contributed to my research also deserve recognition for making the atmosphere as uplifting and motivating as I have experienced it. It's been a pleasure.

I want to thank my parents for giving me all the tools in life and the boundless support for whatever I wanted to do. To all of my friends and relatives, I want to express my gratitude for bringing loads of meaningful things in my life. Lastly, I thank my girlfriend Roosa, who has made the latter part of my doctoral studies very joyful and the future look especially bright.

Tampere, August 2021

*Miika Sorvali*



# Contents

<b>Abstract</b>	<b>iii</b>
<b>Preface</b>	<b>v</b>
<b>Symbols and abbreviations</b>	<b>viii</b>
<b>List of publications</b>	<b>xi</b>
<b>Author's contributions</b>	<b>xiv</b>
<b>1 Introduction</b> .....	<b>1</b>
1.1 Research goals and the scope of the thesis .....	2
<b>2 Nanomaterials and their applications</b> .....	<b>5</b>
2.1 Iron oxide .....	5
2.2 Magnetorheological fluids .....	6
2.3 Liquid-repelling surfaces .....	7
<b>3 Flame spray synthesis and additional coating methods</b> .....	<b>11</b>
3.1 Liquid flame spray process .....	11
3.2 Particle formation process .....	14
3.2.1 Atomization & combustion mode .....	16
3.2.2 Flame temperature .....	18
3.2.3 Equivalence ratio .....	19
3.2.4 Residence time .....	20
3.2.5 Gaseous end product concentration .....	20
3.2.6 Chemical processes .....	21
3.3 Atomic layer deposition .....	22
3.4 Silanization .....	24

---

<b>4</b>	<b>Characterization methods</b> .....	<b>25</b>
4.1	Structural and surface characterization.....	25
4.2	MR fluid characterization .....	28
4.3	Surface properties analysis .....	29
<b>5</b>	<b>Results and discussion</b> .....	<b>31</b>
5.1	Controlling the particle formation process in LFS synthesis .....	31
5.1.1	Pure alcohols as solvents .....	32
5.1.2	Modifying the composition of the precursor solution .....	40
5.2	MR fluids .....	45
5.2.1	Nanoparticle synthesis and characterization.....	45
5.2.2	Sedimentation behaviour and MR performance .....	46
5.3	Omniphobic nanocoating.....	48
5.3.1	Characterization of the coating.....	50
5.3.2	Assessment of omniphobicity and stability .....	52
<b>6</b>	<b>Concluding remarks</b> .....	<b>55</b>
	<b>References</b> .....	<b>59</b>
	<b>Publication I</b> .....	<b>69</b>
	<b>Publication II</b> .....	<b>83</b>
	<b>Publication III</b> .....	<b>95</b>
	<b>Publication IV</b> .....	<b>107</b>

# Symbols and abbreviations

$A_{Pr}$	The area a droplet projects on a surface
$A_{SL}$	The actual contact area between a droplet and a surface
$G$	Group combustion number
$G'$	Storage modulus
$G''$	Loss modulus
$R_c$	Droplet cloud radius
$Re$	Reynolds number
$T_{bp}$	Boiling point of solvent
$T_{d/mp}$	Decomposition/melting temperature of precursor
$U_R$	Relative velocity between gas and liquid
$We$	Weber number
$\Phi$	Equivalence ratio
$\delta$	Phase shift
$\dot{\gamma}_R$	Shear rate
$\dot{m}_g$	Mass flow rate of gas
$\dot{m}_l$	Mass flow rate of liquid
$\eta_p$	Plastic viscosity
$\gamma_o$	Strain amplitude
$\gamma_{LV}$	Surface energy of a liquid-vapor interface
$\gamma_{SL}$	Surface energy of a solid-liquid interface
$\gamma_{SV}$	Surface energy of a solid-vapor interface

---

$\lambda$	Wavelength
$\mu_L$	Viscosity of liquid
$\rho_L$	Density of liquid
$\sigma$	Surface tension
$\sigma(n)$	Droplet number density
$\tau_R$	Dynamic yield stress
$\tau_o$	Stress response
$\tau_y$	Yield stress
$\theta_W$	Apparent contact angle defined by Wenzel equation
$\theta_Y$	Intrinsic contact angle defined by Young's equation
$\theta_{CB}$	Apparent contact angle defined by Cassie-Baxter equation
$d_0$	Diameter of the liquid channel
$d_d$	Average droplet diameter
$f_{SL}$	The fraction of the solid-liquid interface from the whole interface underneath the droplet in a heterogeneous wetting state
$n_{fuel}$	The amount of substance of combustible molecules
$n_{oxygen}$	The amount of substance of oxygen molecules
ALD	Atomic layer deposition
BET	Brunauer-Emmett-Teller
ButA	Butanoic acid
CA	Contact angle
CI	Carbonyl iron
CitA	Citric acid
CVD	Chemical vapor deposition
DIM	Diiodomethane
EDS	Energy-dispersive x-ray spectroscopy
EELS	Electron energy loss spectroscopy
EG	Ethylene glycol



---

EHA	2-ethylhexanoic acid
ESP	Electrostatic precipitator
EtOH	Ethanol
FIB	Focused ion beam
FSP	Flame spray pyrolysis
HDF	(heptadecafluoro-1,1,2,2-tetrahydrodecyl) trichlorosilane
HOC	Heat of combustion
IPA	Isopropyl alcohol
LFS	Liquid flame spray
MeOH	Methanol
MR	Magnetorheological
OO	Olive oil
OxA	Oxalic acid
PP	Primary particle
PropA	Propanoic acid
SA	Sliding angle
SEM	Scanning electron microscope
slpm	Standard liters per minute (used as a synonym for l/min)
SMD	Sauter mean diameter
SSA	Specific surface area
TEM	Transmission electron microscope
XPS	X-ray photoelectron spectroscopy
XRD	X-ray diffraction



# List of publications

- Publication I** Sorvali, M., Nikka, M., Juuti, P., Honkanen, M., Salminen, T., Hyvärinen, L. and Mäkelä, J. M. (2019). Controlling the phase of iron oxide nanoparticles fabricated from iron(III) nitrate by liquid flame spray. *International Journal of Ceramic Engineering and Science* 1.4, 194–205. DOI: 10.1002/ces2.10025.
- Publication II** Sorvali, M., Honkanen, M., Hyvärinen, L., Kuisma, R., Larjo, J. and Mäkelä, J. M. (2021). Crystallographic phase formation of iron oxide particles produced from iron nitrate by liquid flame spray with a dual oxygen flow. *International Journal of Ceramic Engineering and Science* 3.5, 227–236. DOI: 10.1002/ces2.10102.
- Publication III** Jönkkäri, I., Sorvali, M., Huhtinen, H., Sarlin, E., Salminen, T., Haapanen, J., Mäkelä, J. M. and Vuorinen, J. (2017). Characterization of bidisperse magnetorheological fluids utilizing maghemite ( $\gamma\text{-Fe}_2\text{O}_3$ ) nanoparticles synthesized by flame spray pyrolysis. *Smart Materials and Structures* 26, 095004. DOI: 10.1088/1361-665X/aa7f7d.
- Publication IV** Sorvali, M., Vuori, L., Pudas, M., Haapanen, J., Mahlberg, R., Ronkainen, H., Honkanen, M., Valden, M. and Mäkelä, J. M. (2018). Fabrication of ultrathin multilayered superomniphobic nano-coatings by liquid flame spray, atomic layer deposition, and silanization. *Nanotechnology* 29, 185708. DOI: 10.1088/1361-6528/aaaffc.

## *Author's contribution*

The author's contributions to each publication are described below.

- Publication I**      The author planned most of the study, wrote almost the whole article and was responsible for the figures. The nanoparticle synthesis and the particle collection was carried out by the author. He also did all the sample preparation for analyses, and was mainly responsible for analyzing the data. Paxton Juuti and Markus Nikka assisted in the synthesis process. Mari Honkanen performed TEM imaging, Turkka Salminen Raman microscopy, and Leo Hyvärinen XRD measurements.
- Publication II**      The author planned most of the study, wrote almost the whole article and was responsible for the figures. The nanoparticle synthesis and the particle collection was carried out by the author. He also did all the sample preparation for analyses, and was mainly responsible for analyzing the data. Mari Honkanen performed TEM imaging, Leo Hyvärinen XRD measurements, Ritva Kuisma BET measurements, and Jussi Larjo the atomization measurements.
- Publication III**      The author planned the nanoparticle synthesis process, and produced the nanopowders. He also assisted in writing the article. Ilari Jönkkäri was responsible for planning the research and performing the rheological experiments. Hannu Huhtinen was responsible for measuring the magnetic properties of the particles. Essi Sarlin was responsible the TEM images and Turkka Salminen for the Raman spectroscopy.
- Publication IV**      Most of the article was written by the author and he was responsible for the figures. The author participated in planning the whole fabrication process and was mainly responsible for the

nanoparticle synthesis and coating. He also analyzed most of the measurement data in collaboration with others. Janne Haapanen assisted in the LFS coating process. Leena Vuori performed silanization, the contact angle measurements and the XPS measurements. Marko Pudas produced the ALD coatings. Mari Honkanen was responsible for SEM imaging, and Ritva Kuisma for the microscratch experiments.



# 1 Introduction

Nanotechnology has been one of the most rapidly growing research and industrial branches during the last few decades. It has spread to almost every industrial field and shows no signs of slowing down. It exceeded a market value of one trillion dollars in 2014, according to international reports (Emashova et al. 2016; Roco 2011). Already in 2001, volumes in the order of 100 metric tons per day were produced worldwide (Kammler et al. 2001). A large advantage arising with nanomaterials is obtaining new properties from familiar base materials by decreasing their physical size, thus simultaneously lowering the material volumes needed.

Due to the continuously increasing demand for high-quality nanomaterials, the production volume and costs are becoming more and more important. Since different fabrication methods offer their own advantages, it can often be difficult to find the best alternative for a specific purpose. If a precisely controlled material is required, but only in small amounts, one from the plethora of chemical methods might prove to be the optimal choice. (Makhlouf and Tiginyanu 2011) However, if large volumes are needed, flame synthesis is one of the more promising alternatives, since it can provide fast and simple production in large scale, and exploit relatively abundant and cheap source materials (Mueller et al. 2003; Teoh et al. 2010). It also produces no liquid waste on the side that is challenging to dispose of, which tends to be problematic for especially wet chemical methods.

Flame spray pyrolysis (FSP) is one of the most interesting flame methods, because it can utilize a wide range of inexpensive precursors and solvents in liquid form (Strobel and Pratsinis 2011). Vapor-fed flame burners are efficient in producing some homogeneous nanomaterials, but precursor gases are usually expensive and offer a very limited selection. They are also not well-suited for producing homogeneous multicomponent materials due to differences in vapor pressures and reaction rates of the reactant gases. (Mueller et al. 2003) FSP, on the other hand, enables simple synthesis by mixing precursors and solvents conveniently into a single solution. With

adequate knowledge of the process, even complex materials can be produced. Liquid flame spray (LFS) is a specific type of FSP reactor developed at Tampere University of Technology, and was chosen as the central synthesis method for this dissertation.

Due to the complexity of the particle formation process and the difficulty of performing precise mid-process measurements, the understanding of the whole picture in FSP synthesis is still far from complete. This can make it less appealing for nanomaterial producers to choose flame synthesis, if relatively strict control of material properties is demanded. As long as there are significant gaps in understanding and computers are unable to perform extensive simulations, experimental research is essential. Half of this dissertation was dedicated to expanding the knowledge on the factors that govern the synthesis process in a specific case. The current state of research on the topic along with a more in-depth analysis of the synthesis process will be discussed in Chapter 3.

Along with research that strives for theoretical understanding, applications utilizing FSP-generated nanomaterials should be studied, because therein lies the final goal. For this dissertation, two distinct applications were chosen: magnetorheological (MR) fluids and liquid-repellent coatings, both utilizing LFS in the fabrication process. Plenty of research has already been conducted on these topics, but a lot to develop still remains. The existing literature will be explored, and it will be assessed how our studies relate to it.

## 1.1 Research goals and the scope of the thesis

The aim of this thesis is to improve the understanding of the flame synthesis process and the factors that impact the resulting material. It also strives to explore the possibilities of utilizing LFS in nanomaterial-based applications by studying two distinct topics. The objectives for this thesis are:

- Enhancing understanding on the factors determining the crystallographic phase of iron oxide particles in flame synthesis
- Studying other variables that are connected to the phase formation, and other particle properties
- Exploring the use of LFS-generated magnetic nanoparticles in magnetorheological fluids



- Producing a liquid-repellent nanocoating on stainless steel utilizing LFS

In **Publication I**, iron oxide nanoparticles were produced from iron nitrate with LFS. The effect of varying either gas flows or the composition of precursor solution on the crystallographic phase was studied. In **Publication II**, the analysis was taken further by modifying the experimental setup to allow a more flexible gas flow configuration and experimenting with two different additives in the precursor solution. Other particle properties and factors associated with changes in phase composition were also studied.

In **Publication III**, magnetic nanoparticles were produced with LFS and used in bidisperse MR fluids. The effect of the particle properties on the MR fluid performance was assessed by measuring sedimentation rate, magnetic response and viscosity. A multilayered omniphobic coating was produced on a steel surface in **Publication IV**. It consisted of three layers: a nanoparticle layer produced with LFS, a stabilizing middle layer produced with atomic layer deposition, and a top layer of silane molecules to lower the surface energy. The coating was characterized and its liquid-repellency and stability were analyzed.



# 2 Nanomaterials and their applications

The whole range of nanoparticle applications is extremely broad, so only a few will be mentioned. In this chapter, two application areas that are most relevant to this dissertation will be covered. Because the process control part of the dissertation concentrates on synthesis of iron oxide, it will first be discussed separately as a nanomaterial.

## 2.1 Iron oxide

Iron oxide is an interesting material due to its nontoxicity and versatility. There are four main crystallographic phases in which it mostly occurs: wüstite ( $\text{FeO}$ ), hematite ( $\alpha\text{-Fe}_2\text{O}_3$ ), maghemite ( $\gamma\text{-Fe}_2\text{O}_3$ ) and magnetite ( $\text{Fe}_3\text{O}_4$ ). (Teja and Koh 2009; W. Wu, He et al. 2008) Also some rarer ones have been discovered, but their potential has only been studied to a limited extent (Brázda et al. 2018; Sakurai et al. 2009). Hematite, maghemite and magnetite are the three most relevant phases regarding applications, so the focus will fall on them.

Hematite is an *n*-type semiconductor with a rhombohedral crystal structure (W. Wu, Z. Wu et al. 2015). It is also the most stable phase of the three, as magnetite and maghemite will go through a phase transformation into hematite when treated at an adequately high temperature (Haneda and Morrish 1977; Khan et al. 2015). However, the other two phases can also be obtained from hematite by a reducing treatment (Gao et al. 2020). Hematite particles are commonly used in red pigments, gas sensors (Dutt et al. 2020; Wei et al. 2020) and catalytic applications (S. Li, Hu et al. 2017; Tamirat et al. 2016), among other fields (W. Wu, Z. Wu et al. 2015). One of the most interesting uses where hematite has lately been linked to is photocatalytic

water-splitting by visible light (Katz et al. 2012; Rohilla and Ingole 2021; Tamirat et al. 2016).

Magnetite and maghemite are quite similar in their properties. They both have a cubic unit cell, but at least for maghemite, there seems to be some variation in the exact structure, as multiple structure models have been reported (Jørgensen et al. 2007; Pecharromán et al. 1995; Solano et al. 2014). Both phases are also ferrimagnetic, but magnetite is usually regarded as magnetically a little stronger. On the other hand, magnetite is the less stable of the two, and can relatively easily transform into maghemite (Haneda and Morrish 1977; Hanesh 2009). Maghemite can be considered an oxidized form of magnetite, since magnetite contains both divalent and trivalent ferric ions, and maghemite only trivalent ones.

Much of the application potential of these two phases lies with their magnetic properties, which will be elaborated in the next section, although they have also been used in, e.g., lithium-ion batteries and gas sensors (Wang et al. 2018). Magnetic properties of particles offer potential uses for various applications, medical research being one of the fields taking advantage of magnetic nanoparticles. They can be used for targeted drug delivery by loading the particles with specific molecules, and magnetically guiding them to the intended location (Cao et al. 2008; Ong et al. 2020). This could, for example, help reduce the adverse effects of chemotherapy in cancer patients. Other medical applications include magnetic resonance imaging (Nosrati et al. 2019) and hyperthermia (Usov 2019). Magnetic nanoparticles have also been used in microfluidic systems (Gijs et al. 2010; Hsu et al. 2018), but the most relevant application branch for this dissertation is magnetorheological fluids, so a closer look will be taken at them.

## **2.2 Magnetorheological fluids**

Magnetorheological (MR) fluids are usually liquid suspensions composed of a non-magnetizable liquid and magnetizable particles. When an external magnetic field is applied on the fluid, the particles magnetize and their induced magnetic dipole moments align, forming chains that resist liquid flow, as described in Figure 2.1. This causes a sudden rise in viscosity. (Bossis et al. 2002; Vicente et al. 2011) Vehicle industry is an example of a field that could benefit from using these types of fluids in brakes.

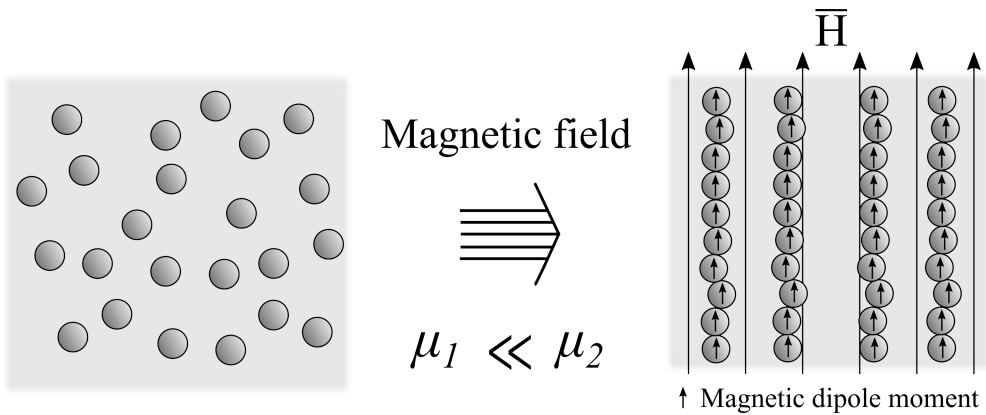


**Figure 2.1** The working principle of an MR fluid.  $\mu$  refers to the viscosity of the fluid.

Traditionally the particles are in the micron range in size, because larger particles provide stronger magnetization compared to nanoparticles, and therefore an enhanced response (Chaudhuri et al. 2005). However, a common problem with particles in the micron range is their fast sedimentation due to gravitational settling. If the particles form a rigid enough sediment, they cannot detach and form chains after reintroduction of the magnetic field. One possible solution to this problem is substituting the micron-sized particles with nanoparticles that do not settle on the bottom. This would, however, result in a much weaker MR response.

A compromise between these two instances can be met with so-called bidisperse MR fluids, where only a small portion of the larger particles is substituted with nanoparticles. This counteracts the sedimentation, simultaneously preserving most of the MR response or even improving it. (Chin et al. 2001; Ngatu and Wereley 2007; Wereley et al. 2006)

## 2.3 Liquid-repelling surfaces

Nanocoatings is one of the large branches of nanotechnology, encompassing thin films up to 100 nm in thickness, but also thicker layers with embedded nanostructures (Aliofkhazraei 2011). Some nanocoatings are applied just for decoration, but often some functionality that emerges from the nanoscale structures is pursued. This can supply an object with new properties without modifying its bulk material.

Typical functionalities provided by nanocoatings are, for example, wear resistance (Gemici et al. 2008), corrosion resistance (Hamdy 2006), antibacterial activity (Seddiki et al. 2014), catalytic activity (X. Zhang et al. 2014) and controllable wetting (Sun et al. 2005). Depending on the working mechanisms, some coatings can even be built into multilayered structures that create multiple functions (H.-G. Shi et al. 2021; Zeng et al. 2021). For this dissertation, liquid-repelling coatings will be focused on.

Liquid-repelling surfaces prevent liquid droplets from sticking and spreading onto them. Different terminologies are used based on the types of liquids that are repelled: hydrophobic surfaces repel water, oleophobic surfaces repel oils. Omniphobic (sometimes referred to as amphiphobic) surfaces repel all liquids. However, the term omniphobic is usually used with a less strict definition, since surfaces that would repel every single liquid are extremely difficult to manufacture. Only one coating that can be regarded truly superomniphobic has been reported in the literature so far (T. Liu and Kim 2014).

Surfaces are often categorized under different terms based on their degree of wetting. These categories are presented in Figure 2.2. If the contact angle (CA), meaning the angle between the liquid-air interface and the surface, is greater than  $90^\circ$ , the surface is considered phobic, and otherwise philic. Extreme cases of these are usually defined as superphobic ( $CA > 150^\circ$ ) and superphilic ( $CA < 10^\circ$ ), the former often including an additional requirement for the sliding angle (SA) to be less than  $5^\circ$  (Parvate et al. 2020). SA refers to the maximum angle the surface can be inclined to before the liquid droplet placed onto it rolls off.

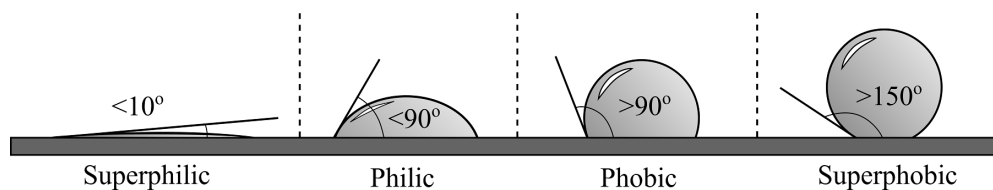


**Figure 2.2** Terminology for different degrees of wetting.

Superhydrophobic surfaces have gained the largest interest regarding wettability. The complete repellency of water droplets can, for example, provide self-cleaning, anti-corrosion and anti-icing properties. However, superphilic coatings have their own uses as well, such as windshields that form an ultrathin layer of water on their

surfaces, thereby not impairing visibility.

Wetting is governed by the surface structure of the solid surface and the interfacial tensions of different interfaces: solid-liquid ( $\gamma_{SL}$ ), liquid-vapor ( $\gamma_{LV}$ ) and solid-vapor ( $\gamma_{SV}$ ). Typically, three equations are used to describe the wetting behaviour:

- **Young's equation** defines the so-called intrinsic CA ( $\theta_Y$ ) that neglects the surface structure, so it only applies to an ideally smooth surface (Bhushan and Jung 2011):

$$\cos \theta_Y = \frac{\gamma_{SV} - \gamma_{SL}}{\gamma_{LV}} \quad (2.1)$$

- **Wenzel equation** defines the apparent CA ( $\theta_W$ ) in a homogeneous wetting state (the whole solid surface underneath the droplet is in liquid contact) by implementing the effect of surface structure (Wenzel 1936):

$$\cos \theta_W = \frac{A_{SL}}{A_{p_r}} \cos \theta_Y, \quad (2.2)$$

where  $A_{SL}$  is the actual contact area between the droplet and the surface, and  $A_{p_r}$  is the area the droplet projects onto the surface.

- **Cassie-Baxter equation** defines a heterogeneous wetting state, where the pores in the surface structure are not wetted, so that the droplet partly rests on the solid surface and partly on air pockets (Cassie and Baxter 1944):

$$\cos \theta_{CB} = \frac{A_{SL}}{A_{p_r}} f_{SL} \cos \theta_Y - 1 + f_{SL}, \quad (2.3)$$

where  $f_{SL}$  is the fraction of the SL interface from the whole interface underneath the droplet.

These equations are still used, but recent studies have raised up the problems arising from unideality or structural complexity of surfaces (Parvate et al. 2020). For example, if the surface is chemically heterogeneous, no single values can be found for the interfacial tensions that would apply. Also, the applicability of the equations have been linked to the size of the liquid droplet in relation to the size scale of the surface structure (Marmur and Bittoun 2009).

For superphobic surfaces, the Cassie-Baxter wetting state is usually formed. Superphobicity is easiest to reach by minimizing both the liquid-solid contact area and the surface energy. For minimizing the contact area, a hierarchical surface structure is often used, which means forming a nanostructure on top of a microstructure (Ellinas et al. 2011; H. Li and Yu 2016). The surface energy issue is usually tackled by coating the surface with a low surface energy material, because not many intrinsically strongly hydrophobic materials that could be used to build the whole structure are known. In theory, perfect omniphobicity can be reached without paying attention to the surface chemistry, but this would require a perfect doubly reentrant structure that is difficult to manufacture, especially cost-effectively and in large scale (T. Liu and Kim 2014).

The last thing to consider is the substrate. Surfaces of some less resilient materials and softer metals than steel can be quite easily surface-shaped by etching, for example (T. Shi et al. 2016). This facilitates forming the desired surface structure. However, the low plasticity and resiliency of hard metals makes it difficult to imprint or etch a fine surface structure on them (Jiang et al. 2016). In cases like these, a coating can be applied for this purpose. The challenge of producing well-adherent durable coatings is still somewhat unsolved though.



# 3 Flame spray synthesis and additional coating methods

Because this dissertation is built around flame synthesis, it is essential to explore the whole process in more detail. There are many lower-level classifications that divide variations of flame synthesis methods into different categories (Teoh et al. 2010). One crude division can be made based on the precursor type: vapor-fed versus liquid-fed reactors (S. Li, Ren et al. 2016). The discussion here will be limited to liquid-fed reactors, since LFS belongs in this class. There are additional categories that have been defined at least based on atomization mechanisms and precursor combustion enthalpy (Teoh et al. 2010), but they will not delved into.

The structures of synthesis setups used around the world usually differ from each other in various ways. Therefore, adjusting certain parameters will not have an identical impact in every case. Nevertheless, the basic principles governing the process should be relevant to all of them. Different parts of the synthesis process that mostly apply for all typical setups will be dicussed.

Two other coating methods, atomic layer deposition (ALD) and silanization, that were used in **Publication IV** will also be described at the end of this chapter. These methods can be used by themselves or combined with others, like we did here with LFS. Let us begin by exploring the LFS process.

## 3.1 Liquid flame spray process

Liquid flame spray, or LFS, that was used in this dissertation, falls into the liquid-fed reactor group, and can be categorized as a specific FSP method (Tikkanen et al. 1997). We should start by describing the structure of the two burners used. Figure 3.1 shows the principal structures, even though not in completely realistic dimensions.

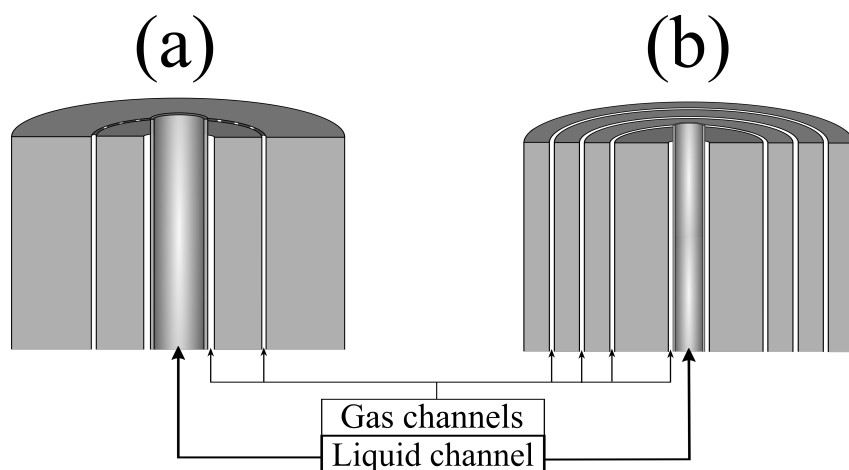


**Figure 3.1** The structure of the LFS burners used in the dissertation: (a) the LR burner and (b) the KP burner.

The same names will be used for the burners as Aromaa et al. 2007. The burner in Figure 3.1a will be referred to as the LR burner and the one in Figure 3.1b as the KP burner. The LR burner has a wider liquid channel for facilitating larger possible production rates compared to the KP burner. The KP burner, on the other hand, provides two additional gas channels, which offers more possibilities for modifying the process. There is also a structural difference in the outer gas channel of the LR burner compared to other gas channels. The gas emerges from multiple holes divided evenly on an annular ring, whereas for the KP burner, all the channel outlets are annular.

The main gases used in LFS are hydrogen ( $H_2$ ) and oxygen ( $O_2$ ), and they can be switched between the channels. An extra nitrogen flow has also been added in between the main flows in some studies to push the base of the flame further from the burner. This should promote the cleanliness of the burner head during synthesis. (Aromaa et al. 2007; Juuti et al. 2019)

In short, the synthesis process encompasses feeding a liquid precursor solution into a flame formed by the  $O_2$  and  $H_2$  flows, where the inner gas flow atomizes the liquid jet. The droplets burn in the flame and either form the end product from gaseous materials through nucleation (gas-to-particle route) or in liquid droplets in case of incomplete evaporation (droplet-to-particle route). However, the whole picture is much more complicated than that and will be discussed in more detail. The

individual spherical particles that nucleate in the flame are referred to as primary particles (PPs), and the final material is formed through their aggregation and agglomeration.

In this dissertation, the forming nanoparticles were either guided directly to a substrate from the flame (**Publication IV**) or collected with a custom-built electrostatic precipitator (ESP) (**Publications I, II and III**). The ESP consisted of two parallel metal plates, one of which had thin metal wires attached to it and was connected to a high voltage source (25–40 kV), while the other plate was grounded. The high voltage creates corona discharges in the wire tips, charging particles around them. The particle flow was directed through the plates and the material ended up onto the grounded plate due to the electric field formed between the plates. The nanomaterial was then scraped off the collection plate.

The main parameters that can be adjusted in the LFS process are the composition of the precursor solution, the liquid feed rate, and the gas flows. From the producer's standpoint, it is relevant to assess how different parameter choices affect the profitability versus the end product properties. Figure 3.2 shows schematically how different parameters could affect the interests of the producer. The lower portion of the graph will be elaborated in the next section.

Production efficiency, material costs, and the environmental impact and possible by-product handling were chosen as the three main factors guiding the choices of the producer. Obviously, there are always also other factors, like existing facilities, at

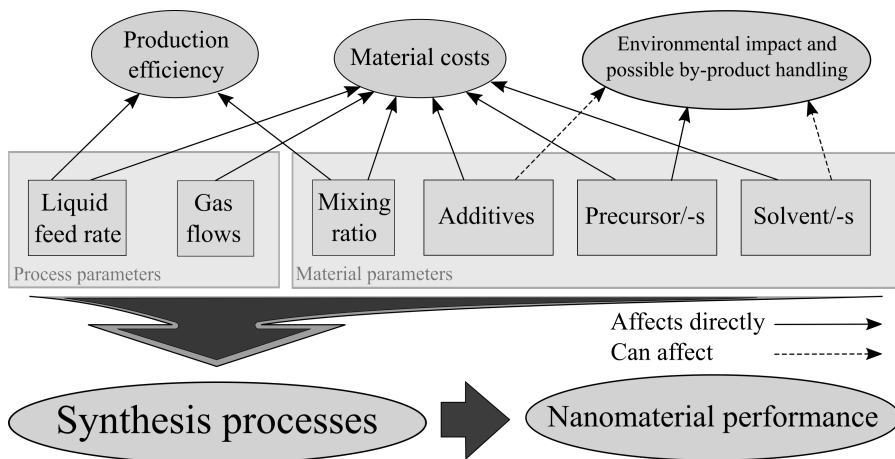


**Figure 3.2** A scheme of the parameter choices affecting the resources and the output of a nanomaterial producer.

play, but they are irrelevant to this examination. The adjustable parameters were divided into material and process parameters. The first group comprises the choice of precursors, solvents and possible additives, and the mixing ratio of the chosen ingredients. The second group represents the parameters that can be adjusted during the process, although the gas flows cannot be swapped, when the synthesis is running.

Let us start from the left in Figure 3.2. The liquid feed rate clearly affects production efficiency by directly raising or lowering the production rate, and it also has an impact on the material costs, as less gas is consumed per gram of obtained nanomaterial at higher feed rates. The gas flows only impact the material costs through gas consumption, if we assume fixed choices of gases. If a carbon-containing combustion gas was chosen, an environmental effect could also be argued for in large-scale production.

Of the material parameters, all the material choices obviously contribute to the material costs, but so does the mixing ratio, as high concentrations reduce the consumption of other components per gram of nanomaterial. The mixing ratio defines the production efficiency together with the liquid feed rate, but one has to keep in mind that adjusting these parameters has an impact on the process. Therefore, the production efficiency of a certain type of nanomaterial cannot be simply raised by increasing them. The environmental impact is mostly defined by the by-products that are produced. If precursors that generate toxic by-products are used, some after-treatment could be required. All in all, LFS can be considered quite eco-friendly as the burning gases themselves only produce water vapor, and no problematic liquid waste is left behind if the whole precursor solution burns or evaporates. This is a huge advantage of flame synthesis compared to, e.g., wet chemical methods.

## **3.2 Particle formation process**

In this section, the effect of different parameters on the process will be examined according to the existing literature. However, it is impossible to give any descriptions of how a certain change modifies the behavior of the process in every experimental setup. In addition to basically every setup being somehow different from each other, the parameters work together, meaning the effect of an adjusted parameter can depend on the value of another parameter, which adds to the complexity.

Figure 3.3 aims to provide a big picture of the whole flame synthesis process.

Here, the material parameters were divided a little differently than before, as it is convenient to link certain properties of the precursor solution to certain intermediate processes in the flame. All considered properties are sums of the material choices and their mixing ratios, so adjusting them completely separately is impossible.

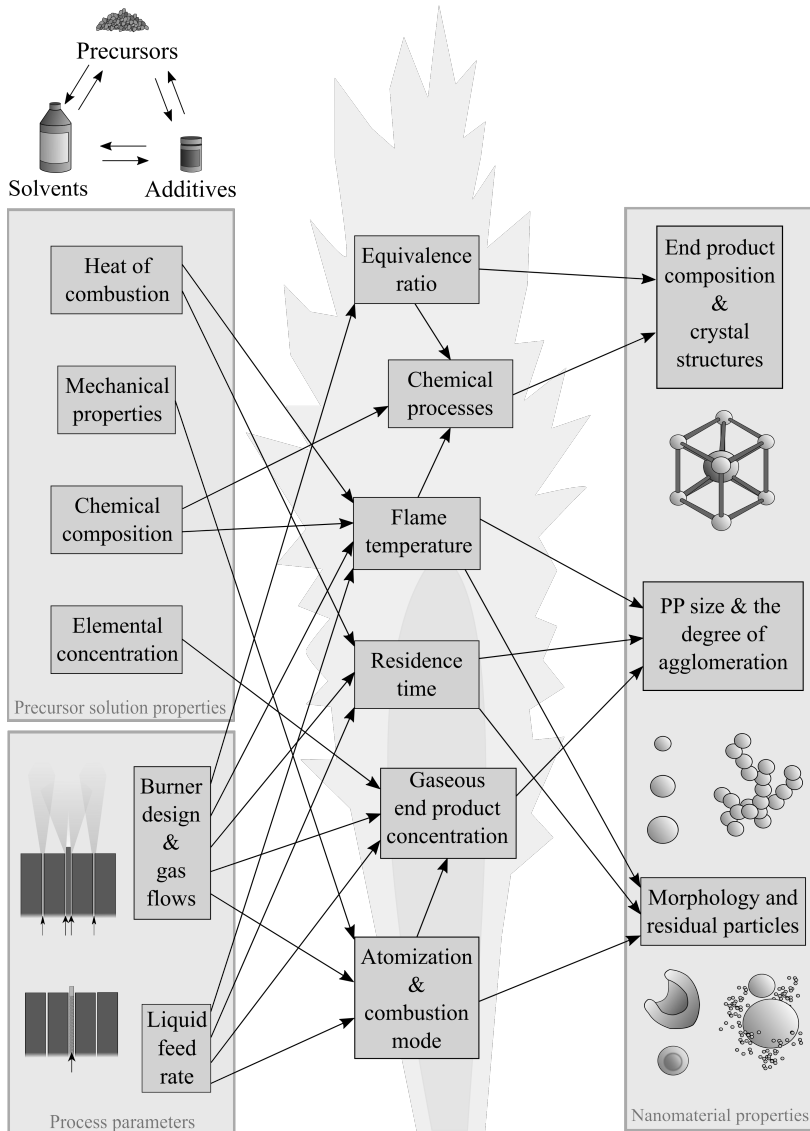


**Figure 3.3** A scheme of the effect of different parameters to intermediate processes and eventually the end product in flame spray pyrolysis.

Let us start by defining what is meant by each box on the left side in Figure 3.3:

- **Heat of combustion (HOC):** The total energy per volume that can be released from the precursor solution during pyrolysis (often expressed in kJ/ml)
- **Mechanical properties:** Viscosity and surface tension as the main factors, but density can also have a slight effect
- **Chemical composition:** The concentrations of all compounds present in the solution
- **Elemental concentration:** The concentration of the base element or elements in the precursor solution
- **Burner design & gas flows:** The choices and volumetric flow rates of process gases, and the resulting flow fields with the chosen burner design
- **Liquid feed rate:** The volume per time unit of the precursor solution injected into the flame (often expressed in ml/min)

The nanomaterial properties on the right side of the graph, determining the final product performance, were divided in three pairs. Firstly, the chemical composition and the crystal structure are tightly bound together, so they are handled as a single package. Secondly, primary particle size and the degree of agglomeration can be controlled separately, but they are often determined by same factors, so they were clumped together. Lastly, morphology and possible residual particles often go hand in hand. Specific crystal shapes of some compounds are not accounted for here.

As "intermediate processes", six factors were chosen that can be somehow distinguished from each other, two of which ("Chemical processes" and "Gaseous end product concentration") were also considered to depend on some of the others. These factors will be discussed separately in a hopefully logical order along with possible ways to influence them, and how they may affect the final particle properties.

### 3.2.1 Atomization & combustion mode

Atomization can be regarded as the first step in the synthesis process. Because the size of the droplets is important for their evaporation rate, efficient atomization helps in producing homogeneous material. The main factors determining the droplet size

distribution are: the mechanical properties of the precursor solution (mainly viscosity and surface tension), the liquid feed rate, the choice of the atomizing gas and its flow rate, and the burner design. The burner design combined with the atomizing gas flow determines the pressure drop across the nozzle, which several studies have used as the measure that ensures proper atomization (Heine and Pratsinis 2005; Mädler, Kammler et al. 2002; Meierhofer et al. 2017).

Droplet burning is a surface process, so the best droplet size measure is the Sauter mean diameter (SMD) that has been defined for external-mixing nozzles by Lefebvre and McDonell 2017 as:

$$\text{SMD} = 51d_0 \text{Re}^{-0.39} \text{We}^{-0.18} \left( \frac{\dot{m}_l}{\dot{m}_g} \right)^{0.29}, \quad (3.1)$$

where  $Re = \frac{\rho_L U_R d_0}{\mu_L}$  is the Reynolds number,  $We = \frac{\rho_L d_0 U_R^2}{\sigma}$  is the Weber number,  $d_0$  is the diameter of the liquid channel,  $\dot{m}_l$  and  $\dot{m}_g$  are the mass flow rates for the liquid and the atomizing gas,  $\rho_L$  is the liquid density,  $U_R$  is the relative velocity of the gas and the liquid at the nozzle end ( $\approx$  the gas velocity at high gas flow rates), and  $\mu_L$  and  $\sigma$  are the viscosity and the surface tension of the liquid. The actual value of  $U_R$  might be challenging to determine due to differences in burner geometries and possibly strong turbulence. The droplet sizes typically vary between ca. 5–60  $\mu\text{m}$  (Heine and Pratsinis 2005; Keskinen et al. 2008; Stodt et al. 2019; Tikkanen et al. 1997), strongly depending on the parameters.

Combustion mode is a measure that is sometimes used to describe how the burning of the droplet cloud occurs as a whole (Mädler, Kammler et al. 2002; Stodt et al. 2019). It can not really be measured directly, but a dimensionless group combustion number  $G$  can be calculated to predict it. Since the exact conditions are still difficult to quantify, approximations must always be made. (Stodt et al. 2019) There are not very many studies that inspect the combustion mode in an FSP setting, but probably the most used form for  $G$  is defined as: (Chen and Gomez 1997)

$$G = 2\pi\rho(n)d_d R_c^2, \quad (3.2)$$

where  $\rho(n)$  is the droplet number density,  $d_d$  is the average droplet diameter and  $R_c$  is the droplet cloud radius. Generally, three distinct modes have been defined based on the value of  $G$ : (Mädler, Kammler et al. 2002; Stodt et al. 2019)

- $1 \leq G \leq 100$ : External group combustion, where a core of non-evaporating droplets are surrounded by vaporizing droplets
- $0.01 \leq G \leq 1$ : Internal group combustion with individually burning and vaporizing droplets
- $G < 0.01$ : Isolated single droplet combustion, where the individually burning droplets do not interfere with each other

According to Stodt et al. 2019, the combustion mode changes along the flame zone, depending on the chosen parameters. The optimal situation for producing homogeneous nanomaterial would be maximizing the time in single droplet and internal group combustion modes, as they are the most efficient for complete evaporation. However,  $G$  does not take into account some relevant factors for burning, like flame temperature, so it can not be used on its own to predict the quality of the end product. Even though  $G$  will not be used as an observed measure in this thesis, it was mentioned here due to its relation to the atomization and the relevance to the combustion process.

### 3.2.2 Flame temperature

Because flame synthesis is fundamentally a heat-driven process, the flame temperature is a very essential factor. In LFS, the gas flows usually provide the largest contribution to the heat overall due to the often high hydrogen flow compared to the liquid feed rate. Therefore, raising the hydrogen flow is the simplest way to increase the flame temperature. This will likely, however, have other effects and impact the end product properties. Increasing the hydrogen flow renders the flame more reducing, which can effect the redox chemistry of the precursor.

The precursor solution and its feed rate also play a role in determining the temperature field, especially by providing higher local temperatures for burning solution droplets with high energy contents. The main property of the precursor solution affecting the flame temperature is its HOC. In addition to HOC, the chemical composition can have a significant effect on the temperature field. Chiarello, Rossetti, Forni et al. 2007 measured clearly varying temperatures when using two solutions with identical HOC values. One of the solutions contained octanoic acid that has a linear carbon chain, while the other contained 2-ethylhexanoic acid (EHA) with a



branched chain instead.

The flame temperature is especially important when using poorly volatile precursors, or producing materials with relatively low melting and boiling temperatures. If a once formed solid material can evaporate again in the flame zone, homogeneous nanomaterial is easier to produce through nucleation (Rosebrock, Wriedt et al. 2016). Raising the flame temperature can also activate certain chemical reactions that facilitate the synthesis. However, if the precursor is very volatile, it vaporizes completely already in lower temperature. In these instances, raising the flame temperature mostly impacts the size of PPs and the shape of the final particles. Higher temperatures enhance coagulation and increase the interaction between formed PPs, resulting in a higher degree of agglomeration and aggregation. In the LFS process, maximum temperatures of up to 2600°C have been measured (Pitkänen et al. 2005; Tikkanen et al. 1997).

### 3.2.3 Equivalence ratio

When anything is burning, the amount of oxygen plays an important role in determining how fast and intensely this occurs. It can also affect the chemical composition of the material, since certain structures are preferred when an excess or a deficit of oxygen is present. For example, in flame synthesis of titanium oxide, oxygen availability has been observed to be one of the key factors in determining the crystallographic phase composition of the end product (C. Liu et al. 2018; Manuputty et al. 2019).

Equivalence ratio is sometimes used to quantify how much oxygen is present during the synthesis process (Aromaa et al. 2007; Mädler, Kammler et al. 2002; Strobel and Pratsinis 2009). It describes the actual amount of oxygen in relation to the amount that would be required to burn all volatile material present, and is defined as:

$$\Phi = \frac{\left(\frac{n_{fuel}}{n_{oxygen}}\right)_{act.}}{\left(\frac{n_{fuel}}{n_{oxygen}}\right)_{stoich.}}, \quad (3.3)$$

where  $n_{fuel}$  and  $n_{oxygen}$  are the amounts of substance for combustible material and oxygen molecules, respectively. The subscripts *act.* and *stoich.* refer to the actual ratio and the ratio in stoichiometric conditions. Therefore, values below 1 signal oxidic

conditions and values greater than 1 anoxic conditions.

Usually in LFS, the gas flows is the main factor determining  $\Phi$ , but if a high liquid feed rate is picked, that can also make a significant contribution (not marked in Figure 3.3 with an arrow). The real accurate  $\Phi$  value is, however, difficult to define in an open flame setup, since the entrainment air coming from the surroundings changes it. In addition, temperature often goes hand in hand with  $\Phi$  in LFS synthesis, since raising oxygen flow lowers the flame temperature in conjunction with  $\Phi$  due to the extra gas that has to be heated up (Mädler, Kammler et al. 2002). However, equivalence ratio can still be a useful measure in monitoring the flame conditions.

### 3.2.4 Residence time

In addition to the temperature field, the time the droplets spend in the hot zone affects whether they burn completely or not. After nucleation, the particles can also still spend time in the high temperature zone, which determines how much the PPs grow and agglomerate. Residence time can be considered the total time spent in the flame zone, and is mostly determined by two variables: gas velocity (mainly the atomizing gas) and the flame length. It is quite tightly linked to equivalence ratio, since a linear dependence between  $\Phi$  and the length of the flame has been observed (Mädler, Stark et al. 2002). However, this relationship does not always apply to complex flow setups, as was discovered in **Publication II**.

In theory, the gas velocity can be adjusted through the atomization flow without changing the flame length, if the rest of the experimental setup is modified accordingly. One has to keep in mind, however, that changing the atomization gas flow affects the droplet distribution, which in turn has an impact on the combustion behavior. Also, turbulence becomes a significant factor with high velocities.

### 3.2.5 Gaseous end product concentration

If we presume that all of the particles homogeneously nucleate from the gas phase, the concentration of the gaseous end product provides the third staple for defining the PP size and the degree of agglomeration, beside flame temperature and residence time. The amount of available material (concentration), the interaction intensity (temperature) and the interaction time (residence time) will mostly determine the

size and the shape of the final material. The end product concentration depends on the elemental concentration in the precursor solution, the liquid feed rate and the gas flow mechanics. Also, incomplete precursor evaporation leads to a lower end product concentration, because residual particles can consume a comparatively large fraction of the material volume. Therefore, the concentration can only be directly raised by increasing liquid feed rate, if it does not impair the evaporation process.

### 3.2.6 Chemical processes

"Chemical processes" is definitely the least understood box in Figure 3.3 due to the complexity of all the variables involved. This tends to be the part in the FSP simulations that is usually grossly oversimplified. The models normally assume a very simple route of precursor combustion leading to gaseous end product which then nucleates into solid particles, and this is basically a necessity, because as Schulz et al. 2019 stated: "Only little is known about the initial steps between precursor decomposition and formation of first, stable nuclei and their precise chemical composition is mostly unknown." What makes untangling all the details tricky, is the high temperatures, extremely short time scales and the difficulty to experimentally study the process without interfering with it. Also, the complete synthesis process is too complex to be simulated at a molecular level, which would be required for reliable and detailed results.

If reliable sampling cannot be performed during the process, changes in the end product must be used to deduce the effects of parameter adjustments. Certain properties of the precursor solution have been linked to the combustion processes. Jossen, Stark et al. 2003 and Jossen, Pratsinis et al. 2005 studied how the ratio between the solvent boiling point ( $T_{bp}$ ) and the precursor melting/decomposition temperature ( $T_{d/mp}$ ) affect the particle homogeneity and morphology as a function of combustion enthalpy. They observed that if  $\frac{T_{bp}}{T_{d/mp}}$  was adequately high or the flame contained enough energy, solid and homogeneous particles could be produced. However, based on other literature, this result can not be deemed always applicable, but only being a part of the puzzle. A link between the specific volumes of the end product and the precursor regarding the particle morphology has also been suggested (Mädler and Pratsinis 2002).

Changing and mixing solvents has been studied for influencing resulting nanoma-

terial. Poorly soluble precursors, such as nitrates and acetates, have been observed to produce residual particles, when using pure alcohols as solvents (Chiarello, Rossetti and Forni 2005; Chiarello, Rossetti, Forni et al. 2007; Mädler and Pratsinis 2002). However, when the alcohols were substituted with carboxylic acids or mixed solvents, the residual particles could be erased. This was attributed to the formation of possibly more volatile intermediate species, indicating that the in-flame chemical processes can be influenced by changing the precursor solution composition.

Meierhofer et al. 2017 studied different precursor-solvent combinations for producing  $\text{Li}_4\text{Ti}_5\text{O}_{12}$  particles. They also discovered that the connection between the precursor solution chemistry and the synthesis process is very complex. Carboxylic acids were observed to transform a low-volatile lithium nitrate into a more volatile organometallic lithium complex, but also the HOC played a role in obtaining homogeneous material. Another factor they pointed out was the requirement of stable solutions in the long term, if unwanted chemical reactions are to be prevented. These kinds of properties are difficult to find out without case-by-case experimentation.

Single droplet experiments offer another possible explanation for this homogenizing effect of solvent mixing. Rosebrock, Riefler et al. 2013 observed that a convenient tuning of the precursor solution composition led to droplet explosions during burning. The larger droplets exploded into very fine droplets that would efficiently evaporate, resulting in homogeneous nanomaterial. Two suggested pathways leading to the explosions were a pressure buildup inside the droplet due to formation of a viscous shell, and the nucleation of vapor bubbles due to concentration gradients caused by uneven evaporation of different chemical species inside the droplets. Although some ideas have been developed on how the chemical composition affects the burning process, it is still quite unclear how the manipulation of the precursor solution can be used to adjust the composition and the structure of the end product in general.

### **3.3 Atomic layer deposition**

Atomic layer deposition (ALD) is used to produce thin coatings and can be categorized under chemical vapor deposition (CVD) methods (Miikkulainen et al. 2013). In working principle, ALD differs from traditional CVD processes in the way the gaseous reactants are handled. They are introduced to the substrate surface as iso-

lated pulses in a cyclic manner, as shown in Figure 3.4. The surface is first saturated with one reactant, followed by purging the nonadhering molecules and possible by-products. The second reactant is then added, resulting in chemical reactions on the surface, and again followed by purging. This provides a precisely controlled process, inhibiting most unwanted reactions in the gas phase.

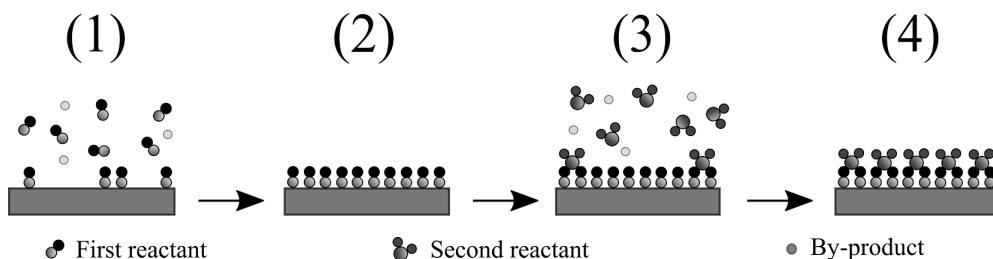


**Figure 3.4** A scheme of the four-step ALD process: (1) The adsorption of the first reactant on the substrate, (2) Purging of nonadhering reactant molecules and possible by-products, (3) Introduction of the second reactant on the surface, (4) Purging of unreacted molecules and possible by-products.

One coating cycle typically lasts around 0.5 seconds and produces a layer thickness of 0.1 to 3 Å (Leskelä and Ritala 2003; Puurunen 2005). The precise thickness is determined by the precursor molecules and the process parameters. In some cases, even average layer thicknesses of 0.04 Å have been measured (Lim et al. 2003). These sort of extremely low values usually correspond to an incomplete monolayer, which means the whole surface is not completely covered by the molecules in a single cycle. The final layer thickness can then be very accurately controlled by the number of coating cycles.

The ALD process usually requires some pretreatment, because the purity of the substrate before coating is crucial for high-quality layers. In **Publication IV**, the substrates were first treated in a nitrogen-oxygen atmosphere, which ensured the complete oxidation of any organic contaminants. Both the pretreatment and the coating were performed in a Picosun P-1000 ALD system at 300°C. Some promising results have been found in the literature in using ALD for nanoparticle layer reinforcement, which is relevant to **Publication IV** (Dafinone et al. 2011; D. Zhang, Xu et al. 2015; D. Zhang, L. Zhang et al. 2015).

## 3.4 Silanization

Silanization refers to coating a surface with silane molecules. The amount of impurities on the surface has a significant effect on the adherence of the molecules, so a pretreatment is usually also used prior to silanization (Vuori, Leppiniemi et al. 2014). When the process is conducted carefully, the silane molecules bond strongly to the surface, forming an organized array.

Silanization can be used for many different purposes. For example, fluorosilanes are often utilized for lowering the surface energy, as was the case in **Publication IV**. A so-called liquid phase deposition process was used, which basically means adsorbing the silane molecules onto the surface from a liquid solution. A detailed description of the process used can be found in the literature (Vuori, Hannula et al. 2014; Vuori, Leppiniemi et al. 2014).

# 4 Characterization methods

In this chapter, all the characterization methods used in this dissertation will be described. The first section contains methods that more or less encompass all of the publications, whereas the the second section is only relevant to **Publication III**, and the third section to **Publication IV**.

## 4.1 Structural and surface characterization

If one wants to thoroughly study the material they have produced, several offline characterization methods are required. Let us imagine a situation similar to the one created in **Publication IV**. Nanomaterial is synthesized with LFS, deposited onto a surface, and coated with another substance. This scenario is depicted in Figure 4.1 with appropriate characterization methods prior to and after deposition onto the substrate.

After the nanomaterial is generated with LFS, many of its properties are easiest to analyze from a powder. The most precise way of inspecting the size and the shape of ultrafine nanoparticles is transmission electron microscopy (TEM). The method is based on imaging with electrons transmitting through the sample, which usually limits the maximum thickness of the imaged object to around 100 nm. Even resolutions revealing the atomic planes of a crystal can be reached with advanced equipment. TEM systems can also be equipped with additional detectors, like an energy-dispersive x-ray spectroscopy (EDS) detector that enables elemental analysis, and electron energy loss spectroscopy (EELS) detector that offers more specific and detailed analysis of the elemental composition and chemical bonding.

Because TEM imaging can only inspect a tiny portion of the whole powder, it is not a reliable way to investigate whether a small number of large particles are included in the sample or how prevalent they are. Especially with flame synthesis,

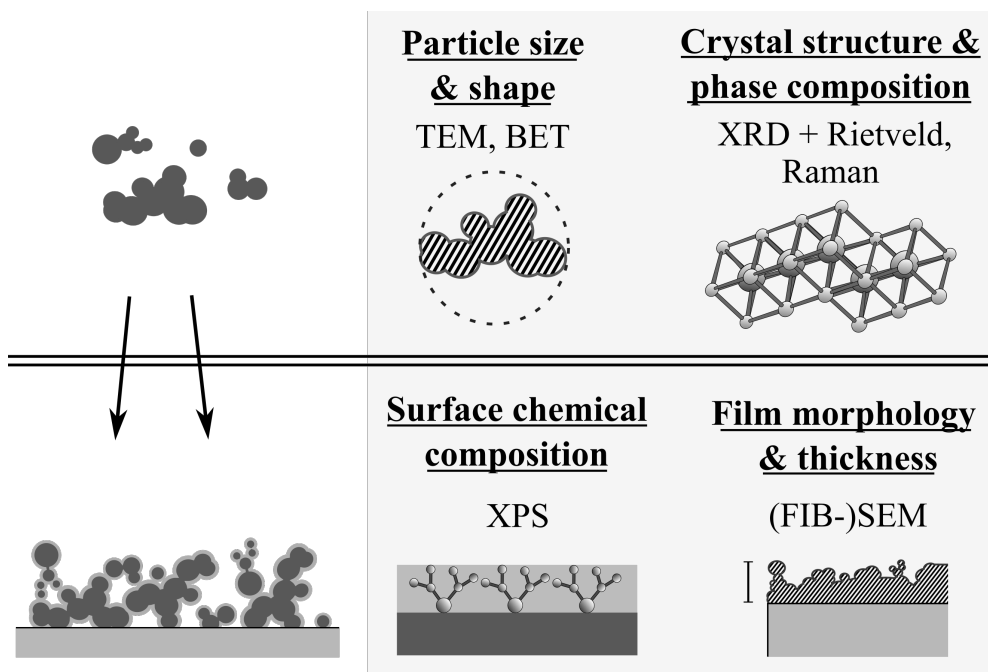


**Figure 4.1** A scheme of different characterization methods used for studying properties of a nanocoating.

larger residual particles are often encountered, so Brunauer-Emmett-Teller (BET) analysis is a valuable tool for their detection. It can measure the specific surface area (SSA) (the total surface area of a powder sample per unit mass) by using gas molecule adsorption. BET theory can be used to determine the amount of gas molecules adsorbed on the sample, which allows calculation of the surface area a monolayer would cover. Even a low number of significantly larger solid particles will drastically lower the SSA of a nanopowder sample. Another factor having a large impact on the SSA value besides the size distribution is particle morphology. For example, hollow particles yield considerably higher SSA values compared to solid particles due to their low effective density, which has to be kept in mind when interpreting the results.

Also the crystal structure of the nanomaterial is easier to study from a powder than a coating, especially in case of ultrathin coatings. The most common method for structural analysis is x-ray diffraction (XRD) that can distinguish different crystal structures from each other. When analyzing a powder, basically every crystal orientation is present simultaneously, so strong interference maxima form at certain



diffraction angles, revealing the crystal structure. XRD can be combined with Rietveld analysis to gain more detailed information. If all the existing elements and the possible crystallographic phases have been identified, it can be used to calculate the phase composition of the sample from the XRD pattern. Among some other factors, instrumental parameters, cell dimensions, particle size and possible microstrain determine the intensities and the shapes of the diffraction peaks. Rietveld analysis works by refining these parameters, so that the computational diffraction pattern matches the measured pattern as well as possible. There are numerous programs that can be used to perform Rietveld analysis. We chose BRASS 2 program (Birkenstock et al. 2003) for this dissertation.

Even though XRD can tell apart different crystal structures, it cannot reliably distinguish isomorphous compounds. For example, two of the iron oxide phases, maghemite and magnetite, have very similar cubic structures, so they can produce almost identical XRD patterns. In a situation like this, an additional method is required to detect the specific phase. Raman spectroscopy is one alternative for this. It uses inelastic Raman scattering of monochromatic laser light to detect vibrational and rotational (only vibrational for solid samples) modes in the sample. Since these modes are specific to a certain chemical environment, each compound has its own "fingerprint" that can be measured and used to identify the phase. However, when studying compounds sensitive to heat, the laser power has to be very carefully selected to avoid measurement errors due to structural changes in the sample.

There are many different mechanisms at play, when particles deposit onto a substrate. To see how the particles are organized on the surface, a scanning electron microscope (SEM) can be used. SEM imaging is based on rastering the sample surface with a focused electron beam and detecting the low-energy secondary electrons emerging from the top layer. This produces a topographical image of the surface. When a focused ion beam (FIB) is added to the device setup, ions ( $\text{Ga}^+$  ions in **Publication IV**) can be used to mill a hole that reveals the cross-section of the coating, which can then be imaged. This is of great interest when studying thin films, since the film thickness is usually regarded as an important parameter. SEM systems also often include an EDS detector that can be used for elemental mapping across the surface or the cross-section.

Since the performance of functional coatings is tightly linked to their surface properties, it is often essential to have knowledge on the chemistry of the topmost

layer. X-ray photoelectron spectroscopy (XPS) is an excellent method for this purpose. The XPS system uses x-rays to release electrons from the surface atoms and ions. Since electrons of each element have specific binding energies, the chemical composition can be calculated from the measured kinetic energies of ejected photoelectrons. When the x-ray energy is chosen carefully, all of the measurable electrons come from the outermost 1–10 nm, which makes the method very surface sensitive.

## 4.2 MR fluid characterization

For characterizing MR fluids, magnetization of the nanoparticles, rheological properties with (on-state) and without (off-state) an external magnetic field, and the sedimentation behavior are the most relevant factors. In **Publication III**, the on- and off-state rheology measurements were performed with two different geometries that are presented in Figure 4.2.

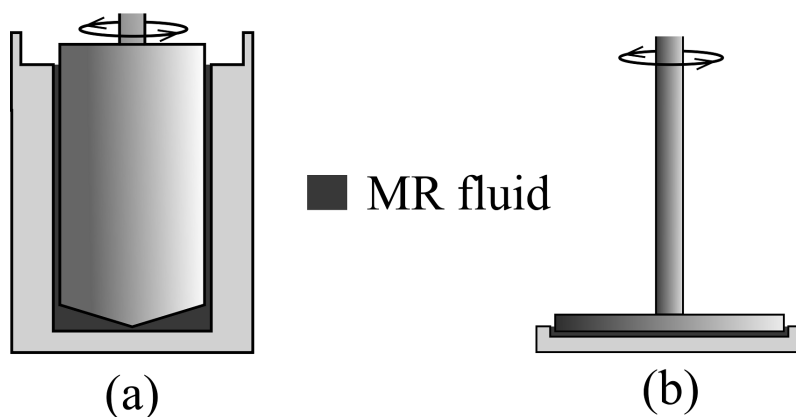


**Figure 4.2** Measurement geometries for (a) off-state and (b) on-state rheology measurements. (Adapted from **Publication III**)

The distinct geometries were used, because the concentric cylinder geometry (Figure 4.2a) provided better sensitivity for low-viscosity liquids, therefore being more suitable for the off-state measurements. For the on-state measurements, the geometry had to be changed to produce a uniform magnetic field. Shear rate was logarithmically increased from 0.01 to  $1000 \frac{1}{s}$ , and dynamic yield stress was determined

from the measured data by fitting to the Bingham model, which can be written as:

$$\tau_R = \tau_y + \eta_p \dot{\gamma}_R, \quad (4.1)$$

where  $\tau_y$  is the yield stress,  $\eta_R$  is the plastic viscosity and  $\dot{\gamma}_R$  is the shear rate. In addition, oscillatory measurements were performed to assess what happens in the microstructure of the MR fluid, when the strain amplitude is changed. For this, storage modulus  $G'$  and loss modulus  $G''$  were calculated. These two measures are defined as:

$$\begin{cases} G' = \frac{\tau_o}{\gamma_o} \cos \delta \\ G'' = \frac{\tau_o}{\gamma_o} \sin \delta, \end{cases} \quad (4.2)$$

where  $\gamma_o$  is the strain amplitude,  $\tau_o$  is the stress response, and  $\delta$  is the phase shift between them.

The magnetization measurements were performed with a magnetometer in varying temperatures and magnetic field strengths. The magnetometer can be used to draw hysteresis curves for the powder samples and to obtain their coercivities and saturation magnetizations. The sedimentation behavior was assessed by photographing the MR fluid in a test tube every 60 minutes. The sedimentation rate was then calculated from the images by tracking the interface of the particles and the carrier fluid.

### 4.3 Surface properties analysis

Since the goal in **Publication IV** was to achieve a very liquid-repelling coating, wettability analysis was used to measure the performance. CA and SA can be determined with various equipment. In our CA measurements, small droplets of different test liquids were placed on the sample surfaces and filmed. A computer program then calculated the CA from the video using a suitable droplet shape fit. SA measurements were conducted by placing test liquid droplets on an inclined plane and observing whether they rolled off it or not. The equipment allowed a very careful adjustment of the inclination angle.

The adhesion of the coating to the substrate was evaluated by a microscratch test that is often used to measure adhesion and cohesion of coatings and thin films

(Kilpi et al. 2016). A Rockwell diamond stylus was dragged along the surface with an increasing load. Three parallel scratches were made and imaged. Penetration depth, friction force and acoustic emission were measured simultaneously during the scratching.

# 5 Results and discussion

The results will be presented in three parts, since **Publications I+II, III, and IV** represent three a bit thematically separate areas. The first part (**Publications I+II**) mainly focuses on controlling the crystallographic phase composition of iron oxide particles when using iron nitrate as the precursor. It will also cover other particle properties associated with phase formation. The last two parts exhibit the application studies: bidisperse MR fluids (**Publication III**) and a multilayered omniphobic nanocoating (**Publication IV**). These two sections encompass the nanomaterial synthesis and the application-relevant results.

## 5.1 Controlling the particle formation process in LFS synthesis

This section entails the results from **Publications I and II** that mostly focus on factors determining the phase composition of iron oxide particles in LFS synthesis from iron nitrate as the precursor. In **Publication II**, we will also examine other properties that are affected simultaneously. In these two papers, the two different burner designs introduced in Chapter 3 were utilized: the LR burner (Figure 3.1a) in **Publication I** and the KP burner (Figure 3.1b) in **Publication II**. Both studies also have two distinct aspects for studying the phase formation process: (1) using pure alcohols as the solvents while modifying the process by adjusting other parameters, and (2) modifying the precursor solution while keeping other parameters fixed. The results regarding the first aspect will be presented first for each burner, followed with the results regarding the second one.

### 5.1.1 Pure alcohols as solvents

Because the synthesis process is very dependent on the experimental setup, this section will be divided into two parts, each dedicated for one of the burner designs and specific setups. The results from the two cases will then be compared to each other.

#### The LR burner

In **Publication I**, samples with different parameters were produced with the LR burner to study possible factors affecting the crystallographic phase composition of iron oxide particles. The following parameters were fixed (excluding a few samples):

- Iron(III) nitrate nonahydrate ( $\text{Fe}(\text{NO}_3)_3 \cdot 9\text{H}_2\text{O}$ ) was used as the precursor.
- Pure alcohols (methanol (MeOH), ethanol (EtOH) and isopropyl alcohol (IPA)) were used as solvents.
- Fe atom concentration was fixed at 40 mg/ml.
- Precursor liquid feed rate was kept at 2 ml/min, excluding a few samples.

The gas flows were the main parameters that were adjusted to control the phase composition. The atomizing oxygen flow was varied between 15 and 35 l/min, and the hydrogen flow between 20 and 60 l/min. Because the liquid feed rate was very small compared to the gas flow rates, the  $\text{O}_2/\text{H}_2$  flow ratio primarily defined  $\Phi$ , which was concluded as the best factor determining the phase composition. The three chemically fairly similar alcohols with varying HOC values were chosen to explore if the phase formation process is sensitive to the energy content of the solvent.

Hematite is easily distinguished from the other iron oxide phases with XRD, but maghemite and magnetite are difficult to tell apart due to their isomorphism. Therefore, we used Raman microscopy in addition to XRD to tell the two phases apart. Figure 5.1a displays the weight fraction of maghemite calculated with Rietveld analysis as a function of  $\Phi$ , and Figure 5.1b shows two Raman patterns recorded from the sample marked in Figure 5.1a. These patterns are very typical for hematite and maghemite, and the characteristic peaks are marked in the graph. Optical images pointing out the measurement locations are also presented.

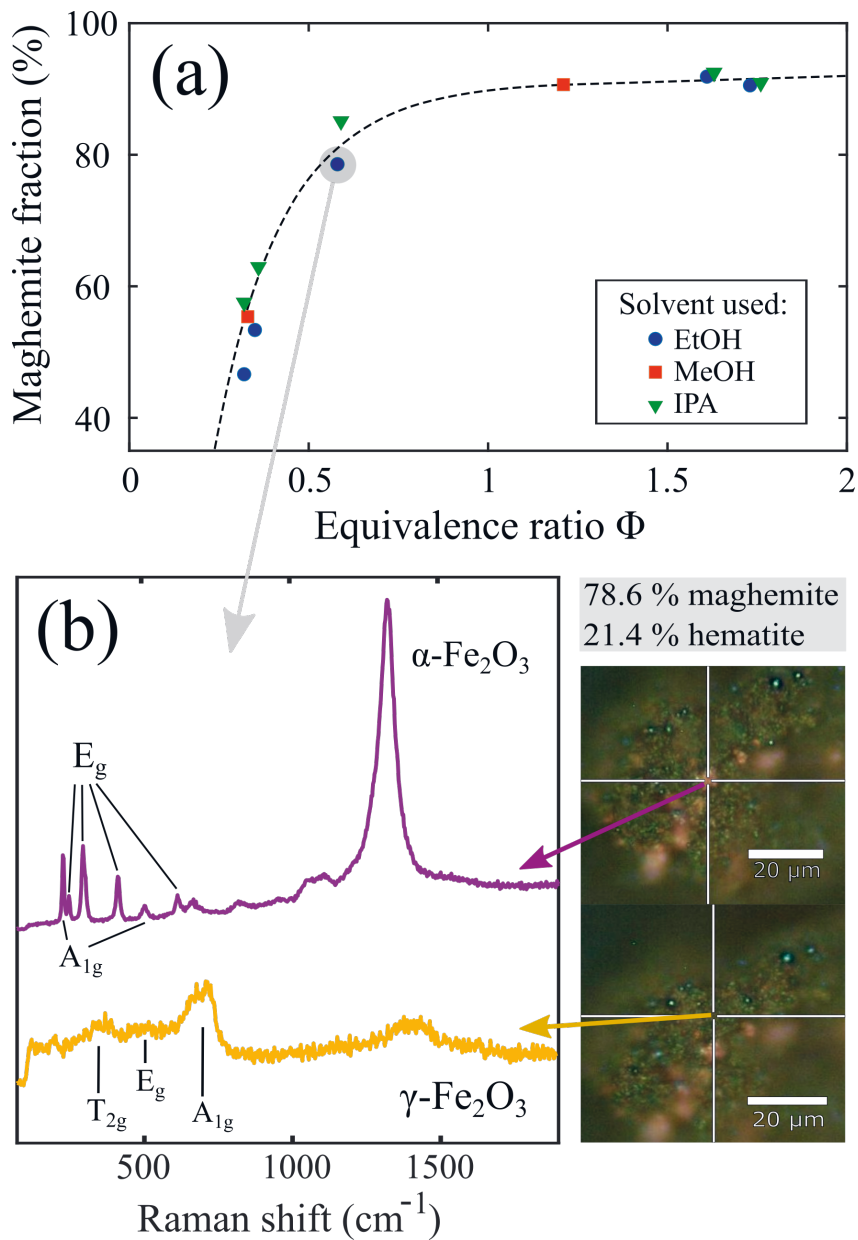


**Figure 5.1** (a) The weight percentage of maghemite as a function of equivalence ratio in the samples synthesized using different alcohols as solvents, and (b) two Raman spectra recorded from the indicated locations in the optical microscope images. The two spectra are typical for hematite and maghemite, and their characteristic peaks are marked. (Adapted from **Publication I**)

In the low end of the curve, the maghemite fraction seemed to follow  $\Phi$  quite linearly, but it saturated somewhere between 0.5 and 1. This could be due to oxygen diffusion from the surrounding atmosphere, which would be assumed to increase, when the amount of oxygen fed to the flame decreases. This would also mean that the actual equivalence ratio would stray further from the theoretical value.

The choice of the solvent did not seem to have a huge effect on the phase ratio, even though samples produced with IPA (higher HOC compared to EtOH and MeOH) mostly contained the largest maghemite fraction. However, even the slight impact of HOC is difficult to conclude based on these results, since EtOH with higher HOC than MeOH falls lower on the curve. The chemical differences between the solvents possibly have a more pronounced effect here. A few extra IPA and EtOH samples were produced with differing liquid feed rates: 4 ml/min with the highest  $\Phi$  (corresponding to the rightmost circle and triangle in Figure 5.1a) and 1 ml/min with the lowest  $\Phi$  (corresponding to the leftmost circle and triangle in Figure 5.1a). Because no drastic differences were observed, the phase composition does not seem to be very sensitive to the liquid feed rate either.

The Raman measurements confirmed that the non-hematite part of the samples consisted primarily of maghemite. However, the one clear peak in magnetite's Raman spectrum overlaps with the strongest peak of maghemite at around  $700\text{ cm}^{-1}$ , so the possibility of a small amount of magnetite can not be ruled out. An interesting phenomenon was observed with the measurement, as it seemed that the phases could be somewhat distinguished in the optical micrographs. Bright yellow areas gave a hematite pattern and brown/green areas a maghemite pattern, while colours somewhere in between gave a mixture of the two patterns. In samples with lower amounts of hematite, the yellow areas seemed quite large and very localized, which indicates that the hematite particles accumulated together for some reason, and possibly included larger particles. When the hematite fraction increased, the colours more or less blended together, forming a more uniform appearance.

TEM imaging was performed to study the particle size distributions of the samples. Not every sample was imaged, but the whole equivalence ratio range was covered. The images were used to estimate average PP sizes by choosing random areas and measuring all discernible particles (not counting clearly larger residual particles). Figure 5.2a shows TEM micrographs that represent most of the imaged area for all samples, and Figure 5.2b the calculated average PP sizes for a few different imaged



samples with varying  $\Phi$  values. Figure 5.2c shows some collections of larger particles that were found.

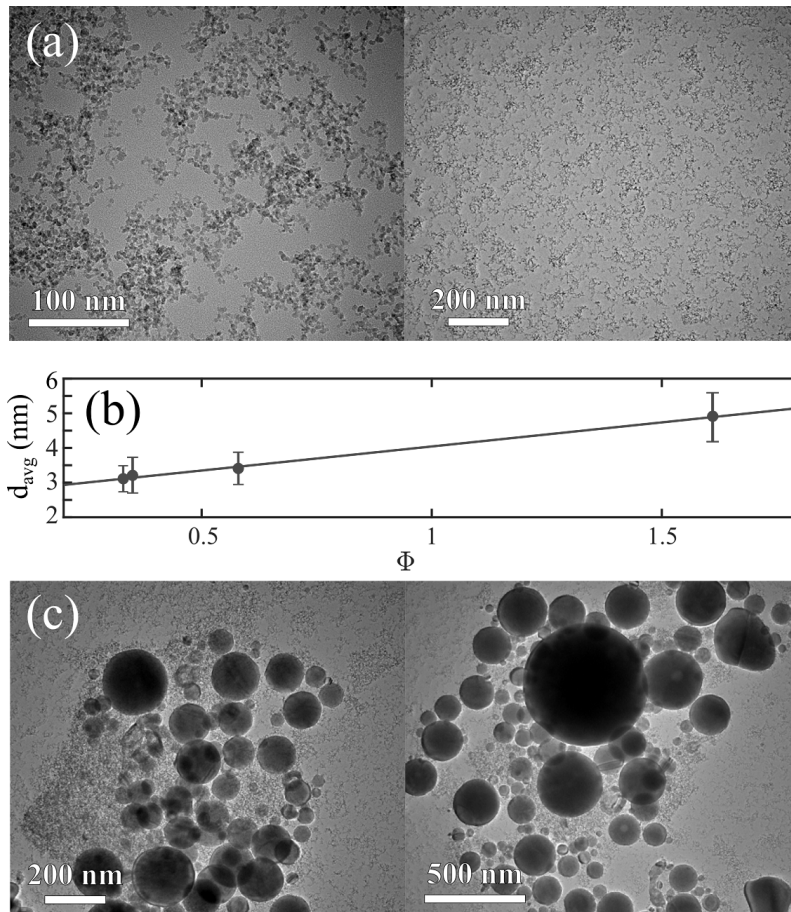


**Figure 5.2** (a) TEM images representing most of the sample area, (b) the average PP size calculated from the images as a function of  $\Phi$ , and (c) some larger residual particles found in the TEM samples. (Adapted from **Publication I**)

The fine particle mode shown in Figure 5.2a was clearly dominant across all TEM samples, and the PP sizes increased quite linearly with growing  $\Phi$ , which is depicted in Figure 5.2b. There are supposedly two main factors affecting the PP size in this case: the residence time and the total residual particle volume. A larger  $\Phi$  lengthened the flame, thereby increasing residence time. If less residuals form, more material is available for nucleation and particle growth. Since more large particles were found in the samples with lower  $\Phi$  values, a combination of these two effects is probable.

However, since TEM images always represent a very small portion of the whole powder sample, so we can not tell to which extent these two factors contribute.

## The KP burner

The starting point of **Publication II** was overcoming the restriction in the amount of oxygen that could be fed into the flame with the LR burner. With a single atomizing oxygen flow, the flow rate could not be raised beyond a certain point while maintaining stable burning, so we switched to the KP burner that allows a more flexible gas flow setup. The total oxygen flow rate was then increased by adding a secondary oxygen flow. Figure 5.3 shows the specific gas flow setup chosen for the KP burner in **Publication II**.

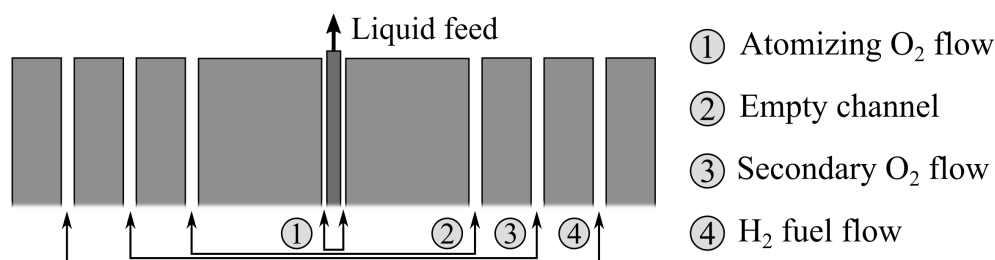


**Figure 5.3** The gas flow setup chosen for the KP burner. (**Publication II**)

The different gas flows can obviously be arranged in several ways, but every configuration does not work equally well. Some experimentation was conducted before choosing this specific setup. If the secondary oxygen flow was placed in channel 2, or the hydrogen flow between the two oxygen flows, a significant amount of solid material accumulated on the burner head. This was assigned to swirling flows directed towards the liquid channel. The chosen setup offered the most stable synthesis. The hydrogen flow could also be used for atomization, like in most published LFS studies, but it is less efficient for atomizing compared to oxygen. Therefore, larger  $H_2$  flow rates would be required for efficient atomization. This would in turn increase the equivalence ratio, which would be counterproductive regarding the goal of reaching lower  $\Phi$  values.

The atomizing oxygen flow rate  $Q_{at}$  was varied between 5 and 15 l/min, and the secondary flow so that the total oxygen flow  $Q_{tot}$  settled between 20 and 65 l/min. This resulted in a  $\Phi$  range of 0.10–0.33, whereas for the LR burner in **Publication I**,

a range of around 0.32–1.76 was covered. The hydrogen flow was fixed at 10 l/min, so  $\Phi$  was only adjusted through  $Q_{tot}$ . The liquid feed rate was also here maintained at 2 ml/min as in **Publication I**, but the Fe atom concentration was lowered from 40 to 30 mg/ml to ensure that the additives used in the second part of the results completely dissolved in the precursor solution.

Figure 5.4 shows the maghemite fraction as a function of  $\Phi$  obtained from the XRD data with Rietveld analysis. The results for the LR burner from **Publication I** are plotted in the same graph for reference. Because the total oxygen flow can be divided in several ways between the two channels, samples with equal equivalence ratios but differing flow setups were produced. These samples are marked with the total flow rates in grey boxes.

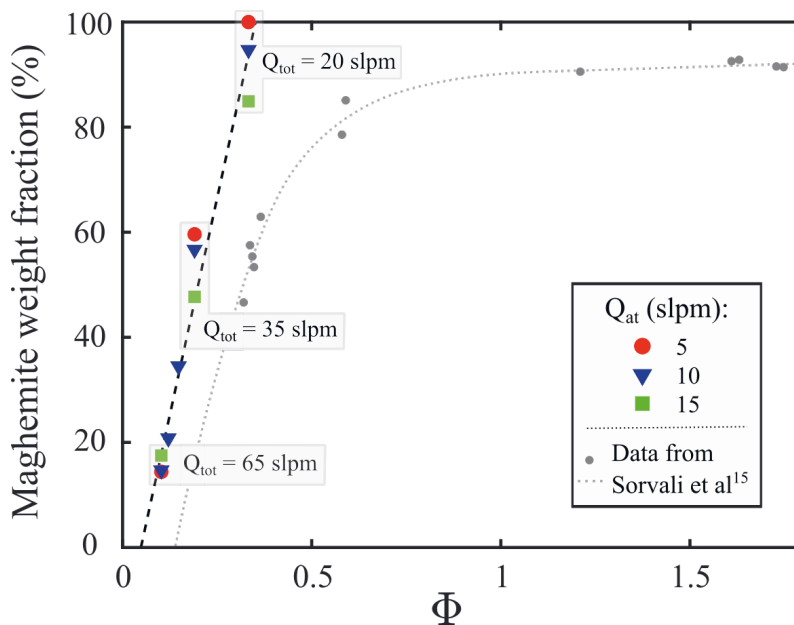


**Figure 5.4** The maghemite fraction as a function of equivalence ratio. Three different total oxygen flows with differing atomization flows are marked, and the results obtained for the LR burner in **Publication I** are plotted for reference. (**Publication II**)

The maghemite fraction correlated again strongly with  $\Phi$ , but the curve was a little different from the one measured for the LR burner. The relationship was quite linear through the whole range, whereas saturation was observed earlier. This could result from the structural difference between the two burners. The flame zone is probably more shielded from the surroundings with KP burner, as the liquid jet is

surrounded by two annular gas flows, whereas LR burner has fine discrete H<sub>2</sub> channels as described in Section 3.1. This could help entrainment air enter the flame zone earlier compared to the KP burner. Another discrepancy between the curves is a clear shift towards lower equivalence ratios. Consequently, even pure maghemite was observed with  $\Phi \approx 0.33$  that resulted in about 1:1 phase ratio with the LR burner. It is difficult to tell the cause for this shift, but the structural difference in the gas channels could also here be a part of the explanation. If the entrainment is stronger already in the lower part of the flame for the LR burner, this could lower the actual equivalence ratio there. It would also make sense that the difference to the KP burner grows with  $\Phi$ , as the entrainment air has a larger effect. However, extensive flow simulations would be required to confirm the details. There was some variation among the samples where the same total oxygen flow was divided differently between the two gas channels, but none of the data points deviated considerably from the linear fit. Higher atomization flow rates promoted a slightly greater hematite fraction.

We also wanted to see how the SSA correlates with the phase composition, since it reflects the particle size distribution and particle morphology. To examine these, BET measurements were performed alongside TEM imaging. Figure 5.5 shows the SSA as a function of total oxygen flow and TEM images of some residual particles from certain samples indicated in the graph. Most of the imaged particles could be categorized either as primary or residual particles. The PP mode consisted of a reasonably narrow size distribution below 10 nm, but the residual mode comprised a much wider range of considerably larger sizes. Both particle modes contributed to the SSA values. The highest SSA value of 87 m<sup>2</sup>/g refers to a calculated average particle size of about 13 nm, which implies that all the samples included at least some residual particles.

The drop in SSA from 20 to 35 l/min was assumed to mainly arise from an increase in residual particle volume. After this, the situation gets more difficult to interpret. When the secondary flow was raised from 25 to 35 and 45 l/min with the atomization flow being 10 l/min, the SSA still slightly decreased, but then clearly rose for the highest oxygen flow in all cases. Since the TEM samples with 65 l/min total oxygen flow were dominated by residual particles, the increase in SSA unlikely reflects a decrease in residual volume. The reason behind this could be the increase in the number of hollow particles that seemed to get more prevalent with the growing oxygen flow. Hollow particles raise the SSA due to their low effective density. That

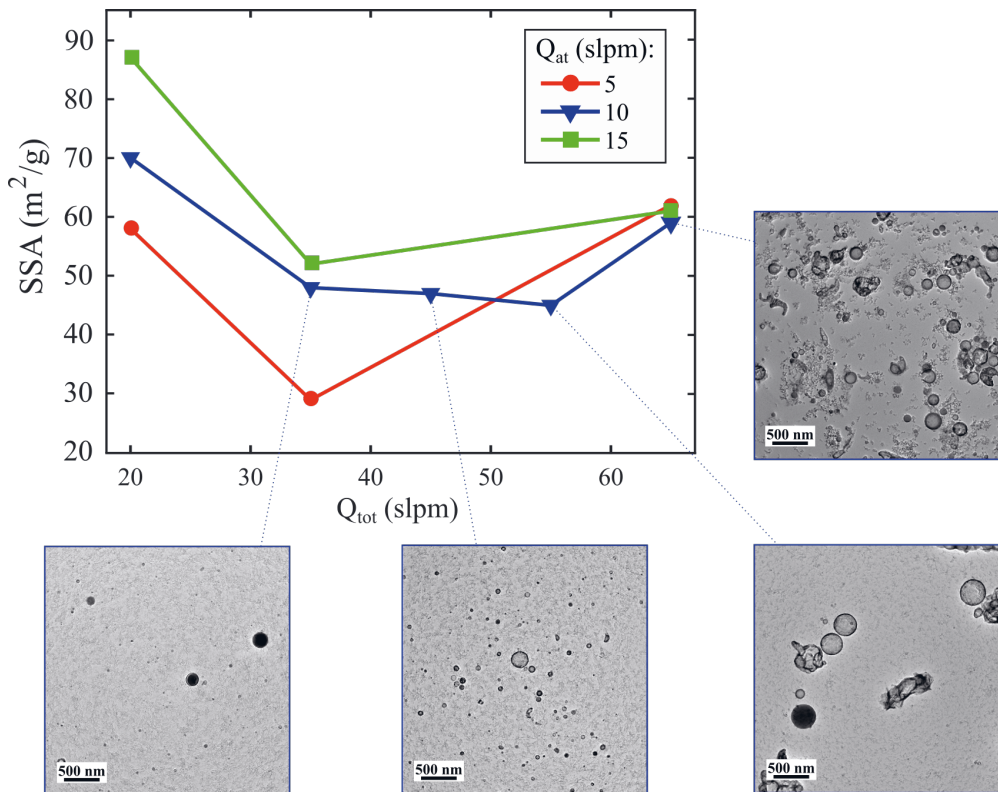


**Figure 5.5** The specific surface area as a function of the total oxygen flow, and TEM images of some residual particles from the marked samples. (Adapted from **Publication II**)

would also indicate a possible correlation between hollow particles and the hematite fraction.

Discrepancies were observed in SSA among samples with varying atomization flow rates, higher values generally promoting larger SSA. This was assumed to originate mainly from differences in PP size. For the 20 l/min total oxygen flow samples, where the average PP sizes could be calculated from TEM images, the average size decreased with increasing atomization flow, which translates to a larger SSA. One of the main factors causing this was most likely flame contraction that occurred, when more of the total oxygen flow was placed in the atomization channel. Especially for lower total oxygen flows, the difference between the flame lengths was quite large. Also, the Rietveld results showed a correlation between atomization flow rate and hematite fraction, which could imply more hollow particles.

Our results indicate that even though  $\Phi$  is a good base measure for predicting the phase ratio, the actual relationship is dependent on the burner design and the gas flow setup. There also seems to be a difference between the two burners in the composition range that is attainable.  $\Phi$  is only a single number to describe the whole synthesis process, and it does not take into account the local conditions that most likely depend on the experimental setup. As was hypothesized earlier, the difference in the structure and dimensions of the gas channels could have an impact on the equivalence ratio in different parts of the flame zone. They also likely affect the local gas velocities and temperatures, which are assumed to strongly influence the reaction kinetics in the flame. A thorough measurement of the temperature fields in each case would help assess the role of temperature. For the local gas velocities, simulations could prove to be a great asset. Another possible factor besides the gas channel structure is the diameter of the liquid channel. When the diameter is increased (KP vs LR burner), a larger fraction of the precursor solution in the core of the liquid jet comes in contact with the atomizing oxygen gas later compared to a smaller liquid channel. This could definitely have an impact on the oxidation kinetics. Other alterations to the burner and gas flow setup would also be interesting to study, as that would give more insight into the fundamental processes of the synthesis.

### 5.1.2 Modifying the composition of the precursor solution

Another perspective for controlling the phase composition was modifying the composition of the precursor solution. In **Publication I**, the LR burner was used, and part of the alcoholic solvent was substituted with different carboxylic acids, resulting in a mixed solvent. In **Publication II**, citric acid (CitA) and oxalic acid (OxA) were dissolved in the precursor solution as additives, while using the KP burner. The carboxylic acids used were liquids, so they worked as solvents, whereas CitA and OxA are solid compounds that need to be dissolved in a solvent themselves, which gives a certain distinction between the two compound groups.

#### Carboxylic acids

The gas flows for studying the effect of carboxylic acids were chosen as 35 l/min of O<sub>2</sub> for atomization and 20 l/min of H<sub>2</sub> for the LR burner. These parameters resulted in around 50 % of hematite with pure MeOH as the solvent, so the shift

towards either phase would be easily detected. Butanoic acid (ButA) and propanoic acid (PropA) were mixed with MeOH in a 1:1 volumetric ratio. 2-ethylhexanoic acid (EHA) was mixed in a few different amounts (5, 15, 30 and 50 vol-%) to see if the solvent mixing ratio has a significant effect on the particles. EHA has earlier been used for getting rid of residual particles in flame synthesis and causing disruptive droplet burning in single droplet experiments (Harra et al. 2017; Rosebrock, Riefler et al. 2013; Strobel and Pratsinis 2011).

All of the samples with a carboxylic acid addition showed exclusively maghemite peaks in the XRD measurements, so even the smallest addition of 5 vol-% of EHA resulted in the elimination of the hematite phase. However, there were clear discrepancies in the XRD peak shapes and widths between samples, which indicates differences in particle properties. Therefore, the EHA samples were also characterized with TEM imaging, which is illustrated in Figure 5.6. The top row shows primary particles and the bottom row the largest collections of residual particles found in all of the different EHA samples.

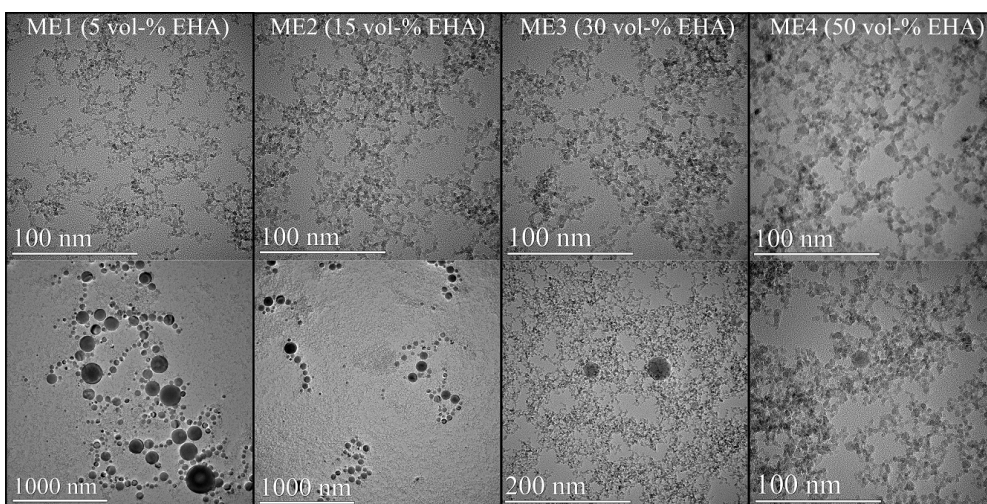


**Figure 5.6** TEM images of samples with various EHA fractions in the solvent mixture. (Publication I)

The amount and the size of the residual particles seemed to decrease with the growing EHA fraction in the precursor solution. This was also supported by the inspection of the PP sizes, which increased simultaneously. Since the gas flows, which for the most part determine the flame length, the residence time and  $\Phi$  were fixed for all samples, the only apparent reason for the PP growth is the reduction in resid-

ual particle volume. As the precursor evaporates more efficiently, the end product concentration increases, thereby enhancing PP growth through condensation. The explanation for the reduction is not certain, but it could be connected to the HOC of the precursor solution. Figure 5.7 shows the PP sizes calculated from TEM images for all the EHA samples and the PropA sample as a function of the HOC of the precursor solution.

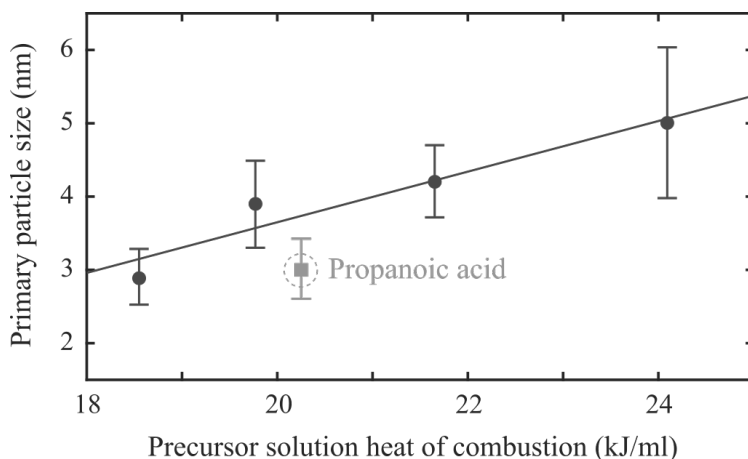


**Figure 5.7** The PP sizes calculated from TEM images for different EHA samples (blue) and the PropA sample as a function of the precursor solution HOC. (Adapted from **Publication I**)

The PP sizes increased quite linearly for the EHA samples, when they were plotted against the HOC of the precursor solution. However, the PropA sample strays from the curve a bit more. One possible cause for this could be the difference in boiling point of PropA compared to EHA. Jossen, Pratsinis et al. 2005 claimed that a large ratio of solvent boiling point to the precursor melting/decomposition point would promote the formation of homogeneous nanomaterial. Since the boiling points for PropA, ButA and EHA are 141.5, 163.8 and 288.1°C, respectively, the results would follow this logic.

There are a few possible explanations for the carboxylic acids erasing the hematite phase. It has been suggested that elevated temperatures would lead to the formation of metal complexes when using nitrate precursors (Chiarello, Rossetti, Forni et al. 2007). When adding carboxylic acids, metal carboxylates could form, which might not have a reaction pathway to hematite. Another possibility could be hematite formation through hydrolysis in the liquid droplets. If the hematite forms due to water



condensation on the droplets for pure alcohol samples, the carboxylic acids could prevent this by inhibiting water condensation. Inhibition of hydrolysis/condensation reactions by EHA has been observed for titanium isopropoxide (Meierhofer et al. 2017). The simultaneous decrease in residual volume could be the result of microexplosions in the precursor solution droplets that have been observed for instances where EHA has been added to the precursor solution (Rosebrock, Riefler et al. 2013; Rosebrock, Wriedt et al. 2016).

### Citric acid and oxalic acid

We chose 10 l/min atomization flow, 25 l/min secondary oxygen flow and 10 l/min hydrogen flow for the KP burner to study the effect of citric acid and oxalic acid in the precursor solution. Even though we used another burner and a lower equivalence ratio than for carboxylic acids, these parameters give a good reference point against those results due to the very similar phase compositions obtained for the corresponding pure alcohol samples (42–45 % of hematite in both cases).

Samples with a few different amounts of the additives were fabricated in order to inspect possible mixing-ratio-dependent effects. Two OxA samples were mixed with the additive-to-precursor mass ratio of 0.12 and 0.46, and three CitA samples with the mass ratio ranging from 0.15 to 1. Figure 5.8 presents the measured XRD patterns for all samples with the corresponding hematite fractions and SSA values.

Both of these additives brought about a similar effect than a small partial substitution of EHA. They basically eliminated the hematite phase, but for especially OxA, the effect was clearly dependent on the amount of the additive, a smaller amount resulting in a higher hematite fraction. CitA erased the hematite phase more efficiently, since a smaller addition was adequate for producing practically pure maghemite.

No notable dissimilarities were observed in the PP sizes between the samples. However, the SSA values draw a very interesting discrepancy between the two additives. CitA slightly raised the SSA, but OxA lowered it to almost half compared to the pure methanol sample. Since the PP mode seemed very unlikely to have caused this difference, the effect probably emerged from the residual mode. The only suggestion for the cause from the results was found from TEM images. The oxalic acid samples, and especially OxA 2, seemed to contain a third particle mode that consisted of solid particles in the size range of about 10–50 nm. These particles could

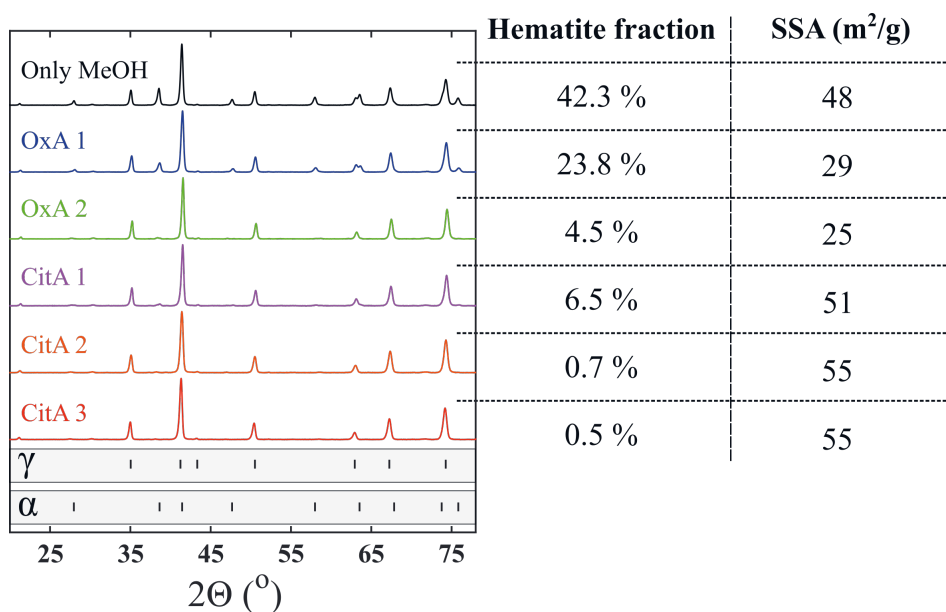


**Figure 5.8** The XRD patterns of oxalic acid and citric acid samples with the corresponding hematite fractions and specific surface areas. The growing number refers to an increasing amount of the additive in the precursor solution. The most important reflections for maghemite ( $\gamma$ ) and hematite ( $\alpha$ ) are marked in the bottom. (Adapted from **Publication II**)

be found quite evenly spread throughout the TEM sample area. The cause for emergence of this sort of a mid-sized particle mode is unknown, but it could be the main factor explaining the drop in the SSA.

Since no studies were found in the literature using similar additives in flame synthesis, the outcome was difficult to predict beforehand. Some iron oxide studies exist, however, that have utilized citric acid and oxalic acid in different synthesis methods. Based on this literature, maghemite would have been the more expected phase to be obtained with citric acid (Kotsyubynsky et al. 2015; Mou et al. 2010), but most of the syntheses mixing oxalic acid with the precursor resulted in hematite particles (Ba-Abbad et al. 2017; Muruganandham et al. 2011; Pant et al. 2009; Yatsenko et al. 2012). Therefore, the results for oxalic acid were somewhat surprising, and the effect of additives seem to depend on the type of synthesis.

## 5.2 MR fluids

Three MR fluids were prepared in **Publication III** by adding micron-sized carbonyl iron (CI) particles and iron oxide nanoparticles to a silicone oil that acted as the carrier fluid. One of the MR fluids was monodisperse, only containing micron-sized CI particles, and for the other two, 5 % of the CI particle volume was substituted with LFS-made maghemite nanoparticles to counteract sedimentation. The total volume of the particles was 15 % percent of the whole MR fluid volume for all fluids. Lecithin was added as a surfactant to prevent nanoparticle agglomeration. It was also added to the sample with only CI particles in order to account for its possible effects.

### 5.2.1 Nanoparticle synthesis and characterization

Two sets of iron oxide nanopowder were produced from ferrocene ( $\text{Fe}(\text{C}_5\text{H}_5)_2$ ) dissolved in xylene with the LR burner, hydrogen being the atomization gas. The differing parameter for the two batches was the feed rate of the precursor solution. This resulted in a size difference for the primary particles, the sample with the lower feed rate (Nano1) having a smaller average PP size than the one with the higher feed rate (Nano2). Both powders were confirmed to consist of maghemite with XRD and Raman analyses. Figure 5.9 shows TEM images of the two nanopowders.

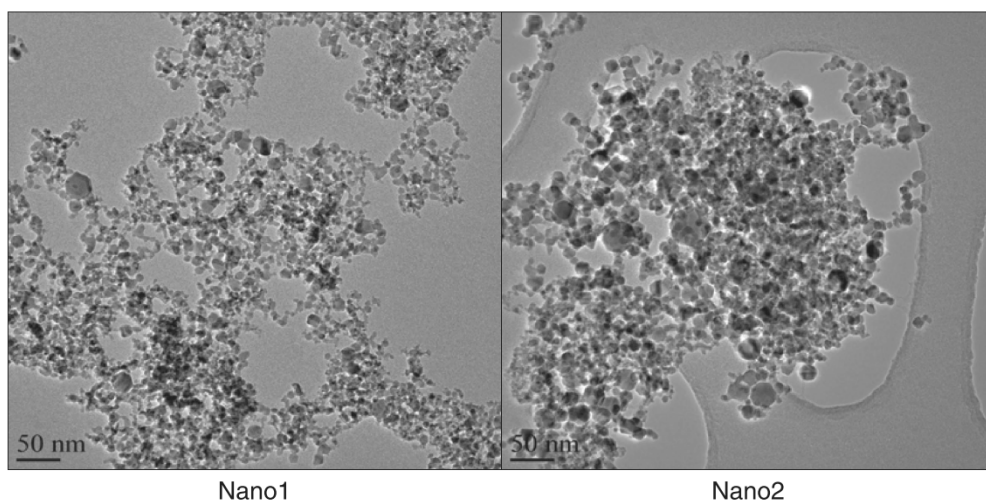


**Figure 5.9** TEM images of the two nanopowder samples. (**Publication III**)

The particles were mostly spherical and contained a spectrum of different sizes up to about 50 nm. A manual calculation of random particles in the TEM images resulted in arithmetic mean particle sizes of 7.9 and 16.6 nm for Nano1 and Nano2, respectively. The particles were significantly aggregated and agglomerated, and this was observed to be slightly stronger in Nano2.

Both powder samples showed saturation magnetizations clearly lower (22 and 43  $\frac{\text{Am}^2}{\text{kg}}$ ) compared to bulk maghemite (74  $\frac{\text{Am}^2}{\text{kg}}$ ), which was expected for nanosized particles. At room temperature, the virgin magnetization curves for both samples agreed well with the Langevin function, and the measured coercivities were zero, which indicates superparamagnetic behaviour.

### 5.2.2 Sedimentation behaviour and MR performance

When the magnetic particles started to sediment, an interface formed between the clear carrier fluid and the particle suspension. The sedimentation behaviour was assessed by tracking this interface from photographs taken once per hour of a 5 ml MR fluid sample. Since the inhibition of sedimentation without impairing the magnetic response of the MR fluid was the main goal of the nanoparticle addition, it is sensible to observe the sedimentation rate in conjunction with the magnetic response. Figure 5.10 shows the sedimentation rate and the dynamic yield stress as a function of magnetic flux density for the different MR fluids. The sedimentation curve labelled "Micro" was added from a previous study by Jönkkäri, Matti et al. 2015. It refers to a sample without the addition of nanoparticles or lecithin, and shows that lecithin has an impact on the gravitational settling on its own. The "Micro + lecithin" curve refers to the monodisperse MR fluid prepared for **Publication III**. The dynamic yield stress refers to the stress needed to break the particle chains and make the material flow freely.

The addition of nanoparticles lowered the sedimentation rates significantly, the average rate for the first 100 h decreasing from 42 nm/s for the monodisperse fluid to 9 and 12 nm/s for Nano1 and Nano2, respectively. Simultaneously, the magnetic response remained almost intact. Low magnetic flux density resulted in a slightly higher dynamic yield stress for the monodisperse fluid, but the difference tilted in the other direction for higher flux density values. Most of the differences between the samples fall inside the standard error, so the effect of nanoparticles on the dy-

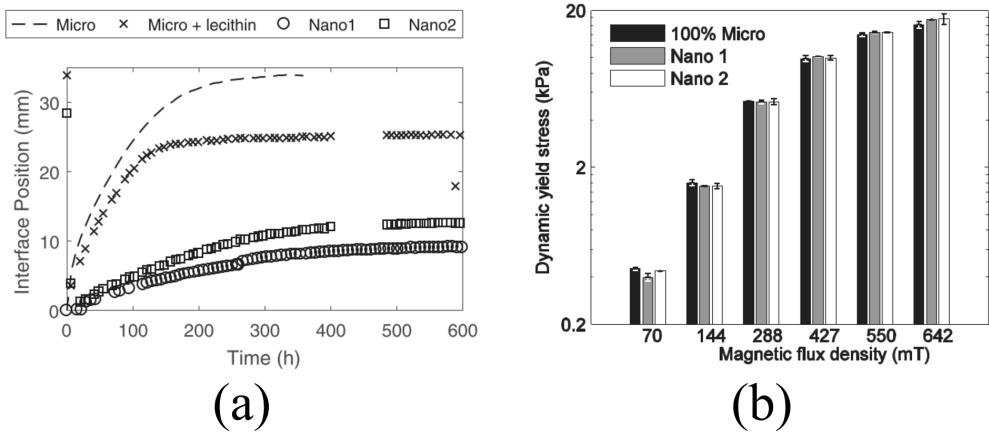


**Figure 5.10** (a) The interface position as a function of time and (b) the dynamic yield stress as a function of magnetic flux density for the different MR fluids. The curve labelled "Micro" was taken from Jönkkäri, Matti et al. 2015, and it applies to an MR fluid without nanoparticles or lecithin. (Adapted from **Publication III**)

dynamic yield stress can be deemed negligible. However, a change in the deformation behaviour was observed. According to the oscillatory measurements, the elastic part of the deformation decreased, while the viscous part increased with the addition of nanoparticles.

Sedimentation rates have been earlier tested with a similar addition of commercial iron nanoparticles with an average particle size of 50 nm, but only a minor improvement was observed (Jönkkäri, Matti et al. 2015). Therefore, the lower particle size seems to be a key factor in hindering sedimentation. One possible explanation is that the larger total surface area of the particles increase the drag between the particles and the carrier fluid.

Another notable phenomenon arising with the nanoparticle addition was that the bidisperse MR fluids seemed to settle to considerably lower packing densities than the monodisperse MR fluid, if we assume the settling final at 600 h. This could facilitate resuspension of the particles after a long storage period. A dense concretion of particles in the bottom is far more challenging to resuspend effectively. The flip side of the nanoparticle substitution was the effect on the off-state viscosity, which is presented in Figure 5.11.

The values were 29–84 % higher for Nano1 and 23–52 % higher for Nano2 when comparing to the monodisperse fluid, with the highest discrepancies occurring at

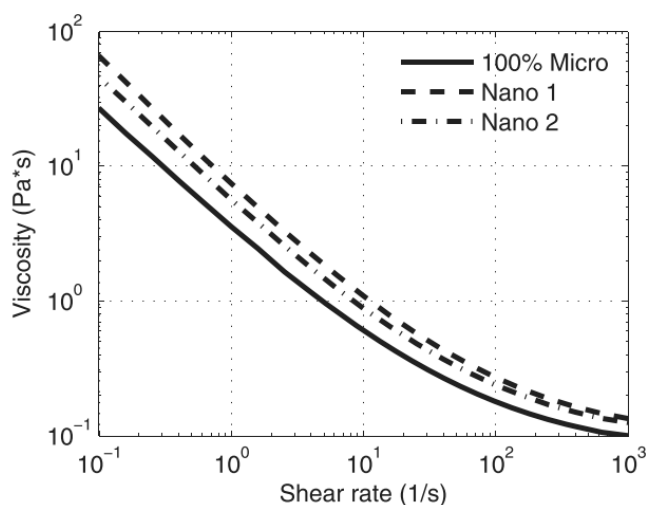


**Figure 5.11** The off-state viscosity as a function of shear rate for the different MR fluids. (**Publication III**)

lowest shear rates. Depending on the application the MR fluid is to be used in, this can be undesirable. The increase in viscosity is understandable considering that according to Rudyak and Krasnolutsii 2014, nanofluids are well established to have higher viscosities than conventional suspensions. Therefore, a partial nanoparticle substitution should induce a similar effect. Also, they claim that viscosity should increase with decreasing particle size, which is also consistent with these results. The produced MR fluids show great promise for applications.

### 5.3 Omniphobic nanocoating

The initial goal in **Publication IV** was to produce a nanocoating on a stainless steel surface that would optimally repel all liquids, be as thin as possible, and have acceptable stability. A multilayered coating was designed for this purpose, and the fabrication process is described in Figure 5.12 in four distinct steps.

The first step was cleaning the substrate carefully with various solvents. LFS was then used to deposit  $\text{TiO}_2$  particles on the surface to produce a nanostructure that would enable efficient omniphobicity. The particle material and the process parameters were chosen so that a well predictable structure could be achieved. Hydrogen was used as the atomizing gas with the LR burner, as in **Publication III**. The form-

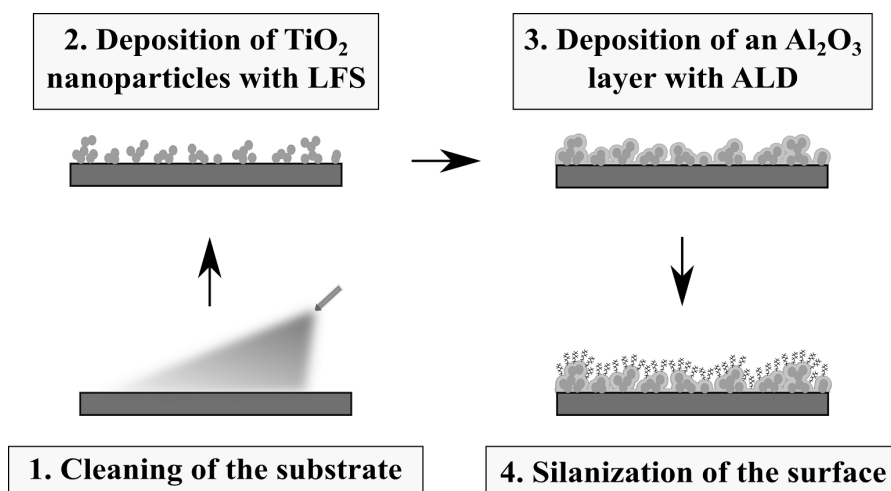


**Figure 5.12** The stepwise fabrication process of the multilayered omniphobic coating. (Adapted from Publication IV)

ing nanomaterial was directed through a so-called residence tube before reaching the substrate. The main purpose of the residence tube was to even out the particle flux on the whole surface area to be coated, scavenge possible large residual particles, and lower the temperature, so that the substrate would not be affected by the heat.

The third step was coating the LFS-treated surface with a thin Al<sub>2</sub>O<sub>3</sub> layer using ALD. In an ALD process, a conformal coating accumulates one atomic layer at a time, so it was able to penetrate the porous nanoparticle layer, ultimately covering the whole surface area. The idea was that the alumina would enter the contact areas between the substrate and the particles, reinforcing their adhesion along with strengthening the cohesion of the particle layer. However, the thickness of the ALD layer had to be low enough, so that the nanostructure would not be buried underneath. The samples were oxidized in mixtures of oxygen and nitrogen at 300°C to remove all organic impurities before introducing the reactants onto the surface.

The final step was covering the surface with fluorosilane (heptadecafluoro-1,1,2,2-tetrahydrodecyl trichlorosilane specifically) molecules in a liquid phase deposition process in order to lower the surface energy of the final coating. Before silanization, the ALD-coated samples were irradiated with UV-C light (peak wavelength at 254 nm) to remove possible contaminants, since it was observed to decompose organic material even in the absence of a photocatalyst.

### 5.3.1 Characterization of the coating

Since the process proceeded in a stepwise manner, mid-process characterization was performed in addition to analyzing the final coating. The samples were imaged with SEM after each step from the top to see how the topography evolved during the process. Figure 5.13 shows SEM images of the coating after fabrication steps 2, 3 and 4.

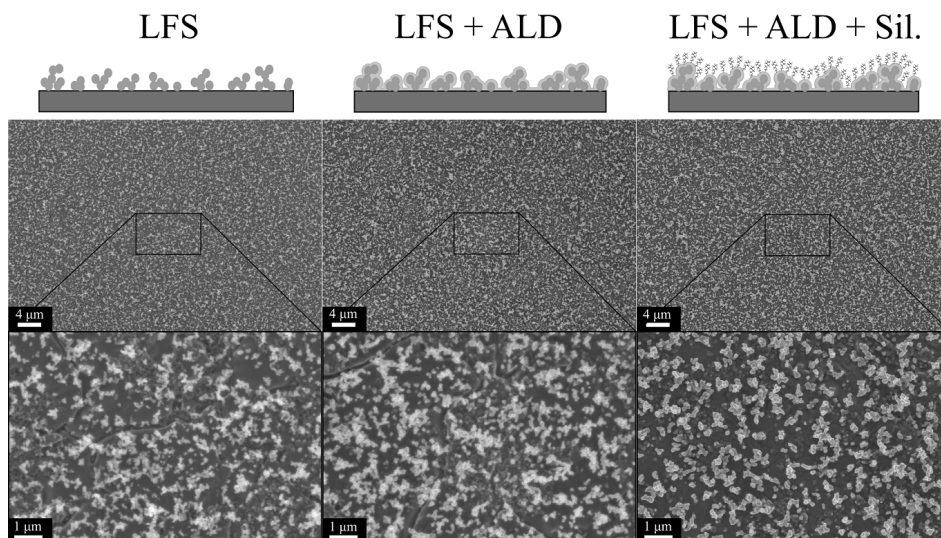


**Figure 5.13** SEM images after fabrication steps 2, 3 and 4. (Publication IV)

The nanoparticles mostly occurred on the surface as agglomerates or aggregates with an average PP size of around 50 nm, surface coverage being far from complete. Graphical analysis with ImageJ program calculated the coverage as ca. 30 % with automatic thresholding. The produced 10 nm ALD layer had no noticeable impact on the appearance of the coating in microscale. The growth of the particles could, however, be clearly observed from the SEM images with higher magnifications. Also, the silanization had very little effect on the surface topography, as suspected.

The thickness of the coating could not be determined from the top view SEM images, so FIB-SEM was used to study it cross-sectionally. A gold layer was sputtered onto the coating to enhance conductivity and a platinum layer was deposited on top of that to protect the coating during the milling process with  $\text{Ga}^+$  ions. Figure 5.14 shows a cross-sectional SEM image of the coating along with an Al  $\text{K}\alpha 1$  signal from



an EDS scan.

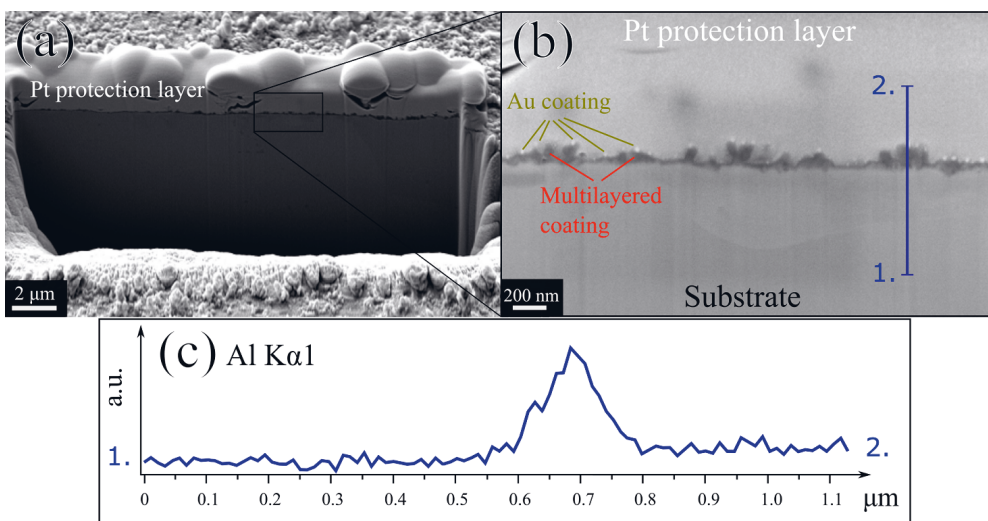


**Figure 5.14** (a)(b) SEM images of the cross-section with different magnifications, and (c) the EDS signal of Al K $\alpha$ 1 across the line marked in (b). (Adapted from **Publication IV**)

The coating is visible through the whole cross-section in Figure 5.14a. The higher magnification image in Figure 5.14b reveals the actual coating in more detail. In the SEM images, the gold layer appears as bright spots, and the platinum as a thick layer on top. The nanostructure undulates between 10–15 nm (areas with only ALD) and 160–200 nm in thickness. If we imagine a flat and even coating with the cross-sectional area calculated from the SEM images, this results to an average coating thickness of  $\sim 70$  nm. Both the estimated maximum thickness and the calculated average thickness are lower than any reported values for omniphobic coatings in the literature so far. The EDS curve indicates a good penetration of the ALD layer. Since there is an Al K $\alpha$ 1 signal emanating even from the very bottom of the coating, the alumina can be presumed to have covered the titania particles very efficiently.

XPS analysis performed after each step reinforced the assumption that the ALD coating was even and conformal. Since the thickness of the ALD layer was in the same order of magnitude as the information depth of XPS ( $\sim 10$  nm), an uneven layer would most likely have caused a signal from underneath the alumina layer. However, the measurement of the ALD-coated sample only revealed peaks originating from Al, O and C transitions, in addition to carbon, silicon and fluorine peaks originating from organic impurities and the silane molecules.

### 5.3.2 Assessment of omniphobicity and stability

The liquid-repellency and the coating stability seemed to go hand in hand. A very short LFS coating time or a large ALD thickness led to a reasonably durable but poorly repellent coating. Conversely, a long coating time or a thin ALD layer resulted in good repellency but very poor stability. The final values for both variables were picked to compromise between the two properties.

The performance in liquid-repellency was assessed with two different measures: CA and SA. Test liquids were chosen to represent various surface tension values, since repelling liquids with low surface tension generally requires higher sophistication. Figure 5.15 shows the measured CA values for the chosen 6 s LFS coating time as a function of ALD coating thickness for water ( $H_2O$ ), diiodomethane (DIM), ethylene glycol (EG), olive oil (OO) and hexadecane (HDEC) with four different ALD thicknesses. The SA values represent the final coating with the 10 nm ALD layer discussed so far.

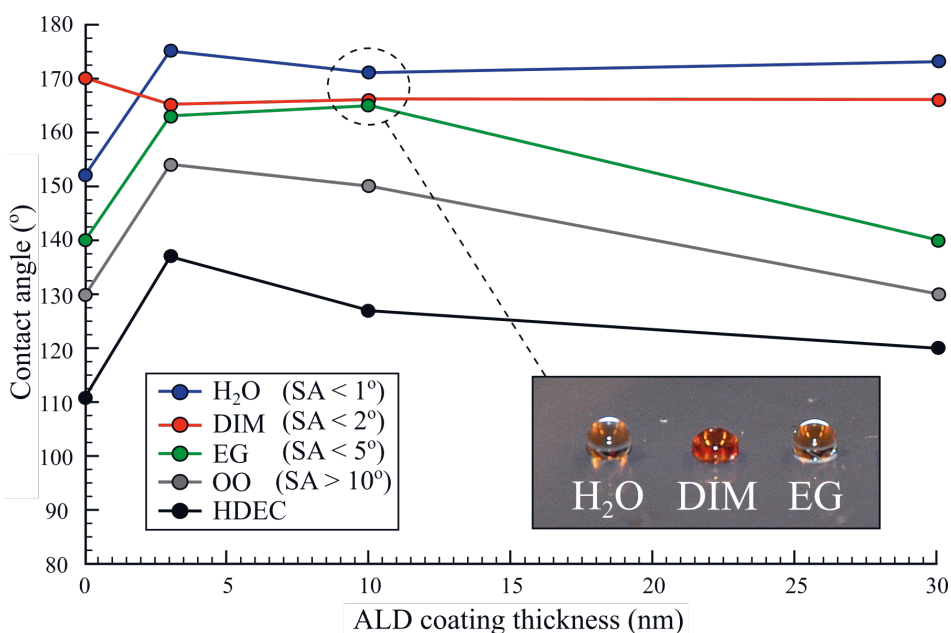


**Figure 5.15** The measured CA values as a function of ALD thickness. The SA values correspond to an ALD thickness of 10 nm. The photo of test liquid droplets refers to the circled data points. HDEC is missing an SA value, because it could not be determined. (Adapted from **Publication IV**)

The 3 nm ALD thickness presented the strongest repellency, while 30 nm thickness already impaired the performance by covering some of the nanostructure. The 10 nm offered the best compromise between repellency and stability, resulting in CA values of over  $160^\circ$  for H<sub>2</sub>O, DIM and EG. However, if repellency against only liquids with higher surface tension was adequate, a thicker ALD coating would probably be optimal.

Another interesting observation from Figure 5.15 is the significant increase in CA values (excluding DIM) from no ALD coating to 3 nm. This indicates that the thin alumina layer provides a superior substrate for silanization compared to the uncoated, LFS-treated surface. All in all, the final coating fulfilled the superphobicity requirements for water, DIM and EG, and can be considered superomniphobic to a certain extent.

The adhesion of the coating to the substrate and its durability was studied with a microscratch test. A small diamond tip was dragged along the surface with varying loads. Unfortunately for the performance of the coating in realistic conditions, already the lowest loads used caused the coating to lose the surface structure and the omniphobicity with it. This indicates poor resistance against abrasion and mechanical pressure. However, the adhesion of the particles to the substrate could not be deemed poor, because the SEM images of the scratch marks implied that the coating mostly just flattened under the pressure rather than detached from the steel substrate.

As was suspected, achieving good stability was the biggest challenge, and it could not be sufficiently fulfilled. The ALD layer improved the stability, but not to point where abrasive wear could be endured. However, the coating could work in conditions where the surface does not confront significant wear. More research is needed to discover ways of improving the endurance.



## 6 Concluding remarks

As the need for large volumes of nanomaterials will continuously be increasing, the methods suitable for that require more research and development. Liquid flame spray, and flame synthesis in general, offers lots of potential for simple fabrication of nanoparticles from cheap precursor, but the process is not adequately well understood yet. This dissertation focused partly on expanding the knowledge on the processes happening in the flame, and partly on exploring its utilization in specific applications.

One of the unclear parts in LFS synthesis is the processes through which the crystallographic phase of the resulting nanoparticles is determined. Since the whole assortment of factors playing their part in this is unclear, a specific case was chosen: studying factors that determine the phase composition of iron oxide particles from iron nitrate. Iron oxide is considered a very important nanomaterial and also very interesting from our point of view, because it occurs in numerous different phases. Two different perspectives were picked for influencing the phase composition: (1) adjusting the gas flow setup in LFS while keeping other parameters constant, and (2) modifying the composition of the precursor solution prior to feeding it to the flame. Two different burner designs were used in the studies.

When the gas flow setup acted as the variable, pure alcohols were used as solvents. All of the samples were observed to consist of two common iron oxide phases: maghemite ( $\gamma\text{-Fe}_2\text{O}_3$ ) or a mixture of maghemite and hematite ( $\alpha\text{-Fe}_2\text{O}_3$ ). The ratio of these two phases was observed to strongly correlate with a measure called equivalence ratio  $\Phi$  that is sometimes used in monitoring the flame synthesis.  $\Phi$  describes the amount of oxygen in the flame compared to stoichiometric burning, values under 1 referring to oxic conditions and values over 1 referring to anoxic conditions. Even though the correlation between the phase ratio and  $\Phi$  was clear with both burners, the relationship was unique to each case, indicating it to be dependent on the burner and the gas flow setup. The phase ratio was not observed to correlate with any other

measure in a simple way, but a possible link between the hematite fraction and hollow particles was inferred. Discovering the fundamental causes for the differences between the burners and the properties linked to the phase ratio require plenty more research.

The effect of precursor solution composition was explored through mixing alcohols and carboxylic acids, and by dissolving citric acid and oxalic acid in the solution as additives. All of these modifications led to a decrease in the hematite fraction, even to its practically complete elimination in most samples. However, the residual particle mode was observed to mostly vanish only in the case larger additions of EHA, but not for other additives or small amounts of EHA. This effect was hypothesized to be connected to the increase in heat of combustion and the differences between solvent boiling points. Disruptive burning of the droplets could also play a part here.

All in all, these results are believed to help understand better the governing factors behind phase formation for iron oxide in flame synthesis. They also suggest that the chemistry connected to the precursor solution might be having currently unknown effects on the FSP process. There is a large research consortium in Germany studying the FSP process at the moment with a standardized burner (Schulz et al. 2019), which will most likely be paramount for understanding the synthesis process in detail in the future. However, experimenting with different types of setups will also play an important role in confirming if the future results apply in general or if they are specific for their experimental setup.

The second part of the dissertation explored the utilization of LFS in two different applications. The first of them was magnetorheological fluids that experience a sudden increase in viscosity after introduction of a magnetic field, and a relaxation when it is turned off. A bidisperse MR fluid was produced by mixing microscale carbonyl iron particles and LFS-generated iron oxide nanoparticles in a non-magnetizable carrier fluid. The function of the nanoparticles was counteracting the particle sedimentation that is a common problem with MR fluids. The nanoparticle addition significantly reduced the sedimentation rate without impairing the MR response. A downside caused by the nanoparticles was an increase in the off-state viscosity. However, the results are promising for further development.

In the other application study, an omniphobic nanocoating was fabricated. The goal was to produce a very thin and somewhat durable coating on stainless steel that

would repel all liquids as well as possible. The coating consisted of a nanoparticle layer deposited onto a cleaned steel substrate with LFS, a stabilizing mid layer produced with ALD, and a top layer of silane molecules to lower the surface energy. This resulted in a very thin coating of under 200 nm, and it repelled efficiently water, diiodomethane, ethylene glycol and olive oil. Therefore, it could be regarded superomniphobic to a certain extent. Unfortunately, scratch testing revealed the surface structure to be fairly fragile against abrasion, as it quite easily flattened out under pressure, which led to losing its omniphobicity. This kind of a coating could be applicable for conditions with low wear. A little thicker ALD layer (10 nm  $\rightarrow$  30 nm) weakened the repellency, but increased the stability. Solving the problem of low stability is probably very difficult with the used methodology alone. The research community working on these topics are continuously exploring ways of producing durable omniphobic coatings that are easy to manufacture.

The application results show that LFS can be used for these types of applications. They also give promise to further development in the future. As the understanding in the formation process deepens, the convenience for different applications also improves.





# References

- Ba-Abbad, M. M., Takriff, M. S., Benamor, A. and Mohammad, A. W. (2017). Size and shape controlled of  $\alpha$ -Fe<sub>2</sub>O<sub>3</sub> nanoparticles prepared via sol-gel technique and their photocatalytic activity. *J. Sol-Gel Sci. Technol.* 81, 880–893.
- Aliofkhazraei, M. (2011). *Nanocoatings: Size Effect in Nanostructured Films*. Springer. 251 pp.
- Aromaa, M., Keskinen, H. and Mäkelä, J.M. (2007). The effect of process parameters on the Liquid Flame Spray generated titania particles. *Biomol. Eng.* 24, 543–548.
- Bhushan, B. and Jung, Y. C. (2011). Natural and biomimetic artificial surfaces for superhydrophobicity, self-cleaning, low adhesion, and drag reduction. *Prog. Mater. Sci.* 56, 1–108.
- Birkenstock, J., Fischer, R. X. and Messner, T. (2003). BRASS 1.0beta: The Bremen Rietveld Analysis and Structure Suite. *Zentrallabor für Kristallographie und Angewandte Materialwissenschaften, Fachbereich Geowissenschaften, University of Bremen*.
- Bossis, G., Laci, S., Meunier, A. and Volova, O. (2002). Magnetorheological fluids. *J. Magn. Magn. Mater.* 252, 224–228.
- Brázda, P., Kohout, J., Bezdička, P. and Kmječ, T. (2018).  $\alpha$ -Fe<sub>2</sub>O<sub>3</sub> versus  $\beta$ -Fe<sub>2</sub>O<sub>3</sub>: Controlling the Phase of the Transformation Product of  $\epsilon$ -Fe<sub>2</sub>O<sub>3</sub> in the Fe<sub>2</sub>O<sub>3</sub>/SiO<sub>2</sub> System. *Cryst. Growth Des.* 14, 1039–1046.
- Cao, S. W., Zhu, Y. J., Ma, M. Y., Li, L. and Zhang, L. (2008). Hierarchically nanostructured magnetic hollow spheres of Fe<sub>3</sub>O<sub>4</sub> and gamma-Fe<sub>2</sub>O<sub>3</sub>: preparation and potential application in drug delivery. *J. Phys. Chem. C* 112.6, 1851–1856.
- Cassie, A. B. D. and Baxter, S. (1944). Wettability of porous surfaces. *Trans. Faraday Soc.* 40, 546–551.
- Chaudhuri, A., Wang, G. and Wereley, N. M. (2005). Substitution of micron by nanometer scale powders in magnetorheological fluids. *Int. J. Mod. Phys. B* 19, 1474–1480.

- Chen, G. and Gomez, A. (1997). Dilute laminar spray diffusion flames near the transition from group combustion to individual droplet burning. *Combust. Flame* 110.3, 392–404.
- Chiarello, G. L., Rossetti, I. and Forni, L. (2005). Flame-spray pyrolysis preparation of perovskites for methane catalytic combustion. *J. Catal.* 236, 251–261.
- Chiarello, G. L., Rossetti, I., Forni, L., Lopinto, P and Migliavacca, G. (2007). Solvent nature effect in preparation of perovskites by flame-pyrolysis 1. Carboxylic acids. *Appl. Catal. B: Environ.* 72, 218–226.
- Chin, B. D., Park, J. H., Kwon, M. H. and Park, O. O. (2001). Rheological properties and dispersion stability of magnetorheological (MR) suspensions. *Rheol. Acta* 40, 211–219.
- Dafinone, M. I., Feng, G., Brugarolas, T., Tettey, K. E. and Lee, D. (2011). Reinforcement of Nanoparticle Thin Films Using Atomic Layer Deposition. *ACS Nano* 5.6, 5078–5087.
- Dutt, M., Ratan, A., Tomar, M., Gupta, V. and Singh, V. (2020). Mesoporous metal oxide- $\alpha$ -Fe<sub>2</sub>O<sub>3</sub> nanocomposites for sensing formaldehyde and ethanol at room temperature. *J. Phys. Chem. Solids* 145, 109536.
- Ellinas, K., Tserepi, A. and Gogolides, E. (2011). From Superamphiphobic to Amphiphilic Polymeric Surfaces with Ordered Hierarchical Roughness Fabricated with Colloidal Lithography and Plasma Nanotexturing. *Langmuir* 27, 3960–3969.
- Emashova, N. A., Kudryashov, V. E., Sirjuba, T. A., Balandina, A. V., Bratschev, A. V., Sklyar, V. I. and Kalyuzhni, S. V. (2016). Quo Vadis, Worldwide Nanoindustry?: *Nanotechnol. Russ.* 11.3–4, 117–127.
- Gao, S., Zhang, Y., Xing, H. and Li, H. (2020). Controlled reduction synthesis of yolk-shell magnetic@void@C for electromagnetic wave absorption. *Chem. Eng. J.* 387, 124149.
- Gemici, Z., Shimomura, H., Cohen, R. E. and Rubner, M. F. (2008). Hydrothermal Treatment of Nanoparticle Thin Films for Enhanced Mechanical Durability. *Langmuir* 24, 2168–2177.
- Gijs, M. A. M., Lacharme, F. and Lehmann, U. (2010). Microfluidic Applications of Magnetic Particles for Biological Analysis and Catalysis. *Chem. Rev.* 110, 1518–1563.
- Hamdy, A. S. (2006). Advanced nano-particles anti-corrosion ceria based sol gel coatings for aluminum alloys. *Mater. Lett.* 60, 2633–2637.

- Haneda, K. and Morrish, A. H. (1977). Magnetite to maghemite transformation in ultrafine particles. *J. Phys. (Paris)* 4.38, 321–323.
- Hanesh, M. (2009). Raman spectroscopy of iron oxides and (oxy)hydroxides at low laser power and possible applications in environmental magnetic studies. *Geophys. J. Int.* 177, 941–948.
- Harra, J., Kujanpää, S., Haapanen, J., Juuti, P. and Mäkelä, J. M. (2017). Aerosol analysis of residual and nanoparticle fractions from spray pyrolysis of poorly volatile precursors. *AIChE J.* 63.3, 881–892.
- Heine, M. C. and Pratsinis, S. E. (2005). Droplet and Particle Dynamics during Flame Spray Synthesis of Nanoparticles. *Ind. Eng. Chem. Res.* 44, 6222–6232.
- Hsu, M.-C., Alfadhel, A., Forouzandeh, F. and Borkholder, D. A. (2018). Biocompatible magnetic nanocomposite microcapsules as microfluidic one-way diffusion blocking valves with ultra-low opening pressure. *Mater. Des.* 150, 86–93.
- Jiang, D., Fan, P., Gong, D., Long, J., Zhang, H. and Zhong, M. (2016). High-temperature imprinting and superhydrophobicity of micro/nano surface structures on metals using molds fabricated by ultrafast laser ablation. *J. Mater. Process. Tech.* 236, 56–63.
- Jönkkäri, I., Matti, I. and Syrjälä, S. (2015). Sedimentation stability and rheological properties of ionic liquid-based bidisperse magnetorheological fluids. *J. Intell. Mater. Syst. Struct.* 26, 2256–2265.
- Jönkkäri, I., Sorvali, M., Huhtinen, H., Sarlin, E., Salminen, T., Haapanen, J., Mäkelä, J. M. and Vuorinen, J. (2017). Characterization of bidisperse magnetorheological fluids utilizing maghemite ( $\gamma\text{-Fe}_2\text{O}_3$ ) nanoparticles synthesized by flame spray pyrolysis. *Smart Materials and Structures* 26, 095004. DOI: 10.1088/1361-665X/aa7f7d.
- Jørgensen, J.-E., Mosegaard, L., Thomsen, L. E., Jensen, T. R. and Hanson, J. C. (2007). Formation of  $\gamma\text{-Fe}_2\text{O}_3$  nanoparticles and vacancy ordering: an in situ X-ray powder diffraction study. *J. Solid State Chem.* 180.1, 180–185.
- Jossen, R., Pratsinis, S. E., Stark, W. J. and Mädler, L. (2005). Criteria for Flame-Spray Synthesis of Hollow, Shell-Like, or Inhomogeneous Oxides. *J. Am. Ceram. Soc.* 88.6, 1388–1393.
- Jossen, R., Stark, W. J., Mädler, L. and Pratsinis, S. E. (2003). Effect of Precursor and Solvent on Particle Homogeneity and Morphology during Spray Flame Synthesis of Nanoparticles. *Chemie Ingenieur Technik* 75, 1129–1130.

- Juuti, P., Nikka, M., Gunell, M., Eerola, E., Saarinen, J. J., Omori, Y., Seto, T. and Mäkelä, J. M. (2019). Fabrication of Fiber Filters with Antibacterial Properties for VOC and Particle Removal. *Aerosol Air Qual. Res.* 19, 1892–1899.
- Kammler, H. K., Mädler, L. and Pratsinis, S. E. (2001). Flame Synthesis of Nanoparticles. *Chem. Eng. Technol.* 24.6, 583–596.
- Katz, M. J., Riha, S. C., Cheong, N. C., Martinson, A. B. F., Farha, O. K. and Hupp, J. T. (2012). Toward solar fuels: Water splitting with sunlight and “rust”? *Coordination Chem. Rev.* 256, 2521–2529.
- Keskinen, H., Aromaa, M., Heine, M.-C. and Mäkelä, J. M. (2008). Size and velocity measurements in sprays and particle producing flame sprays. *Atomization Sprays* 18, 1–26.
- Khan, U. S., Amanullah, Manan, A., Khan, N., Mahmood, A. and Rahim, A. (2015). Transformation mechanism of magnetite nanoparticles. *Mater. Sci.-Poland* 33.2, 278–285.
- Kilpi, L., Ylivaara, O. M. E., Vaajoki, A., Malm, J., Sintonen, S., Tuominen, M., Puurunen, R. L. and Ronkainen, H. (2016). Microscratch testing method for systematic evaluation of the adhesion of atomic layer deposited thin films on silicon. *J. Vac. Sci. Technol. A* 34, 01A124.
- Kotsyubynsky, V., Ostafychuk, B., Moklyak, V. and Hrubciak, A. (2015). Synthesis, Characterization and Electrochemical Properties of Mesoporous Maghemite  $\gamma$ - $\text{Fe}_2\text{O}_3$ . *Sol. St. Phen.* 230, 120–126.
- Lefebvre, A. H. and McDonell, V. G. (2017). *Atomization and Sprays*. 2nd ed. Boca Raton, Florida, USA: CRC Press. 301 pp.
- Leskelä, M. and Ritala, M. (2003). Atomic Layer Deposition Chemistry: Recent Developments and Future Challenges. *Angew. Chem. Int. Ed.* 42, 5548–5554.
- Li, H. and Yu, S. (2016). Facile fabrication of micro-nano-rod structures for inducing a superamphiphobic property on steel surface. *Appl. Phys. A* 122.30.
- Li, S., Hu, S., Xu, K., Jiang, W., Hu, J. and Liu, J. (2017). Excellent visible-light photocatalytic activity of p-type  $\text{Ag}_2\text{O}$  coated n-type  $\text{Fe}_2\text{O}_3$  microspheres. *Mater. Lett.* 188, 268–371.
- Li, S., Ren, Y., Biswas, P. and Tse, S. D. (2016). Flame aerosol synthesis of nanostructured materials and functional devices: Processing, modeling, and diagnostics. *Prog. Energ. Combust.* 55, 1–59.

- Lim, B. S., Rahtu, A. and Gordon, R. G. (2003). Atomic layer deposition of transition metals. *Nat. Mater.* 2, 749–754.
- Liu, C., Camacho, J. and Wang, H. (2018). Phase Equilibrium of TiO<sub>2</sub> Nanocrystals in Flame-Assisted Chemical Vapor Deposition. *Chem. Phys. Chem.* 19, 180–186.
- Liu, T. and Kim, C.-J. (2014). Turning a surface superrepellent even to completely wetting liquids. *Science* 346.6213, 1096–1100.
- Mädler, L., Kammler, H. K., Mueller, R. and Pratsinis, S. E. (2002). Controlled synthesis of nanostructured particles by flame spray pyrolysis. *J. Aerosol. Sci.* 33, 369–389.
- Mädler, L. and Pratsinis, S. E. (2002). Bismuth Oxide Nanoparticles by Flame Spray Pyrolysis. *J. Am. Ceram. Soc.* 85.7, 1713–1718.
- Mädler, L., Stark, W. J. and Pratsinis, S. E. (2002). Flame-made ceria nanoparticles. *J. Mater. Res.* 17.6, 1356–1362.
- Makhlouf, A. S. H. and Tiginyanu, I. (2011). *Nanocoatings and ultra-thin films: Technologies and applications*. Philadelphia, USA: Woodhead Publishing. 448 pp.
- Manuputty, M. Y., Dreyer, J. A. H., Sheng, Y., Bringley, E. J., Botero, M. L., Akroyd, J. and Kraft, M. (2019). Polymorphism of nanocrystalline TiO<sub>2</sub> prepared in a stagnation flame: formation of the TiO<sub>2</sub>-II phase. *Chem. Sci.* 10, 1342–1350.
- Marmur, A. and Bittoun, E. (2009). When Wenzel and Cassie Are Right: Reconciling Local and Global Considerations. *Langmuir* 25, 1277–1281.
- Meierhofer, F., Li, H., Gockeln, M., Kun, R., Grieb, T., Rosenauer, A., Fritsching, U., Kiefer, J., Birkenstock, J., Mädler, L. and Pokhrel, S. (2017). Screening Precursor-Solvent Combinations for Li<sub>4</sub>Ti<sub>5</sub>O<sub>12</sub> Energy Storage Material Using Flame Spray Pyrolysis. *ACS Appl. Mater. Interfaces* 9, 37760–37777.
- Miikkulainen, V., Leskelä, M., Ritala, M. and Puurunen, R. (2013). Crystallinity of inorganic films grown by atomic layer deposition: overview and general trends. *J. Appl. Phys.* 113, 021301.
- Mou, F., Guan, J.-G., Shi, W., Sun, Z. and Wang, S. (2010). Oriented Contraction: A Facile Nonequilibrium Heat-Treatment Approach for Fabrication of Maghemite Fiber-in-Tube and Tube-in-Tube Nanostructures. *Langmuir* 26.19, 15580–15585.
- Mueller, R., Mädler, L. and Pratsinis, S. E. (2003). Nanoparticle synthesis at high production rates by flame spray pyrolysis. *Chem. Eng. Sci.* 58, 1969–1976.

- Muruganandham, M., Amutha, R., Sathish, M., Singh, T. S., Suri, R. P. S. and Silanpää, M. (2011). Facile Fabrication of Hierarchical  $\alpha$ -Fe<sub>2</sub>O<sub>3</sub>: Self-Assembly and Its Magnetic and Electrochemical Properties. *J. Phys. Chem. C* 115, 18164–18173.
- Ngatu, G. T. and Wereley, N. M. (2007). Viscometric and sedimentation characterization of bidisperse magnetorheological fluids. *Trans. Magn.* 43, 2474–2476.
- Nosrati, H., Salehiabar, M., Fridoni, M., Abdollahifar, M.-A., Manjili, H. K., Davaran, S. and Danafar, H. (2019). New insight about biocompatibility and biodegradability of iron oxide magnetic nanoparticles: stereological and in vivo MRI monitor. *Sci. Rep.* 9, 7173.
- Ong, Y. S., Bañobre-López, M., Lima, S. A. C. and Reis, S. (2020). A multifunctional nanomedicine platform for co-delivery of methotrexate and mild hyperthermia towards breast cancer therapy. *Mat. Sci. Eng. C-Mater.* 116, 11255.
- Pant, P., Naik, B. D. and Ghosh, N. N. (2009). Synthesis of  $\alpha$ -Fe<sub>2</sub>O<sub>3</sub> nano powder by simple chemical method. *Mater. Technol.* 24.4, 213–216.
- Parvate, S., Dixit, P. and Chattopadhyay, S. (2020). Superhydrophobic Surfaces: Insights from Theory and Experiment. *J. Phys. Chem. B* 124.8, 1323–1360.
- Pecharromás, C., González-Carreño, T. and Iglesias, J. E. (1995). The infrared dielectric properties of maghemite,  $\gamma$ -Fe<sub>2</sub>O<sub>3</sub> from reflectance measurement on pressed powders. *Phys. Chem. Miner.* 22.1, 21–29.
- Pitkänen, A., Mäkelä, J. M., Nurminen, M., Oksanen, A., Janka, K., Keskinen, J., Keskinen, H., Liimatainen, J. K., Hellstén, S. and Määttä, T. (2005). Numerical study of silica particle formation in turbulent H<sub>2</sub>/O<sub>2</sub> flame. *IFRF Combust. J.* 200509.
- Puurunen, R. (2005). A Short History of Atomic Layer Deposition: Tuomo Suntola's Atomic Layer Epitaxy. *Chem. Vap. Deposition* 20, 1–13.
- Roco, M. C. (2011). The long view of nanotechnology development: the National Nanotechnology Initiative at 10 years. *J. Nanopart. Res.* 13, 427–445.
- Rohilla, J. and Ingole, P. P. (2021). Optimizing hematite nanostructures for electrochemical and photoelectrochemical water splitting applications. *Current Opinion in Green and Sustainable Chemistry* 29, 100455.
- Rosebrock, C. D., Riefler, N., Wriedt, T. and Mädler, L. (2013). Disruptive Burning of Precursor/Solvent Droplets in Flame-Spray Synthesis of Nanoparticles. *AIChE J.* 59.12, 4553–4566.

- Rosebrock, C. D., Wriedt, T. and Mädler, L. (2016). The Role of Microexplosions in Flame Spray Synthesis for Homogeneous Nanopowders from Low-Cost Metal Precursors. *AIChE J.* 62.2, 381–391.
- Rudyak, V. Y. and Krasnolutsii, S. L. (2014). Dependence of the viscosity of nanofluids on nanoparticle size and material. *Phys. Lett. A* 378, 1845–1849.
- Sakurai, S., Namai, A., Hashimoto, K. and Ohkoshi, S. (2009). First Observation of Phase Transformation of All Four  $\text{Fe}_2\text{O}_3$  Phases ( $\gamma \rightarrow \epsilon \rightarrow \beta \rightarrow \alpha$ ). *J. Am. Chem. Soc.* 131, 18299–18303.
- Schulz, C., Dreier, T., Fikri, M. and Wiggers, H. (2019). Gas-phase synthesis of functional nanomaterials: Challenges to kinetics, diagnostics, and process development. *P. Combust. Inst.* 37, 83–108.
- Seddiki, O., Harnagea, C., Levesque, L., Mantovani, D. and Rosei, F. (2014). Evidence of antibacterial activity on titanium surfaces through nanotextures. *Appl. Surf. Sci.* 308, 275–284.
- Shi, H.-G., Li, S.-L., Cheng, J.-B., Zhao, H.-B. and Wang, Y.-Z. (2021). Multifunctional Photothermal Conversion Nanocoatings Toward Highly Efficient and Safe High-Viscosity Oil Cleanup Absorption. *ACS Appl. Mater. Interfaces* 13.10, 11948–11957.
- Shi, T., Kong, J., Wang, X. and Li, X. (2016). Preparation of multifunctional Al-Mg alloy surface with hierarchical micro/nanostructures by selective chemical etching processes. *Appl. Surf. Sci.* 389, 335–343.
- Solano, E., Frontera, C., Puig, T., Obradors, X., Ricart, S. and Ros, J. (2014). Neutron and X-ray diffraction study of ferrite nanocrystals obtained by microwave-assisted growth. A structural comparison with the thermal synthetic route. *J. Appl. Crystallogr.* 47, 414–420.
- Sorvali, M.**, Honkanen, M., Hyvärinen, L., Kuisma, R., Larjo, J. and Mäkelä, J. M. (2021). Crystallographic phase formation of iron oxide particles produced from iron nitrate by liquid flame spray with a dual oxygen flow. *International Journal of Ceramic Engineering and Science* 3.5, 227–236. DOI: 10.1002/ces2.10102.
- Sorvali, M.**, Nikka, M., Juuti, P., Honkanen, M., Salminen, T., Hyvärinen, L. and Mäkelä, J. M. (2019). Controlling the phase of iron oxide nanoparticles fabricated from iron(III) nitrate by liquid flame spray. *International Journal of Ceramic Engineering and Science* 1.4, 194–205. DOI: 10.1002/ces2.10025.

- Sorvali, M., Vuori, L., Pudas, M., Haapanen, J., Mahlberg, R., Ronkainen, H., Honkanen, M., Valden, M. and Mäkelä, J. M. (2018). Fabrication of ultrathin multilayered superomniphobic nanocoatings by liquid flame spray, atomic layer deposition, and silanization. *Nanotechnology* 29, 185708. DOI: 10.1088/1361-6528/aaaffc.
- Stodt, M. F. B., Kiefer, J. and Fritsching, U. (2019). Ethanol droplet formation, dynamics and combustion mode in the flame of the SpraySyn-nozzle. *Exp. Fluids* 60.125.
- Strobel, R. and Pratsinis, S. E. (2009). Direct Synthesis of maghemite, magnetite and wustite nanoparticles by flame spray pyrolysis. *Adv. Powder Technol.* 20, 190–194.
- (2011). Effect of solvent composition on oxide morphology during flame spray pyrolysis of metal nitrates. *Phys. Chem. Chem. Phys.* 13, 9246–9252.
- Sun, T., Feng, L., Gao, X. and Jiang, L. (2005). Bioinspired Surfaces with Special Wettability. *Acc. Chem. Res.* 38, 644–652.
- Tamirat, A. G., Rick, J., Dubale, A. A., Su, W.-N. and Hwang, B.-J. (2016). Using hematite for photoelectrochemical water splitting: a review of current progress and challenges. *Nanoscale Horiz.* 1, 243–267.
- Teja, A. S. and Koh, P.-Y. (2009). Synthesis, properties, and applications of magnetic iron oxide particles. *Prog. Cryst. Growth Ch.* 55, 22–45.
- Teoh, W. Y., Amal, R. and Mädler, L. (2010). Flame spray pyrolysis: An enabling technology for nanoparticles design and fabrication. *Nanoscale* 2, 1324–1347.
- Tikkanen, J., Gross, K. A., Berndt, C. C., Pitkänen, V., Keskinen, J., Raghu, S., Rajala, M. and Karthikeyan, J. (1997). Characteristics of the liquid flame spray process. *Surf. Coat. Technol.* 90, 210–216.
- Usov, N. A. (2019). Iron Oxide Nanoparticles for Magnetic Hyperthermia. *SPIN* 9.2, 1940001.
- Vicente, J. de, Klingenberg, D. J. and Hidalgo-Alvarez, R. (2011). Magnetorheological fluids: a review. *Soft Matter* 7, 3701–3710.
- Vuori, L., Hannula, M., Lahtonen, K., Jussila, P., Ali-Löytty, H., Hirsimäki, M., Pärna, R., Nömmiste, E. and Valden, M. (2014). Controlling the synergetic effects in (3-aminopropyl) trimethoxysilane and (3-mercaptopropyl) trimethoxysilane coadsorption on stainless steel surfaces. *Appl. Surf. Sci.* 317, 856–866.
- Vuori, L., Leppiniemi, J., Hannula, M., Lahtonen, K., Hirsimäki, M., Nömmiste, E., Costelle, L., Hytönen, V. P. and Valden, M. (2014). Biofunctional hybrid ma-



- terials: bimolecular organosilane monolayers on FeCr alloys. *Nanotechnology* 25, 435603.
- Wang, X., Liao, Y., Zhang, D., Wen, T. and Zhong, Z. (2018). A review of Fe<sub>3</sub>O<sub>4</sub> thin films: Synthesis, modification and applications. *J. Mater. Sci. Technol.* 34, 1259–1272.
- Wei, Q., Sun, J., Song, P., Yang, Z. and Wang, Q. (2020). Metal-organic frameworks-derived porous  $\alpha$ -Fe<sub>2</sub>O<sub>3</sub> spindles decorated with Au nanoparticles for enhanced triethylamine gas-sensing performance. *J. Alloy. Compd.* 831, 154788.
- Wenzel, R. N. (1936). Resistance of solid surfaces to wetting by water. *Ind. Eng. Chem.* 28, 988–994.
- Wereley, N. M., Chaudhuri, A., Yoo, J. H., John, S., Kotha, S., Suggs, A., Radhakrishnan, R., Love, B. J. and Sudarshan, T. S. (2006). Bidisperse magnetorheological fluids using Fe particles at nanometer and micron scale. *J. Intell. Mater. Syst. Struct.* 17, 393–401.
- Wu, W., He, Q. and Jiang, C. (2008). Magnetic iron oxide nanoparticles: synthesis and surface functionalization strategies. *Nanoscale Res. Lett.* 3, 397–415.
- Wu, W., Wu, Z., Yu, T., Jiang, C. and Kim, W.-S. (2015). Recent progress on magnetic iron oxide nanoparticles: synthesis, surface functional strategies and biomedical applications. *Sci. Technol. Adv. Mater.* 16, 023501.
- Yatsenko, D. A., Pakharukova, V. P., Tsybulya, S. V., Matvienko, A. A. and Sidel'nikov, A. A. (2012). Phase composition and structure of nanocrystalline products of solid-phase oxidative thermolysis of iron oxalate dihydrate. *J. Struct. Chem.* 53.3, 548–556.
- Zeng, F., Qin, Z., Chen, Y. and Shan, X. (2021). Constructing polyaniline nanowire arrays as efficient traps on graphene sheets to promote compound synergetic effect in the assembled coating for multifunctional protective cotton fabrics. *Chem. Eng. J.* 426, 130819.
- Zhang, D., Xu, Y. and Feng, G. (2015). Comparing sintering and atomic layer deposition as methods to mechanically reinforce nanocolloidal crystals. *J. Mater. Res.* 30.20, 3717–3727.
- Zhang, D., Zhang, L., Lee, D., Cheng, Z. and Feng, G. (2015). Reinforcing nanocolloidal crystals by tuning interparticle bonding via atomic layer deposition. *Acta Mater.* 95, 216–223.

- Zhang, X., Wang, M., Wang, Y., Zhang, C., Zhang, Z., Wang, F. and Xu, J. (2014). Nanocoating of magnetic cores with sulfonic acid functionalized shells for the catalytic dehydration of fructose to 5-hydroxymethylfurfural. *Chinese J. Catal.* 35.5, 703–708.

# PUBLICATION

I

**Controlling the phase of iron oxide nanoparticles fabricated from iron(III) nitrate by liquid flame spray**

**Sorvali, M., Nikka, M., Juuti, P., Honkanen, M., Salminen, T., Hyvärinen, L. and Mäkelä, J. M.**

*International Journal of Ceramic Engineering and Science* 1.4 (2019), 194–205

DOI: 10.1002/ces2.10025

**Publication reprinted with the permission of the copyright holders**



## ORIGINAL ARTICLE

# Controlling the phase of iron oxide nanoparticles fabricated from iron(III) nitrate by liquid flame spray

Miika Sorvali<sup>1</sup> | Markus Nikka<sup>1</sup> | Paxton Juuti<sup>1</sup> | Mari Honkanen<sup>2</sup> |  
Turkka Salminen<sup>2</sup> | Leo Hyvärinen<sup>3</sup> | Jyrki M. Mäkelä<sup>1</sup>

<sup>1</sup>Aerosol Physics Laboratory, Physics Unit, Faculty of Engineering and Natural Sciences, Tampere University, Tampere, Finland

<sup>2</sup>Tampere Microscopy Center, Tampere University, Tampere, Finland

<sup>3</sup>Engineering Materials Science, Materials Science and Environmental Engineering Unit, Faculty of Engineering and Natural Sciences, Tampere University, Tampere, Finland

## Correspondence

Miika Sorvali, Aerosol Physics Laboratory, Physics Unit, Faculty of Engineering and Natural Sciences, Tampere University, P.O. Box 692, FI-33014 Tampere, Finland.  
Email: miika.sorvali@tuni.fi

## Funding information

Tampere University of Technology Graduate School

## Abstract

Iron oxide nanoparticles were synthesized in a liquid flame spray process from iron(III) nitrate. The choice of chemicals and all other process parameters affects the crystallographic phase composition and the quality of the material. Adjustment of the solvent composition and the gas flow rates was used to control the phase composition of the produced particles. All samples consisted of pure maghemite ( $\gamma\text{-Fe}_2\text{O}_3$ ) or a mixture of maghemite and hematite ( $\alpha\text{-Fe}_2\text{O}_3$ ). When using pure alcohols as solvents, the maghemite/hematite phase ratio could be adjusted by changing the equivalence ratio that describes the oxidation conditions in the flame zone. A large residual particle mode formed in the size range of ~20–700 nm along with a dominant very fine particle mode (2–8 nm). Both phases seemed to contain large particles. A partial substitution of methanol with carboxylic acids turned the hematite phase into maghemite completely, even though some of particles were possibly not fully crystallized. Residual particles were still present, but their size and number could be decreased by raising the heat of combustion of the precursor solution. 30 vol-% substitution of methanol with 2-ethylhexanoic acid was adequate to mostly erase the large particles.

## KEYWORDS

iron/iron compounds, liquid flame spray, nanoparticles, synthesis

## 1 | INTRODUCTION

Iron oxide particles generally occur in one of the four main crystallographic phases depending on the Fe oxidation state: magnetite ( $\text{Fe}_3\text{O}_4$ ), maghemite ( $\gamma\text{-Fe}_2\text{O}_3$ ), hematite ( $\alpha\text{-Fe}_2\text{O}_3$ ), or wüstite ( $\text{FeO}$ ), of which the first three are technologically the most relevant.<sup>1,2</sup> The majority of the applicable potential of magnetite and maghemite lies with their exceptional magnetic properties, whereas hematite possesses, among other things, promising catalytic properties. Applications utilizing magnetic particles include magnetic resonance imaging,<sup>3,4</sup> microfluidic systems,<sup>5,6</sup> magnetorheological fluids,<sup>7,8</sup> and

biomedicine,<sup>9,10</sup> while hematite has been used, for example, for lithium-ion batteries,<sup>11,12</sup> gas sensors,<sup>13</sup> and catalysis.<sup>14,15</sup>

Magnetite is magnetically the strongest phase, but also maghemite possesses good magnetic properties and is more stable. In addition to the crystallographic phase, the particle size has a strong influence on both magnetic and catalytic properties. The unique magnetic properties stem from superparamagnetism that emerges in the nanoscale, when an adequately small particle size is achieved. As the particle diameter reaches a critical limit of around 20 nm for magnetite,<sup>16,17</sup> only one magnetic domain remains in each particle. A strong magnetization can then be rapidly switched

This is an open access article under the terms of the Creative Commons Attribution License, which permits use, distribution and reproduction in any medium, provided the original work is properly cited.

© 2019 The Authors. *International Journal of Ceramic Engineering & Science* published by Wiley Periodicals, Inc. on behalf of American Ceramic Society

on and off with an external magnetic field. This fast magnetization switch is utilized, for instance, in magnetorheological fluids.<sup>7,8</sup> For hematite, the small size of the particles mainly promotes their catalytic activity through an increase in surface area-to-volume ratio. Also, many other properties, such as particle shape, conductivity, and charge injection efficiency, affect the catalytic performance of different catalysts.<sup>14</sup> Therefore, it is important to discover more efficient, economic and environmental friendly ways of producing ultrafine iron oxide nanoparticles of different phases.

Iron oxide powders have been produced with a myriad of fabrication methods and they often consist of a mixture of phases. Chemical methods, such as co-precipitation<sup>18</sup> and hydrothermal synthesis,<sup>19</sup> generally provide good control over the particle properties but usually a noncontinuous, batch-type process, which complicates fast and large-scale production. Gaseous precursors have been used in chemical vapor synthesis of controlled oxidation of iron nanoparticles.<sup>20</sup> Physical methods like spray pyrolysis and especially flame synthesis<sup>21–23</sup> enable much higher production rates, but usually at the expense of process control. As large volumes are often required in industry, the physical methods provide a better basis for upscaling and often an adequate control over the end product. With high volumes, also the price of the precursor becomes extremely important. Therefore, fast and upscalable fabrication methods that can utilize inexpensive liquid precursors are economically excellent alternatives. One flame synthesis method that checks many of these boxes and can be used for producing metal and metal oxide nanoparticles is liquid flame spray (LFS).<sup>24,25</sup>

Iron nitrate is an inexpensive and abundant precursor that easily dissolves in cheap and common solvents, which makes it an extremely good alternative for large-scale production.<sup>26</sup> However, as for most nitrate precursors, effective and complete combustion is quite difficult to achieve, which often leads to a residual mode consisting of large particles. Strobel and Pratsinis<sup>21</sup> produced maghemite, magnetite, and wüstite by Flame Spray Pyrolysis (FSP). The latter two were only produced in an enclosed chamber by restricting the amount of oxygen in the flame zone, and an open flame only led to maghemite phase. However, hematite has proven to be challenging to produce with flame synthesis methods. Buyukhatipoglu and Clyne<sup>27</sup> were able to produce a mixture of maghemite and hematite in a flame synthesis by using an argon stream to deliver iron pentacarbonyl vapor into the flame zone. Finding new solutions to push the complete phase composition toward a single phase would be beneficial.

In this study, we investigated how the phase composition of LFS-made iron oxide nanoparticles can be controlled by adjusting the gas flows and changing the solvent composition. A lot of literature is available on how different parameters, like dispersing gas flow, precursor concentration and

feed rate, and the solvent properties, affect the synthesis conditions.<sup>28–32</sup> Due to the plethora of parameters affecting the end product, we focused specifically on iron nitrate as the precursor. We found no similar earlier studies that aim to control the hematite/maghemite ratio of flame-synthesized iron oxide particles. Better tunability of the phase increases the versatility of the flame process in utilizing cost-effective nitrate-based precursors. Because the detailed physical and chemical processes happening in the flame are still relatively unclear, studies like these can help achieve understanding of the fundamental processes.

The chemistry of the precursor solution and the flame conditions can be tuned to achieve a more oxidizing or a more reducing environment for particle production, leading to varying phase compositions.<sup>21,22</sup> One measure that takes into consideration the interplay between many different parameters, and has been used in earlier studies to evaluate the oxidation conditions during FSP synthesis, is the so-called equivalence ratio.<sup>21,33,34</sup> It considers the amount of oxygen that is necessary for burning all the fuel present in the process (stoichiometric amounts) relative to the actual amount of oxygen present and is defined as:

$$\Phi = \frac{\left(\frac{n_{\text{fuel}}}{n_{\text{oxygen}}}\right)_{\text{actual}}}{\left(\frac{n_{\text{fuel}}}{n_{\text{oxygen}}}\right)_{\text{stoich}}}, \quad (1)$$

where  $n_{\text{fuel}}$  is the combined amount of substance from the hydrogen flow and the solvent of the precursor solution per unit time, and  $n_{\text{oxygen}}$  is the amount of substance of oxygen molecules coming from the oxygen flow per unit time.

## 2 | EXPERIMENTAL

### 2.1 | Materials

The precursor used for all samples was iron(III) nitrate nonahydrate ( $\text{Fe}(\text{NO}_3)_3 \cdot 9\text{H}_2\text{O}$ , 98+% (metals basis), Alfa Aesar). The solvents used were methanol (MeOH) (EMSURE® ACS, Reag. Ph Eur, Merck), ethanol (EtOH) (99.5+%, Altia Oyj), isopropanol (IPA) (99.8+%, VWR International), 2-ethylhexanoic acid (EHA) (99%, Acros Organics), butanoic acid (ButA) (99%, Merck), and propanoic acid (PropA) (99.5+%, Honeywell Fluka).

Different alcohols were chosen to test the effect of combustion enthalpy on the final product, as the solvents are chemically fairly similar. The three solvents have notable differences in their heat of combustion (HOC): 726 kJ/mol for MeOH, 1367 kJ/mol for EtOH, and 2005 kJ/mol for IPA. If we consider the HOC per unit volume, the percentual differences between the alcohols narrow down: 17.92 kJ/mL for MeOH, 23.45 kJ/mL for EtOH, and 26.2 kJ/mL for IPA, but still clearly differ from each other.

Sample	Solvent composition	H <sub>2</sub> flow rate (L/min)	O <sub>2</sub> flow rate (L/min)	Liquid feed rate (mL/min)	Φ
I1	IPA	60	20	4	1.76
I2	IPA	60	20	2	1.63
I3	IPA	30	30	2	0.39
I4	IPA	20	35	2	0.36
I5	IPA	20	35	1	0.32
E1	EtOH	60	20	4	1.73
E2	EtOH	60	20	2	1.61
E3	EtOH	30	30	2	0.58
E4	EtOH	20	35	2	0.35
E5	EtOH	20	35	1	0.32
M1	MeOH	33	15	2	1.21
M2	MeOH	20	35	2	0.33
ME1	MeOH + EHA (95/5 vol-%)	20	35	2	0.33
ME2	MeOH + EHA (85/15 vol-%)	20	35	2	0.34
ME3	MeOH + EHA (70/30 vol-%)	20	35	2	0.34
ME4	MeOH + EHA (50/50 vol-%)	20	35	2	0.35
MB	MeOH + ButA (50/50 vol-%)	20	35	2	0.34
MP	MeOH + PropA (50/50 vol-%)	20	35	2	0.34

**TABLE 1** The parameters of different samples. Oxygen was used as the atomizing gas in all cases

## 2.2 | Nanoparticle synthesis

Iron oxide powders were synthesized by LFS, described in more detail elsewhere.<sup>28,35</sup> In short, an oxygen or a hydrogen gas flow is used to atomize a liquid precursor solution feed into a turbulent H<sub>2</sub>/O<sub>2</sub> flame, where the droplets consequently burn. In contrast to the majority of earlier LFS studies describing nanoparticle synthesis, we used the oxygen flow for atomization in this study, as oxygen seemed to be more effective. The two gas flows emerge from two concentric annular orifices, so they can be easily switched, if desired. The H<sub>2</sub> and O<sub>2</sub> gas flow rates were varied between 20-60 L/minutes and 12-35 L/minutes, respectively. The precursor concentration was kept constant for all cases, so that all precursor solutions contained 40 mg/mL of Fe atoms, which translates to a molar concentration of 0.72 mol/L. Also, the liquid feed rate was mostly kept constant at 2 mL/minutes, which results in Fe atom flow of 80 mg/minutes through the flame, but a few exceptions were chosen in order to see if the liquid feed rate has a profound effect on the phase ratio. All different samples are presented in Table 1 along with their equivalence ratios.

The powder samples were collected with an electrostatic precipitator that consisted of two nearly parallel metal plates, one of which had thin metal wires attached to it. The metal wires worked as corona needles when a high voltage (20-35 kV) was applied to the plate. The other plate was

grounded, creating a strong electric field between them. The flame was directed between the plates, so that the nanoparticle flux moved through the electric field. The particles experienced electrical charging from the corona discharges present around the tip of the metal wires and a consequent deposition onto the grounded plate. The deposited particles were carefully scraped off the metal plate and collected in a container for analysis.

## 2.3 | Characterization and sample preparation

The crystal structure of the powders was characterized with X-ray powder diffraction (XRD) (Panalytical Empyrean, monochromatized CuK<sub>α</sub> radiation 15° < 2θ < 70°). The recorded XRD patterns were analyzed by Rietveld refinement, using BRASS 2 program.<sup>36</sup> The structure models used for the refinement were acquired from American Mineralogist Crystal Structure Database (AMCSD) with the codes 0020585 for maghemite (space group Fd-3m) and 0000143 for hematite (space group R-3c). Since several models with different space groups were available for maghemite, the model used was chosen based on which gave the best fit for pure maghemite samples. Further structural information was obtained with a Raman microscope (Renishaw inVia™ Qontor®) that enabled simultaneous optical microscopy and the recording of Raman spectra from specifically chosen

locations. The wavelength used for excitation was 532 nm. The Raman samples were prepared by attaching a piece of double-sided tape on a microscope slide and spreading a small amount of a collected powder onto it. The powder samples were thick enough to eliminate any signal emanating from the substrate. With iron oxide nanoparticles, one must be very careful with the laser power, because magnetite and maghemite are easily turned into other phases, if the intensity of the laser beam is too high.<sup>37,38</sup> Therefore, a very low laser power (~0.3 mW) was chosen to prevent phase changes during the measurements.

The sizes and shapes of the particles were analyzed with a transmission electron microscope (TEM) (JEOL JEM-F200). The TEM samples were prepared by dispersing powders in ethanol, followed by 15-minutes ultrasonic bath to break large agglomerates, and finally dipping a TEM grid with a carbon film in the dispersion. As the ethanol evaporated, the particles attached to the TEM grid sufficiently well. TEM imaging is a reliable way to analyze the precise size of the primary particles, but a TEM sample is always a very small representation of the whole powder, so we used the XRD results to interpret the whole picture. Due to various error sources and possible polydispersity, the XRD results cannot be directly translated into the actual size of the particles, but rather to indicate the presence of large particles, when combined with TEM studies. The average crystallite sizes can be obtained from Rietveld analyses.

### 3 | RESULTS AND DISCUSSION

#### 3.1 | Pure alcohols as solvents

XRD works well in distinguishing hematite from maghemite and magnetite, since there are several significant peaks without overlap. Two of these distinct reflections are at  $2\theta$  angles of a little above  $30^\circ$  for maghemite/magnetite and  $33^\circ$  for hematite. Figure 1 shows these two peaks for three samples produced with EtOH as the solvent with varying gas flows. All of the patterns were scaled based on the  $30^\circ$  peak to demonstrate the change in the ratio between the peak areas as the ratio of the gas flows shifts.

When there is more oxygen available in the flame zone, a larger portion of the produced particles formed in the more oxidized hematite phase. Li et al<sup>16</sup> has stated that flame-made iron oxide generally crystallizes as maghemite, and we did not come across any studies where hematite powder would have been fabricated directly in liquid-fed FSP.

We used Rietveld refinement to quantify the weight percentages of each phase in each sample from the XRD results. The Rietveld plots for all samples and some chosen parameters are presented in Figures S1-S6 and Table S1. As the hematite phase was difficult to fully refine in samples with low hematite fractions, there is more uncertainty for these. Because the following Raman results indicated that the

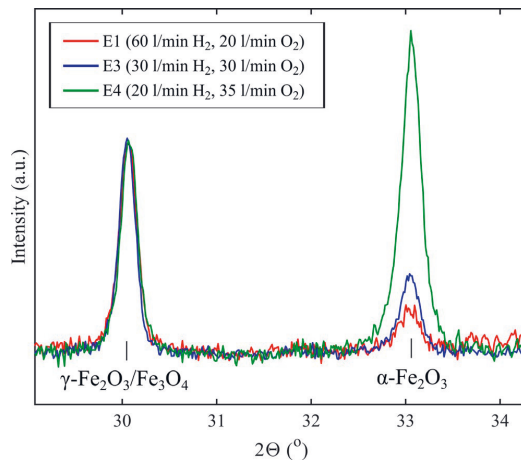


**FIGURE 1** Patterns of two XRD reflections for samples produced with ethanol as the solvent and varying gas flows. All intensities were normalized based on the  $30^\circ$  peak

samples consisted of only maghemite and hematite, we will not be mentioning magnetite from now on. By trying to figure out the correlation of different parameters to the phase composition, it turned out that the equivalence ratio ( $\Phi$ ) could be used to describe the phase behavior quite well. The iron nitrate precursor is not considered in the calculations, since it is assumed to go through an endothermic decomposition reaction.<sup>39</sup> Because we used an atmospheric synthesis process, the theoretical amount of oxygen is most likely not the actual amount present due to possible oxygen diffusion from the surrounding air. Figure 2 depicts the calculated maghemite fraction as a function of equivalence ratio.

All of the samples with an alcohol as the solvent fall quite nicely on a curve, but there seems to be some effect, possibly originating from the differing chemistry of the solvents, that places most IPA samples above the EtOH samples. The effect of chain branching and carbon chain length could be studied by experimenting with different alcohols. In general, the HOC values do not seem to have a significant effect on the phase behavior. It looks like the maghemite fraction saturates at around  $\Phi = 1$ , which could be a result of oxygen diffusion from the surrounding atmosphere. As the oxygen flow in the flame decreases, the amount of diffused oxygen from the surroundings increases. Therefore, the real equivalence ratio probably cannot be raised much above 1 in an open flame setup. In contrast, the low end of the curve seems very sensitive to changes in the equivalence ratio. With the synthesis setup used, it was difficult to obtain a stable flame with lower  $\Phi$  values, so we did not go any lower. However, experimenting with even lower equivalence ratios offers an interesting path for future work with experimental setup modification. It would be interesting to see how far down this curve can



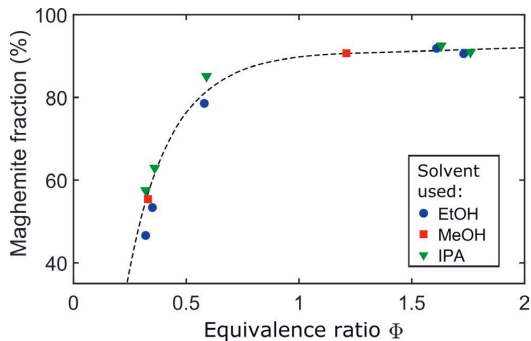


**FIGURE 2** The weight percentage of maghemite as a function of equivalence ratio in samples synthesized using different alcohols as the solvent. The rest of the samples consisted of hematite phase

predict the phase composition. Based on these results, EtOH might be the best of these three alternatives for a solvent, when trying to reach higher hematite fractions.

Even though preceding literature indicates that open flame samples should contain maghemite but no magnetite, we wanted to confirm this with Raman microscopy. Figure 3 shows the optical microscope images along with the recorded Raman spectra from the indicated locations for three samples with different gas flows. The calculated weight percentages from Rietveld refinement for each phase are presented above the micrographs for the corresponding samples. Also, typical spectra for hematite and maghemite along with characteristic features are marked.

The measurements of all samples basically only gave two kinds of spectra, or some combination of these, that can be identified as maghemite and hematite, based on the literature.<sup>37,38,40</sup> None of the measurements gave a pattern that would clearly resemble that of magnetite, so we concluded that the powders comprise only maghemite and hematite. The hematite patterns show clearly the typical two  $A_{1g}$  modes (226 and 500  $\text{cm}^{-1}$ ) and the five  $E_g$  modes (245, 293, 298, 413 and 612  $\text{cm}^{-1}$ ).<sup>41</sup> The peaks at 293 and 298  $\text{cm}^{-1}$  are overlapping a bit, but they can be distinguished based on the shape of the peak. In addition to these, there is a residual peak at around 660  $\text{cm}^{-1}$ , which is often seen in hematite samples.<sup>37</sup> According to Zoppi et al.,<sup>42</sup> it might originate from the lack of long-range order or an impurity phase. The intense peak at 1320  $\text{cm}^{-1}$  comes from a two-magnon scattering arising from hematite's antiferromagnetic nature.<sup>38</sup>

Maghemite can be identified by four broad bands at around 350, 500, 700, and 1440  $\text{cm}^{-1}$ .<sup>38,43</sup> However, for maghemite the locations of the peaks are not as well determined as for hematite. This might be due to the seeming uncertainty considering the exact structure of maghemite, as multiple possible structure models have been reported in the literature.<sup>44-46</sup> Nevertheless, the recorded patterns fit many reported patterns well. The three

main peaks used for the identification refer to Raman active phonon modes  $T_{2g}$  (365  $\text{cm}^{-1}$ ),  $E_g$  (511  $\text{cm}^{-1}$ ), and  $A_{1g}$  (700  $\text{cm}^{-1}$ ).<sup>47</sup>

The optical micrographs of samples with low hematite fractions gave mostly brown/green background with small yellowish dots here and there. If the spectrum from anywhere in the dominant background was recorded, it indicated the maghemite phase, and if the laser was pointed to a yellow spot, either a hematite pattern or a sum of hematite and maghemite was recorded. This phenomenon was observed for all samples, and some additional images and patterns are presented in Figure S7. For some samples with fairly low hematite fractions, the hematite particles seemed to agglomerate together, forming large yellow areas. This could be due to differences in magnetic or electric properties between the particles of different phases. When the hematite fraction grew, the amount of the yellow area in the images increased and the phases blended together more, leading to more mixed phase Raman patterns. The Rietveld refinement and the Raman microscopy results support each other very well. The ratio of the yellow area with respect to brown/green gives a good indication of the actual phase composition. Since Raman microscopy requires very little sample preparation and the measurements are fast to perform, it could possibly be used as a quick, qualitative technique to give an idea of the phase composition of iron oxide samples. We did not come across any literature referring to similar optical phase characterization.

In addition to the phase composition, we were interested in the size distribution of the particles, since the primary particle size is an important factor considering the functionality of various applications. Figure 4 shows TEM images of some samples with different parameters and the primary particle size as a function of equivalence ratio.

The top row in Figure 4A represents the overwhelming majority of the TEM sample areas. Mostly the powders were composed of a very fine particle mode in the size range of 2-8 nm, depending on the process parameters. The estimated mean primary particle size,  $d_{TEM}$ , for the dominant fine mode was calculated from TEM images for those samples that were imaged. The size distributions for this dominant mode looked very narrow for all samples, most of the particles falling inside  $\pm 1-2$  nm from the average. If we consider the size of primary particles in different flame conditions, one of the most important factors is the residence time of the particles in the flame. One of the best single indicators for the residence time is the length of the flame, which determines the size of the high-temperature zone. Madler et al.<sup>31</sup> showed a linear dependence between the equivalence ratio and the flame height. This effect can be seen in Figure 4B. Even though the equivalence ratio is not the only factor affecting the residence time, the estimated average size of the dominant mode seems to follow it rather linearly. This indicates that the amount of evaporated precursor, and therefore residual particles, is probably reasonably similar in all samples. A significant decrease in the

residual mode would most likely tilt the correlation. Based on the average crystallite sizes, simply raising the equivalence ratio has little effect on the formation of the residual mode, but it rather mostly affects the size of the fine mode and the phase composition. We tried to briefly with four samples, I1, I5, E1, and E5, see if halving or doubling the liquid feed rate has a large impact on the phase ratio and residual particles. Since no clear differences were visible in the XRD data, liquid-to-gas ratio is most likely not a very important factor in this regard.

The bottom row in Figure 4A represents the very few areas present on the TEM samples that revealed collections of significantly larger particles that had a very wide size distribution ranging from tens of nanometers to several hundred nanometers. This mode is presumed to be a so-called residual mode that has formed from precursor solution droplets that did not evaporate after atomization, whereas the fine mode has most likely nucleated from gas phase after complete evaporation.<sup>25,32</sup> We could not find these large particles in every sample, so we used the average crystallite sizes obtained from Rietveld refinement to indicate the presence of residual particles. Since some of these particles are two orders of magnitude larger than most, even a small amount of them gives a significant contribution to the measured XRD patterns. These particles seemed to be mostly single crystals, but the TEM images were not adequate to tell for certain. The average crystallite sizes obtained from Rietveld refinement ranged a lot between 27.3 and 515.0 nm (Table S1), varying between the two phases. It does not give a reliable measure for the particle size, but strongly indicates the presence of residual particles in all samples. Also, the phases do not seem to have large enough difference in total for the residual mode to only consist of maghemite or hematite. Most likely, both phases have a mixed composition. This indicates that the phase of a particle is not directly dependent on the formation path, when considering gas-to-particle versus droplet-to-particle routes.

One of the possible ways for the formation of residual particles is hydrolysis in the liquid phase.<sup>37</sup> The precursor itself contains crystal water, but much more water vapor forms in the  $H_2/O_2$  flame. Since alcohols are generally soluble with water, this could allow condensation of water vapor and dissolution to the droplets. However, hydrolysis of iron nitrate should lead to hematite.<sup>37,48</sup> Because it seems that hematite is present in both phases, this is likely not the only mechanism involved. Condensating water can also hinder the combustion of the solution droplets, leading to incomplete combustion.<sup>49</sup> A challenge for future studies is removing the residual mode while maintaining the phase control.

### 3.2 | Mixtures of alcohols and carboxylic acids

We wanted to study the effect of carboxylic acids in the solvent on the phase composition of the produced powder.

It was hypothesized earlier that the hematite portion of the particles could come from the residual mode. The results presented above, however, contradict this assumption. EHA has been used before to eliminate residual particles in flame synthesis.<sup>26,50</sup> Rosebrock et al<sup>49,51</sup> found in single droplet experiments that in some cases the addition of EHA to the precursor solution led to strong droplet explosions, which led to smaller particles. We wanted to see the effects of three carboxylic acids with differing chain lengths. 50% of the MeOH volume in the precursor solution was substituted with an equal volume of PropA, ButA, and EHA. Also, the effect of the amount of EHA was studied by making 5, 15, and 30% substitutions in addition to the 50% samples. For most of the samples, only one set of gas flows, namely 20 L/minutes of  $H_2$  and 35 L/minutes of  $O_2$ , was chosen to emphasize the role of the solvent, because a shift in the direction of either phase would become most visible. Surprisingly, the addition of carboxylic acids erased the hematite phase completely in all cases, even though the equivalence ratios were very low (0.33-0.35). Figure 5A compares the XRD patterns of three samples with identical gas flows, but different solvent compositions. The pattern of M2 was slightly scaled down to fit the intensities of the other samples better. Therefore, Figure 5A does not represent the amounts of phases between the samples.

The powders that had 5 vol-% of EHA and 50 vol-% of PropA gave almost identical XRD patterns with strong reflections, and all of the hematite peaks vanished compared with the pure MeOH sample. When at least 15 vol-% of EHA was added to the solution, the XRD peaks got broader and weaker (Figures S5 and S6). Also, a larger background was measured for these samples. This refers to smaller particle sizes, but also to the possible presence of amorphous material and carbonaceous residua. The low intensities with a high background made Rietveld refinement quite difficult, and the average crystal sizes cannot be regarded very reliable. This, however, indicates a lower amount of large particles.

The purity of the phase was also characterized by Raman microscopy, and the results from the alcohol samples can be used to analyze the acquired data. Figure 5B presents two Raman micrographs and the recorded spectra from the marked locations. All of the recorded patterns from carboxylic acid samples gave only maghemite patterns and all microscope images showed the absence of the yellow areas indicating hematite. At some spots, very weak spectra without clear peaks were recorded, which in part indicates incomplete crystallization (Figure S8). Since our emphasis was on phase control, we did not try different gas flows, but increasing the equivalence ratio could lead to a higher degree of crystallization through longer residence times and higher temperatures.

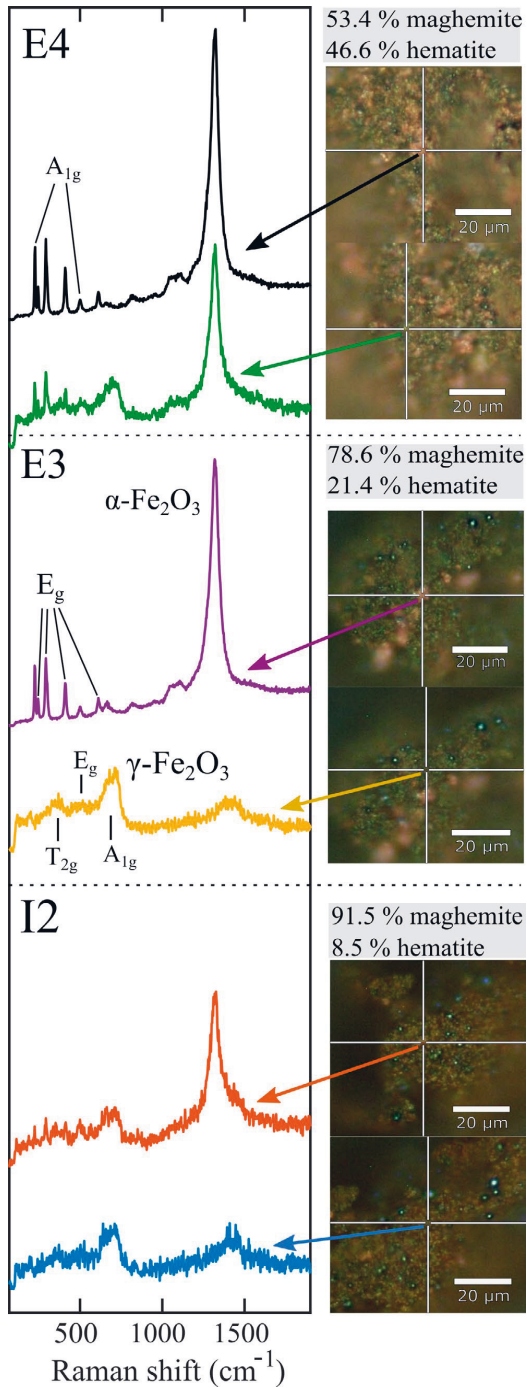


**FIGURE 3** Optical micrographs of three different alcohol samples (E4, E3 and I2) and the recorded Raman spectra from the indicated locations. The corresponding phase compositions obtained by Rietveld analysis are presented above the micrographs. Typical hematite and maghemite patterns and the characteristic peaks are also marked

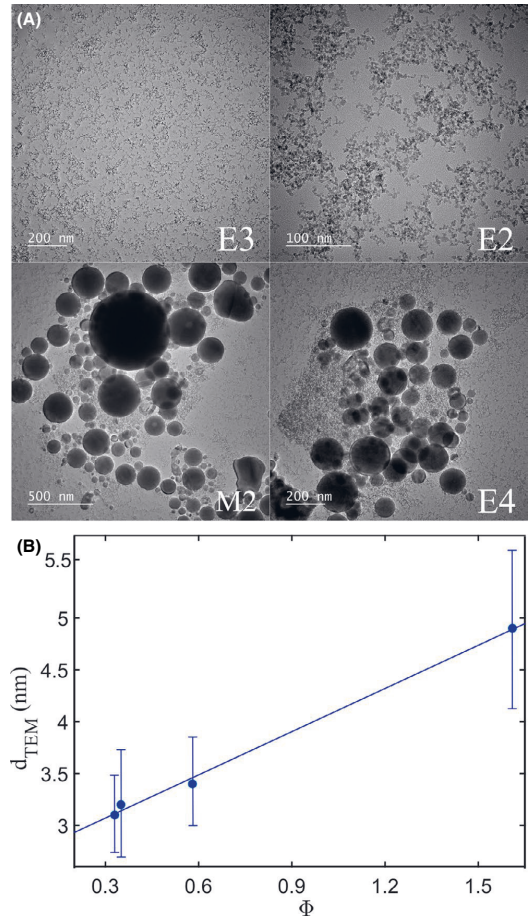


**FIGURE 4** A, TEM images of some samples (E2, E3, E4 and M2) produced with pure alcohols as solvents and B, the average primary particle size as a function of equivalence ratio. The standard deviations are marked with error bars. In (A), the top row represents the majority of the sample areas and the bottom row the very few areas with larger particles

Just like for the alcohol samples, TEM imaging was used to characterize the primary particle size. Figure 6 shows TEM images of various samples produced with

different amounts of EHA in the precursor solution. In accordance to Figure 4, the top row shows the dominant phase of the TEM sample areas, whereas the bottom row represents the very few areas with larger particles. These are the largest collections of residual particles that were

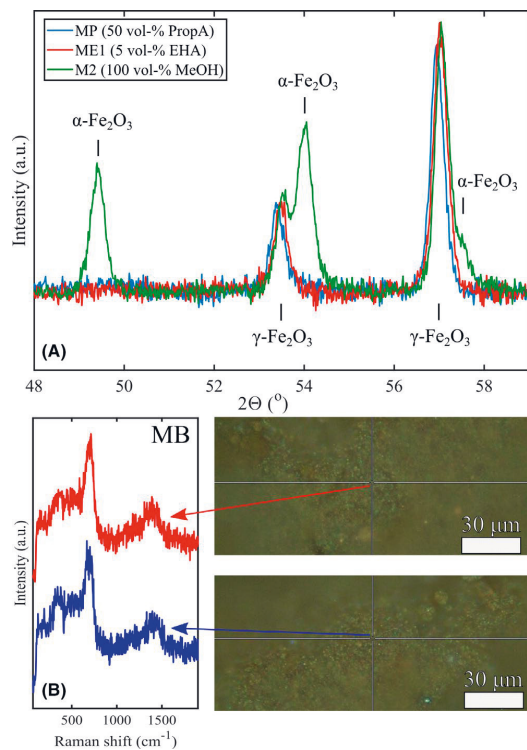


**FIGURE 5** A, Patterns of three XRD reflections of a MeOH sample (M2) and two samples with identical gas flows, but carboxylic acids added to the solvent mixture (MP and ME1), and B, optical micrographs with recorded Raman spectra from the sample with butanoic acid. The pattern of M2 was slightly scaled down to fit the intensities of the other samples to better emphasize the disappearance of the hematite peaks

found in the samples in question. As the amount of EHA in the precursor solution increased, the primary particle size in the fine mode also increased. Simultaneously, the amount and the size of the residual particles decreased. These two processes counteracting each other makes sense, because the elimination of the residual mode increases the amount of evaporated precursor in the flame, which then leads to enhanced condensation and growing particle size. Figure 7 shows the  $d_{\text{TEM}}$  values calculated from the TEM images values as a function of HOC of the corresponding precursor solution, which turned out to be a better indicator than  $\Phi$  in this case.

The blue dots in Figure 7, referring to EHA samples, fall quite well on a straight line, but the one data point with propanoic acid seems to be an outlier. This is presumably caused by the different chemistry between the two carboxylic acids. Now, the equivalence ratio does not change much and the increase in the primary particle size stems from the elimination

of residual particles. Based on TEM images, the 50 vol-% substitution with the two shorter-chained carboxylic acids still led to formation of a significant amount of larger particles, as with alcohol samples. The same thing also happened with 5 vol-% substitution with EHA, but as the fraction of EHA in the solvent mixture was raised, less residual particles were found, and at 30 vol-% they seemed to be mostly gone. As was mentioned before, the average crystallite sizes are not reliable due to poor refinement, but the significantly lower values for the samples with 15, 30, and 50 vol-% of EHA in the precursor solution compared to others (12.7, 8.6, and 11.5 nm, respectively) indicate a lower amount of large particles. The mechanism of residual reduction behind the increasing addition of EHA could be studied by testing if the same effect can be achieved by adjusting the gas flows for solutions with lower EHA content.

Strobel and Pratsinis<sup>26</sup> produced homogeneous nanoparticles from metal nitrates by adding carboxylic acids to the solution, but our results indicate that this does not always lead to the elimination of the residual mode, but it rather turns the hematite phase into maghemite. The reason for this is still uncertain. They suggested that nitrates could be converted into carboxylates at elevated temperatures in the presence of carboxylic acids. Also, Chiarello et al<sup>52</sup> stated that fast heating would lead to the formation of metal complexes when using metal nitrates. It is possible that carboxylic acids turn the iron nitrate into a metal complex that has no formation route to hematite in flame conditions, even with high oxygen concentrations. We did not find studies that would confirm this in FSP synthesis, though. There is research regarding chemical synthesis of iron oxide nanoparticles that introduce various chemicals to turn iron nitrate into other intermediate precursors. Habibi and Kiani<sup>53</sup> turned iron nitrate into iron(III) citrate by reacting it with citric acid, iron(III) acetate by reacting it with ammonium acetate and iron(III) oxalate by reacting it with oxalic acid. This kind of reactions, if fast enough, could happen in the flame, and lead to various reaction routes into the final product.

Meierhofer et al<sup>54</sup> produced  $\text{Li}_4\text{Ti}_5\text{O}_{12}$  particles from different precursor/solvent combinations. The highest quality particles were obtained from solutions containing EHA. They stated that for titanium isopropoxide, EHA could prevent hydrolysis/condensation reactions. If hydrolysis is the reason for the presence of hematite phase, similar effect with iron nitrate could explain this. They also observed in single droplet experiments that addition of EHA led to earlier microexplosions of precursor solution droplets promoted the release of the precursors into the gas phase. These two effects could at least in part be responsible for the decrease in residual particle size and number.

Grigorie et al<sup>55</sup> produced hematite and maghemite from iron(III) nitrate by thermal decomposition. They mixed the precursor with various amounts of polyethylene glycol

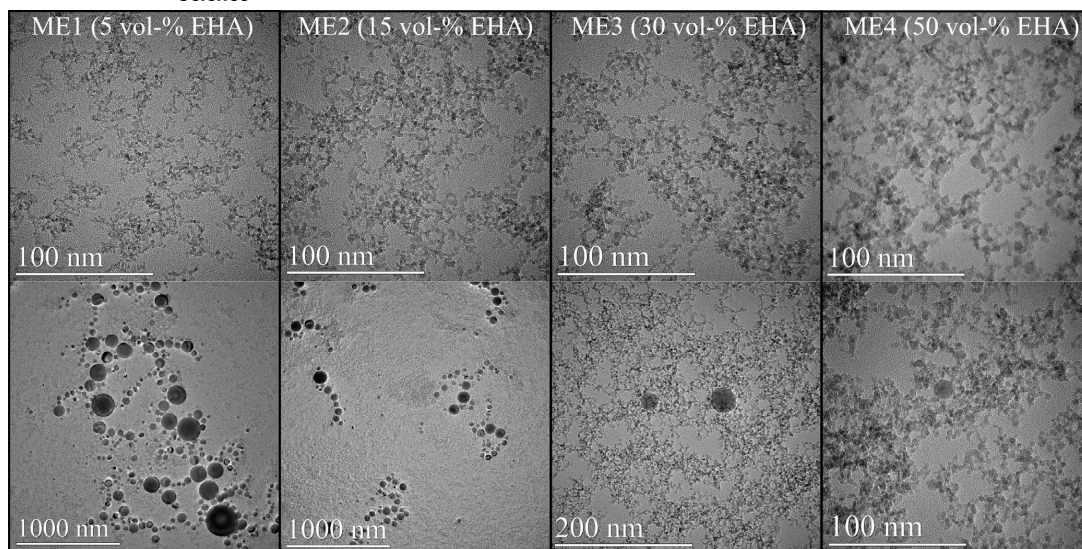


**FIGURE 6** TEM images of samples with different volume fractions of MeOH substituted with EHA. The top row represents the majority of the sample areas, whereas the bottom row shows the largest collection of residual particles found on the samples

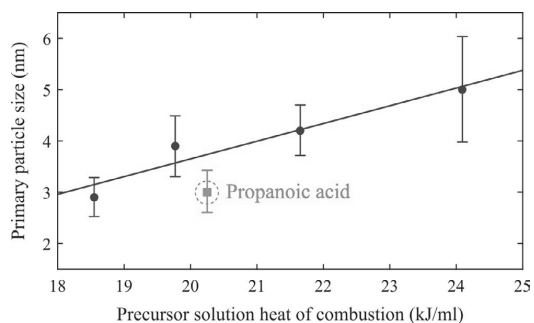


**FIGURE 7** The average primary particle sizes calculated from TEM images for carboxylic acid-containing samples as a function of the heat of combustion for the precursor solution. The blue dots refer to samples containing increasing amount of EHA and the red square contained 50 vol-% propanoic acid. The standard deviations are marked with error bars

(PEG), which worked as a reducing agent. With low PEG concentration, mostly hematite was formed, but as the concentration was raised adequately, it turned into maghemite. Perhaps carboxylic acids provide a similar reducing environment in the flame. The conclusions from chemical syntheses in much lower temperatures and longer times are not directly applicable to LFS conditions, but they could give a hint of the actual mechanisms. This should be tested by adding other reducing agents to the precursor solution instead of carboxylic

acids. If this is the reason for the elimination of the hematite phase, addition of oxidizing agents to the solution could potentially increase the hematite fraction. The incompatibility of strong oxidizers with flammable solvents presents a challenge, however.

These results support further the claim that the residual mode and the hematite phase are not directly linked to each other, as clearly bimodal particle size distributions were found for MP, MB, ME1, ME2, and all of the alcohol samples. It would be interesting to see if using an alcohol with higher heat of combustion mixed with carboxylic acids could be used for eliminating the residual mode with a lower carboxylic acid content. According to Jossen et al.<sup>32</sup>, a large ratio of solvent boiling point to precursor melting point would also promote the production of homogeneous particles. This would partly explain the differences between PropA, ButA, and EHA, as their boiling points are 141.5, 163.8, and 288.1°C, respectively, compared with that of MeOH (64.7°C).

## 4 | CONCLUSIONS

Iron oxide particles can form in various different crystallographic phases. We investigated how the phase of iron oxide nanoparticles can be controlled in liquid flame spray synthesis when using iron(III) nitrate as the precursor. We succeeded in finding process parameters to intentionally adjust the hematite/maghemite ratio of flame-synthesized iron oxide nanoparticles



in a systematic way. We are not aware of earlier studies where the hematite/maghemite ratio has been tuned in a flame-based method. Therefore, we believe that these results will increase the potential of cost-effective nitrate precursors for generating highly dispersed iron oxide nanomaterials.

The solvent composition and the oxygen and hydrogen gas flow rates were the main parameters studied. All collected powder samples were found to consist of either maghemite or a mixture of maghemite and hematite phases, along with possible amorphous material. In nanoparticle synthesis from a liquid precursor, unwanted larger residual particles can form as a result of incomplete evaporation. We were also interested in the influence of residual particles in the phase composition.

When different pure alcohols (methanol, ethanol, or isopropanol) were used as solvents, equivalence ratio that describes the amount of oxygen in the flame zone was found to have a strong correlation with the phase ratio. Oxygen-rich conditions pushed the ratio toward hematite, whereas oxygen-lean conditions promoted maghemite formation, but always having both phases present. Even though most of the particles were very small (2–8 nm), all alcohol samples contained a residual mode that consisted of significantly larger particles (up to several hundred nanometers). Both particle modes seemed to consist of a mixture of the two phases. The equivalence ratio affected the primary particle size of the dominant fine mode in addition to the phase composition.


Mixing carboxylic acids (propionic acid, butanoic acid, or 2-ethylhexanoic acid) with methanol in the solvent mixture led to the complete elimination of the hematite phase, which indicates that the effect of equivalence ratio to the phase composition is tightly linked to the chemical composition of the precursor solution. This happened possibly due to a carboxylic acid-induced conversion of iron nitrate to an intermediate metal complex that has no formation path into hematite in the flame conditions, but this could not be confirmed. When using the two shorter-chained carboxylic acids with low heat of combustion or a small amount of 2-ethylhexanoic acid, a significant amount of residual particles formed. The size and the number of residual particles could, however, be changed by adjusting the mixing ratio of methanol and 2-ethylhexanoic acid, but simultaneously leaving possibly amorphous material. As the amount of 2-ethylhexanoic acid increased in the solvent mixture, simultaneously raising its heat of combustion, the residual mode shrunk. The more complete evaporation of the precursor solution led to an increase in the primary particle size.

The interplay of all different parameters and the precursor solution chemistry is not yet fully understood. More research is needed to understand the impact of different parameters in controlling the phase of iron oxide particles in FSP synthesis, while simultaneously ensuring their homogeneity.

## ACKNOWLEDGMENTS

M. Sorvali and P. Juuti want to acknowledge the TUT graduate school for financial support. This work made use of Tampere Microscopy Center facilities at Tampere University.

## ORCID

Miika Sorvali  <https://orcid.org/0000-0003-2697-4922>

## REFERENCES

1. Wu W, He Q, Jiang C. Magnetic iron oxide nanoparticles: synthesis and surface functionalization strategies. *Nanoscale Res Lett.* 2008;3:397–415.
2. Teja AS, Koh P-Y. Synthesis, properties, and applications of magnetic iron oxide particles. *Prog Cryst Growth Ch.* 2009;55: 22–45.
3. Laurent S, Forge D, Port M, Roch A, Robic C, Elst LV, et al. Magnetic iron oxide nanoparticles: synthesis, stabilization, vectorization, physicochemical characterizations, and biological applications. *Chem Rev.* 2008;108:2064–110.
4. Nosrati H, Salehiabar M, Fridoni M, Abdollahifar M-A, Manjili HK, Davaran S, et al. New insight about biocompatibility and biodegradability of iron oxide magnetic nanoparticles: stereological and in vivo MRI monitor. *Sci Rep.* 2019;9:7173.
5. Gijs MAM, Lacharme F, Lehmann U. Microfluidic applications of magnetic particles for biological analysis and catalysis. *Chem Rev.* 2010;110:1518–63.
6. Hsu M-C, Alfadhel A, Forouzandeh F, Borkholder DA. Biocompatible magnetic nanocomposite microcapsules as microfluidic one-way diffusion blocking valves with ultra-low opening pressure. *Mater Des.* 2018;150:86–93.
7. Jönkkäri I, Sorvali M, Huhtinen H, Sarlin E, Salminen T, Haapanen J, et al. Characterization of bidisperse magnetorheological fluids utilizing maghemite ( $\gamma$ -Fe<sub>2</sub>O<sub>3</sub>) nanoparticles by flame spray pyrolysis. *Smart Mater Struct.* 2017;26(6):095004.
8. Kciuk M, Turczyn R. Properties and application of magnetorheological fluids. *JAMME.* 2006;18(1–2):127–30.
9. Gupta AK, Gupta M. Synthesis and surface engineering of iron oxide nanoparticles for biomedical applications. *Biomaterials.* 2005;26:3995–4021.
10. Usov NA. Iron oxide nanoparticles for magnetic hyperthermia. *SPIN.* 2019;9(2):1940001.
11. Zhu J, Lu Y, Chen C, Ge Y, Jasper S, Leary JD, et al. Porous one-dimensional carbon/iron oxide composite for rechargeable lithium-ion batteries with high and stable capacity. *J Alloy Compd.* 2016;672:79–85.
12. Park J, Yoo H, Choi J. 3D ant-nest network of  $\alpha$ -Fe<sub>2</sub>O<sub>3</sub> on stainless steel for all-in-one anode for Li-Ion battery. *J Power Sources.* 2019;431:25–30.
13. Aronniemi M, Saino J, Lahtinen J. Characterization and gas-sensing behavior of an iron oxide thin film prepared by atomic layer deposition. *Thin Solid Films.* 2008;516:6110–5.
14. Demirci S, Yurddaskal M, Dikici T, Saroğlu C. Fabrication and characterization of novel iodine doped hollow mesoporous hematite (Fe<sub>2</sub>O<sub>3</sub>) particles derived from sol-gel method and their photocatalytic performances. *J Hazard Mater.* 2018;345: 27–37.

15. Tamirat AG, Rick J, Dubale AA, Su W-N, Hwang B-J. Using hematite for photoelectrochemical water splitting: a review of current progress and challenges. *Nanoscale Horiz.* 2016;1:243–67.
16. Li D, Teoh WY, Selomulya C, Woodward RC, Amal R, Rosche B. Flame-sprayed superparamagnetic vare and silica-coated maghemite nanoparticles: synthesis, characterization, and protein adsorption-desorption. *Chem Mater.* 2006;18:6403–13.
17. Li Q, Kartikowati CW, Horie S, Ogi T, Iwaki T, Okuyama K. Correlation between particle size/domain structure and magnetic properties of highly crystalline  $\text{Fe}_3\text{O}_4$  nanoparticles. *Sci Rep.* 2017;7:9894.
18. Jolivet J-P, Chanéac C, Tronc E. Iron oxide chemistry. From molecular clusters to extended solid networks. *Chem Commun.* 2004;10:481–3.
19. Tadić M, Čitaković N, Panjan M, Stojanović Z, Marković D, Spasojević V. Synthesis, morphology, microstructure and magnetic properties of hematite submicron particles. *J Alloys Compd.* 2011;509:7639–44.
20. Ruusunen J, Ihalainen M, Koponen T, Torvela T, Tenho M, Salonen J, et al. Controlled oxidation of iron nanoparticles in chemical vapour synthesis. *J Nanopart Res.* 2014;16:2270.
21. Strobel R, Pratsinis SE. Direct synthesis of maghemite, magnetite and wustite nanoparticles by flame spray pyrolysis. *Adv Powder Technol.* 2009;20:190–4.
22. Kumfer BM, Shinoda K, Jayadevan B, Kennedy IM. Gas-phase flame synthesis and properties of magnetic iron oxide nanoparticles with reduced oxidation state. *J Aerosol Sci.* 2010;41:256–65.
23. Li Y, Hu Y, Huang G, Li C. Metallic iron nanoparticles: flame synthesis, characterization and magnetic properties. *Particuology.* 2013;11:460–7.
24. Mäkelä JM, Aromaa M, Rostedt A, Krinke TJ, Janka K, Marjamäki M, et al. Liquid flame spray for generating metal and metal oxide nanoparticle test aerosol. *Hum Exp Toxicol.* 2009;28(6–7):421–31.
25. Mäkelä JM, Haapanen J, Harra J, Juuti P, Kujanpää S. Liquid flame spray – a hydrogen-oxygen flame based method for nanoparticle synthesis and functional nanocoatings. *KONA Powder Part J.* 2017;34:141–54.
26. Strobel R, Pratsinis SE. Effect of solvent composition on oxide morphology during flame spray pyrolysis of metal nitrates. *Phys Chem Chem Phys.* 2011;13:9246–52.
27. Buyukhatipoglu K, Clyne AM. Controlled synthesis of  $\alpha\text{Fe}_2\text{O}_3$  and  $\text{Fe}_3\text{O}_4$  nanoparticles: effect of flame configuration, flame temperature, and additive loading.
28. Aromaa M, Keskinen H, Mäkelä JM. The effect of process parameters on the Liquid Flame Spray generated titania nanoparticles. *Biomol Eng.* 2007;24:543–8.
29. Kammler HK, Mädler L, Pratsinis SE. Flame synthesis of nanoparticles. *Chem Eng Technol.* 2001;24(6):583–96.
30. Tikkanen J, Gross KA, Berndt CC, Pitkänen V, Keskinen J, Raghu S, et al. Characteristics of the liquid flame spray process. *Surf Coat Technol.* 1997;90:210–6.
31. Mädler L, Stark WJ, Pratsinis SE. Flame-made ceria nanoparticles. *J Mater Res.* 2002;17(6):1356–62.
32. Jossen R, Pratsinis SE, Stark WJ, Mädler L. Criteria for flame-spray synthesis of hollow, shell-like, or inhomogeneous oxides. *J Am Ceram Soc.* 2005;88(6):1388–93.
33. Mädler L, Kammler HK, Mueller R, Pratsinis SE. Controlled synthesis of nanostructured particles by flame spray pyrolysis. *J Aerosol Sci.* 2002;33:369–89.
34. Aromaa M, Arffman A, Suhonen H, Haapanen J, Keskinen J, Honkanen M, et al. Atmospheric synthesis of superhydrophobic  $\text{TiO}_2$  nanoparticle deposits in a single step using Liquid Flame Spray. *J Aerosol Sci.* 2012;52:57–68.
35. Keskinen H, Aromaa M, Heine MC, Mäkelä JM. Size and velocity measurements in sprays and particle producing flame sprays. *Atom Sprays.* 2008;18:1–26.
36. Birkenstock J, Fischer RX, Messner T. BRASS 1.0beta: The Bremen Rietveld Analysis and Structure Suite. *Zentrallabor für Kristallographie und Angewandte Materialwissenschaften, Fachbereich Geowissenschaften, University of Bremen* 2003.
37. Bersani D, Lottici PP, Montenero A. Micro-Raman investigation of iron oxide films and powders produced by sol-gel syntheses. *J Raman Spectrosc.* 1999;30:355–60.
38. De Faria DLA, Silva SV, Oliveira MT. Raman microscopy of some iron oxides and oxyhydroxides. *J Raman Spectrosc.* 1997;28:873–8.
39. Wieczorek-Ciurrow K, Kozak AJ. The thermal decomposition of  $\text{Fe}(\text{NO}_3)_3 \cdot 9\text{H}_2\text{O}$ . *J Therm Anal Calorim.* 1999;58:647–51.
40. Hanesh M. Raman spectroscopy of iron oxides and (oxy)hydroxides at low laser power and possible applications in environmental magnetic studies. *Geophys J Int.* 2009;177:941–8.
41. Beattie IR, Gilson TR. The single-crystal Raman spectra of nearly opaque materials. Iron(III) oxide and chromium(III) oxide. *J Chem Soc.* 1970:980–6.
42. Zoppi A, Lofrumento C, Castellucci EM, Migliorini MG. The Raman spectrum of hematite: possible indicator for a compositional firing distinction among terra sigillata wares. *Ann Chim-Rome.* 2005;95:239–46.
43. Ohtsuka T, Kubo K, Sato N. Raman spectroscopy of thin corrosion films on iron at 100 to 150 °C in air. *Corrosion.* 1986;42(8):476–81.
44. Pecharrromán C, González-Carreño T, Iglesias JE. The infrared dielectric properties of maghemite,  $\gamma\text{-Fe}_2\text{O}_3$  from reflectance measurement on pressed powders. *Phys Chem Miner.* 1995;22(1):21–9.
45. Jørgensen J-E, Mosegaard L, Thomsen LE, Jensen TR, Hanson JC. Formation of  $\gamma\text{-Fe}_2\text{O}_3$  nanoparticles and vacancy ordering: an in situ X-ray powder diffraction study. *J Solid State Chem.* 2007;180(1):180–5.
46. Solano E, Frontera C, Puig T, Obradors X, Ricart S, Ros J. Neutron and X-ray diffraction study of ferrite nanocrystals obtained by microwave-assisted growth. A structural comparison with the thermal synthetic route. *J Appl Crystallogr.* 2014;47:414–20.
47. Jubb AM, Allen HC. Vibrational spectroscopic characterization of hematite, maghemite, and magnetite thin films produced by vapor deposition. *ACS Appl Mater Interfaces.* 2010;2(10):2804–12.
48. Voigt B, Göbler A. Formation of pure haematite by hydrolysis of iron(III) salt solutions under hydrothermal conditions. *Cryst Res Technol.* 1986;21(9):1177–83.
49. Rosebrock CD, Riefler N, Wriedt T, Mädler L, Tse SD. Disruptive burning of precursor/solvent droplets in flame-spray synthesis of nanoparticles. *AIChE J.* 2013;59(12):4553–66.
50. Harra J, Kujanpää S, Haapanen J, Juuti P, Mäkelä JM. Aerosol analysis of residual and nanoparticle fractions from spray pyrolysis of poorly volatile precursors. *AIChE J.* 2017;63(3):881–92.
51. Rosebrock CD, Wriedt T, Mädler L, Wegner K. The role of micro-explosions in flame spray synthesis for homogeneous nanopowders from low-cost metal precursors. *AIChE J.* 2016;62(2):381–91.
52. Chiarello GL, Rossetti I, Forni L, Lopinto P, Migliavacca G. Solvent nature effect in preparation of perovskites by flame pyrolysis 2.

- Alcohols and alcohols + propionic acid mixtures. *Appl Catal B Environ.* 2007;72:227–32.
53. Habibi MH, Kiani N. Preparation of single-phase  $\alpha$ -Fe(III) oxide nanoparticles by thermal decomposition. Influence of the precursor properties. *J Therm Anal Calorim.* 2013;112:573–7.
54. Meierhofer F, Li H, Gockeln M, Kun R, Grieb T, Rosenauer A, et al. Screening precursor-solvent combinations for  $\text{Li}_4\text{Ti}_5\text{O}_{12}$  energy storage material using flame spray pyrolysis. *ACS Appl Mater Interfaces.* 2017;9:37760–77.
55. Grigorie AC, Muntean C, Stefanescu M. Obtaining of  $\gamma$ - $\text{Fe}_2\text{O}_3$  nanoparticles by thermal decomposition of polyethyleneglycol-iron nitrate mixtures. *Thermochim Acta.* 2015;621:61–7.

## SUPPORTING INFORMATION

Additional supporting information may be found online in the Supporting Information section at the end of the article.

**How to cite this article:** Sorvali M, Nikka M, Juuti P, et al. Controlling the phase of iron oxide nanoparticles fabricated from iron(III) nitrate by liquid flame spray. *Int J Ceramic Eng Sci.* 2019;1:194–205. <https://doi.org/10.1002/ces2.10025>



# PUBLICATION

II

**Crystallographic phase formation of iron oxide particles produced from  
iron nitrate by liquid flame spray with a dual oxygen flow**

**Sorvali, M., Honkanen, M., Hyvärinen, L., Kuisma, R., Larjo, J. and Mäkelä, J. M.**

*International Journal of Ceramic Engineering and Science* 3.5 (2021), 227–236


DOI: 10.1002/ces2.10102

**Publication reprinted with the permission of the copyright holders**



## RESEARCH ARTICLE

# Crystallographic phase formation of iron oxide particles produced from iron nitrate by liquid flame spray with a dual oxygen flow

Miika Sorvali<sup>1</sup>  | Mari Honkanen<sup>2</sup> | Leo Hyvärinen<sup>3</sup> | Ritva Kuisma<sup>4</sup> | Jussi Larjo<sup>5</sup> | Jyrki M. Mäkelä<sup>1</sup>

<sup>1</sup>Aerosol Physics Laboratory, Physics Unit, Faculty of Engineering and Natural Sciences, Tampere University, Tampere, Finland

<sup>2</sup>Tampere Microscopy Center, Tampere University, Tampere, Finland

<sup>3</sup>Engineering Materials Science, Materials Science and Environmental Engineering Unit, Faculty of Engineering and Natural Sciences, Tampere University, Tampere, Finland

<sup>4</sup>Research Center Terra, Tampere University, Tampere, Finland

<sup>5</sup>Oseir Ltd, Tampere, Finland

## Correspondence

Miika Sorvali, Aerosol Physics Laboratory, Physics Unit, Faculty of Engineering and Natural Sciences, Tampere University, P.O. Box 692, FI-33014 Tampere, Finland.  
Email: miika.sorvali@tuni.fi

## Funding information

TUT/TAU Graduate school

## Abstract

We fabricated iron oxide particles from iron(III) nitrate in a liquid flame spray synthesis. Unlike in most liquid flame spray studies, we implemented a secondary oxygen flow. The effect of the gas flow setup and two additives to the precursor solution, oxalic acid and citric acid, on the resulting particles was studied, with the focus on crystallographic phase composition. The synthesis yielded either pure maghemite or maghemite/hematite mixed phase powders. For solutions without additives, the maghemite fraction was almost linearly dependent on the equivalence ratio. The specific surface area was highest for the smallest equivalence ratios, then decreased, and increased again for the highest values. Some variation was observed between samples with equal equivalence ratios but the total oxygen flow divided differently between the two oxygen channels, a higher atomization flow promoting larger hematite fraction, and higher specific surface area. Both additives reduced the amount of hematite in the powder samples, citric acid being the more efficient one. Citric acid slightly raised the specific surface area, whereas oxalic acid dropped it in half.

## KEYWORDS

iron oxide, liquid flame spray, nanoparticles, synthesis

## 1 | INTRODUCTION

Iron oxide is among the most relevant nanomaterials nowadays. It is special in the sense that it occurs in different crystallographic phases that manifest their own properties. Iron oxide particles are utilized in applications like biomedicine,<sup>1,2</sup> magnetorheological fluids,<sup>3,4</sup> and magnetic resonance imaging<sup>5,6</sup> in the two strongly magnetic phases, magnetite ( $\text{Fe}_3\text{O}_4$ ) and maghemite ( $\gamma\text{-Fe}_2\text{O}_3$ ),

and in gas sensors,<sup>7,8</sup> catalysts,<sup>9,10</sup> and lithium-ion batteries<sup>11,12</sup> in the antiferromagnetic hematite ( $\alpha\text{-Fe}_2\text{O}_3$ ) phase. Other phases, whose potential has been less studied, also exist.<sup>13,14</sup> Because different phases, or even phase mixtures, provide varying functionalities, there is interest to develop methods that offer efficient synthesis with control over the phase composition.

Different synthesis methods offer their own advantages. Several chemical methods can provide careful

This is an open access article under the terms of the Creative Commons Attribution License, which permits use, distribution and reproduction in any medium, provided the original work is properly cited.

© 2021 The Authors. International Journal of Ceramic Engineering & Science published by Wiley Periodicals LLC on behalf of American Ceramic Society

control of the particle properties, whereas simplicity, production speed, and upscalability are generally regarded as perks of flame methods. However, the fine tuning and the controllability of the end product is often challenging in a flame, where temperatures are high and time scales extremely short. Liquid flame spray (LFS), a specific type of flame spray pyrolysis (FSP) method, is in the focus of this article. Due to the difficulty of studying the very early stages of particle formation in flame synthesis, more experimental research is required to discover all the contributing factors. One of the still unclear parts of the process is the formation mechanisms of different phases and the factors that determine the eventual phase composition. Our goal is to shed a little more light into these processes through a specific experimental setup.

This study aims to build on the previous paper by Sorvali et al<sup>15</sup> that focused on factors affecting the phase of iron oxide nanoparticles produced in an LFS synthesis from iron(III) nitrate. The two main factors studied in the previous study were as follows: (a) the equivalence ratio ( $\varphi$ ), controlled through adjusting O<sub>2</sub> and H<sub>2</sub> gas flows, when using pure alcohols as solvents, and (b) substituting part of the alcohol with a carboxylic acid in the precursor solution. The material primarily consisted of maghemite and hematite.  $\varphi$ , meaning the amount of substance ratio between the oxygen fed to the flame compared to stoichiometric combustion conditions, was observed to have a strong correlation with the maghemite/hematite ratio. However, when part of the alcoholic solvent was replaced with carboxylic acid, the hematite phase disappeared, and the amount added had an impact on the particle size distribution.

Here, we switched the burner to another design that allowed more flexible adjustment of the gas flows, thereby reaching lower equivalence ratios by enabling higher amounts of oxygen to be fed into the flame zone. Since the burner offered more complex flow mechanics, the effect of varying the flow setup was also inspected. In addition, we explored the effect of dissolving citric acid (CitA) or oxalic acid (OxA) as an additive to the precursor solution. The hypothesis was that these additives could cause the formation of citrate and oxalate complexes in the flame as intermediate species, changing the reaction pathways and possibly impacting the phase composition analogously to the assumed effect for carboxylic acid.

## 2 | EXPERIMENTAL

### 2.1 | Materials

The precursor used was iron(III) nitrate nonahydrate (FeN) (Fe(NO<sub>3</sub>)<sub>3</sub>·9H<sub>2</sub>O, 98+% (metals basis), Alfa Aesar). The solvents and the additives used were methanol (MeOH; EMSURE® ACS, Reag. Ph Eur, Merck), ethanol (EtOH) (99.5+%, Altia Oyj), citric acid monohydrate (99.5+%, Tamro Oyj), and oxalic acid (98%, Alfa Aesar).

### 2.2 | Nanoparticle synthesis

All samples were produced with LFS, whose basic principles are described in the literature.<sup>16–18</sup> Traditionally in LFS, a single hydrogen flow and a single oxygen flow are used to produce a turbulent H<sub>2</sub>/O<sub>2</sub> flame, whereinto a liquid precursor solution is atomized with one of the two gas flows. Most of the published research utilizing LFS has been conducted in this sort of a setup and a burner with only two gas channels. However, we chose another burner design (earlier referred to as KP burner by Aromaa et al<sup>16</sup>) that has been used in a few recent studies.<sup>19–22</sup> With this burner, a small additional nitrogen flow is often added between the other flows to push the flame further from the burner head, thus keeping it clean.<sup>16</sup> We substituted this nitrogen flow with a secondary oxygen flow.

The burner has four gas channels as depicted in Figure 1, which makes adjusting the process more flexible compared to the other burner design with only two channels. With a single flow, there came a point when the pressure drop grew too large to increase the flow further, so the only way to raise the amount of oxygen in the flame zone (in an atmospheric synthesis process) was through an addition of a secondary oxygen flow. The choice of the specific gas flow setup will be addressed in the Results and discussion section.

The atomizing O<sub>2</sub> flow rate was varied between 5 and 15 slpm, and the secondary O<sub>2</sub> flow was between 5 and 60 slpm. The H<sub>2</sub> flow was fixed at 10 slpm, so we will be referring to the atomizing oxygen flow rate and the total oxygen flow rate simply by atomization flow ( $Q_{\text{at}}$ ) and total flow ( $Q_{\text{tot}}$ ). The iron nitrate precursor concentration was 0.54 M, which translates to 30 mg of Fe atoms per ml of precursor solution. The concentration was slightly lowered

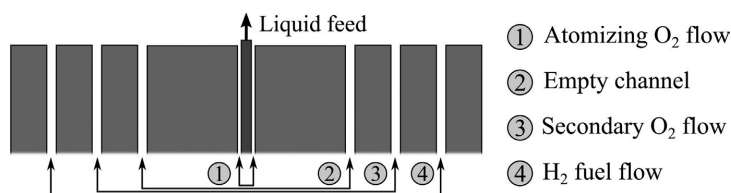


**FIGURE 1** A schematic of the burner head and the gas flow setup used in the synthesis

from the previous study to ensure complete solubility of all species in every precursor solution. The precursor solution feed rate was fixed at 2 ml/min, so  $Q_{\text{tot}}$  was the variable that practically defined the equivalence ratio in each case. For CitA and OxA samples, the additive was dissolved in the precursor solution after the dissolution of iron nitrate in methanol. The samples were collected as a powder with an electrostatic precipitator described by Sorvali et al.<sup>15</sup>

### 2.3 | Atomization measurements

The atomization measurements were performed with a HiWatch HR2 instrument from Oseir Ltd. The instrument utilizes localized extinction of a multi-pulse laser beam for particle detection. Extremely rapid stroboscopic backlight illumination is used to record spray cross-section images that are processed in order to calculate droplet diameter and velocity distributions, among other measures. The working principle is described in more detail by Koivuluoto et al.<sup>23</sup> The measurements were performed with an ethanol feed of 1, 2, and 4 ml/min into a single oxygen flow that was varied between 3 and 15 slpm. The lower cut size of diameter measurement was between 4 and 5  $\mu\text{m}$ , because the instrument could not distinguish droplets smaller than that. Ethanol was chosen instead of methanol for safety reasons.

### 2.4 | Characterization and sample preparation

X-ray powder diffraction (XRD; Panalytical Empyrean, monochromatized  $\text{CoK}_{\alpha}$  radiation) was used to characterize the crystal structures present in the samples. The phase compositions were calculated from the XRD data with Rietveld refinement by BRASS 2 program.<sup>24</sup> The crystal structure models used for iron oxide were obtained from American Mineralogist Crystal Structure Database (AMCSD) with the codes 0020585 for maghemite (space group Fd-3m) and 0000143 for hematite (space group R-3c), as in the previous study.<sup>15</sup>

Transmission electron microscope (TEM; JEOL JEM-F200) was utilized to image particles. The TEM samples were prepared by dispersing sample powders ultrasonically in ethanol and dipping a grid in the suspension. Braun-Emmett-Teller (BET) measurements were performed with Micromeritics FlowSorb III 2035/2310 in a single-point mode to assess the specific surface areas (SSA) of the sample powders. SSA describes the total surface area per mass unit ( $\text{m}^2/\text{g}$ ). The values were calculated as averages of measurements from two distinct samples of each powder, which together amounted to around 10%–30% of the total

powder volume. The measured samples were degassed in 200°C for 2 h.

## 3 | RESULTS AND DISCUSSION

### 3.1 | Iron nitrate in pure methanol

In the previous study,<sup>15</sup> methanol, ethanol, and isopropanol were used as solvents. Since the choice between the three had a relatively small effect on the phase composition, we chose methanol for this study, because it was observed to be the most effective in dissolving additives and provided the most stable solutions in the long term.

Determining a suitable gas flow setup required some experimentation. Since the burner has three gas channels in addition to the atomization channel, the secondary  $\text{O}_2$  flow and the  $\text{H}_2$  flow could be positioned in several ways (Figure 1). The secondary  $\text{O}_2$  flow was placed in the third channel, since using channel 2 led to significant accumulation of material onto the burner head. This was most likely due to swirling flows directed toward the liquid channel. When it was placed further from the liquid channel, the swirls weakened, greatly decreasing the accumulation. Placing the hydrogen flow between the two oxygen flows also had a similar fouling effect than using channel 2 for oxygen. The burning would initiate earlier, again leading to material accumulation, so it was put in the outermost channel.

The starting point of this study was reaching for lower  $\phi$  values than previously by modifying the setup to allow feeding higher amounts of oxygen into the flame zone. Due to the complex flow mechanics resulting from the additional  $\text{O}_2$  flow, we also wanted to study how the division of the total flow between the two channels affects the process and the end product. In theory, adjusting the flow division should impact the local flame temperatures, turbulence, and the residence time of the particles in the flame.

We initially chose three different atomization flows ( $Q_{\text{at}} = 5, 10, 15$  slpm) and total flows ( $Q_{\text{tot}} = 20, 35, 65$  slpm). A total of 11 samples were produced: three samples per each total flow and atomization flow ( $3 \times 3$  samples), plus two extra samples ( $Q_{\text{tot}} = 45, 55$  slpm) for the 10 slpm atomization flow. With this setup, a  $\phi$  range of 0.10–0.33 was achieved, and therefore, we continued down from where we left off in the previous study (0.32–1.76). Figure 2 shows the calculated weight fraction of maghemite (the rest was hematite) as a function of  $\phi$ , alongside the results from the previous study,<sup>15</sup> obtained with another burner design. The Rietveld plots and refinement parameters are presented in Figures S1–S4 and Table S1.

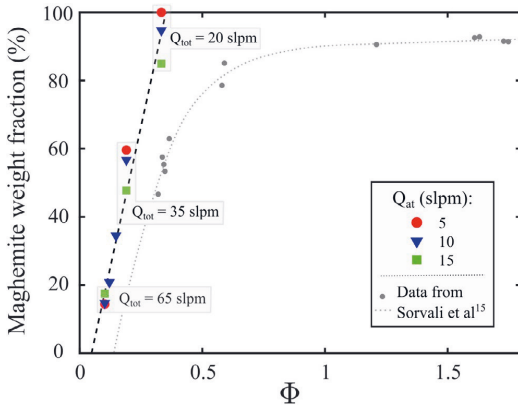


FIGURE 2 The maghemite fraction of the sample powders as a function of equivalence ratio. The results obtained in the previous study for another burner are plotted in grey for comparison. The total oxygen flows ( $Q_{tot}$ ) are marked for the three  $\varphi$  values (0.10, 0.19 and 0.33), where  $Q_{at}$  was varied, but  $Q_{tot}$  kept constant

Just like before, the equivalence ratio had a strong correlation with the maghemite/hematite weight ratio. However, there are two clear differences to the previous results: the shape of the curve for higher equivalence ratios and the position of the curve on the  $\varphi$  axis. With the other burner, we covered a wide  $\varphi$  range. In the low end, the relationship seemed quite linear, but as we moved to an equivalence ratio of roughly 0.5, the curve started to flatten out, and eventually saturated at around 90% maghemite fraction. This saturation was hypothesized to be caused by oxygen diffusion from the surrounding air as the flame conditions became very anoxic. Now that we only moved in very low equivalence ratios, the relationship remained fairly linear for the whole range, and no saturation was observed. Maybe the additional oxygen flow helped keep the flame zone atmosphere better controlled.

Switching the burner and the flow setup surprisingly shifted the curve toward lower  $\varphi$  values. The same equivalence ratio of 0.32–0.33 that earlier produced around 50/50 phase ratio resulted in even pure maghemite (for  $Q_{at} = 5$  slpm), which could not be reached at all with the other burner. This shift made a wider range of phase compositions available in both directions. If we assume that the 25% reduction in precursor concentration did not play a significant role here, the differing flow setup should be the reason for the discrepancy. The change in the experimental setup could lead to differences in the temperature field, which might be one of the key factors explaining the shift of the curve. Temperatures, in any case, are expected to decrease with  $\varphi$ , as the oxygen flow increases. Another difference separating this study from the previous one is the way  $\varphi$  was varied. The low  $\varphi$  range allowed it to be

controlled simply by adjusting the oxygen flows, whereas the hydrogen flow needed to be changed in order to reach higher equivalence ratios. It would be interesting to experiment if the curve remained identical, if the equivalence ratio was controlled by adjusting the hydrogen flow also with this burner.

Even though the phase composition does not seem to be very sensitive to how the total flow is divided between the two oxygen channels, some differences in the phase composition among the three atomization flows are observable. For the 65 slpm total flow, the phase ratio was roughly the same for all three atomization flows, but the difference grew as the total flow was lowered. For the 35 and 20 slpm total flows, the highest atomization flow resulted in the highest amount of hematite. If a linear fit was made separately for each atomization flow, the slope would decrease with a growing atomization flow. Therefore, the correlation between  $\varphi$  and the phase ratio was slightly stronger for lower atomization flows.

We were also interested in other properties of the produced particles, so let us next take a look at how the SSA correlates with the phase composition. Figure 3 presents the BET results from two perspectives. Figure 3A portrays SSA as a function of  $Q_{tot}$  for different atomization flows and Figure 3B as a function of  $Q_{at}$  for different total flows.

The BET results are not straightforward to interpret against the Rietveld results. The SSA values varied between 29 and 87  $m^2/g$ , which correspond to calculated average particle sizes of around 39 and 13 nm, respectively. The highest average SSA values were attained with the lowest total flow of 20 slpm. When  $Q_{tot}$  was increased to 35 slpm, the SSA dropped for every  $Q_{at}$ . We assume this to principally signal an increase in the residual particle volume. Simultaneously, a significant increase in the hematite fraction occurred. For the 10 slpm atomization flow, the SSA slightly decreases further with the raising of the secondary oxygen flow by 10 and 20 slpm, but much less dramatically compared to the first increment. However, for the highest total flow of 65 slpm, the SSA jumped up for all atomization flows. Since the hematite fraction grew continuously with increasing  $\varphi$ , SSA does not unequivocally correlate with it.

As Figure 3B exhibits, SSA values increased on average, when a larger portion of the total flow was shifted to the atomization channel. However, the 65 slpm total flow seems to be a special case also in this sense, since similarly to the hematite fraction, the SSA was practically independent of  $Q_{at}$ . For the two lower total flows, the higher hematite fraction correlated with a higher SSA.

Because the SSA strongly depends on particle morphology in addition to the size distribution, the BET results should be inspected in conjunction with TEM images. The particles could generally be divided into two modes: ultrafine primary particles (PP) and larger residual

particles (RP). The PP mode consisted of quite a narrow distribution of particles below 10 nm that covered most of the TEM sample areas, excluding the 65 slpm samples.

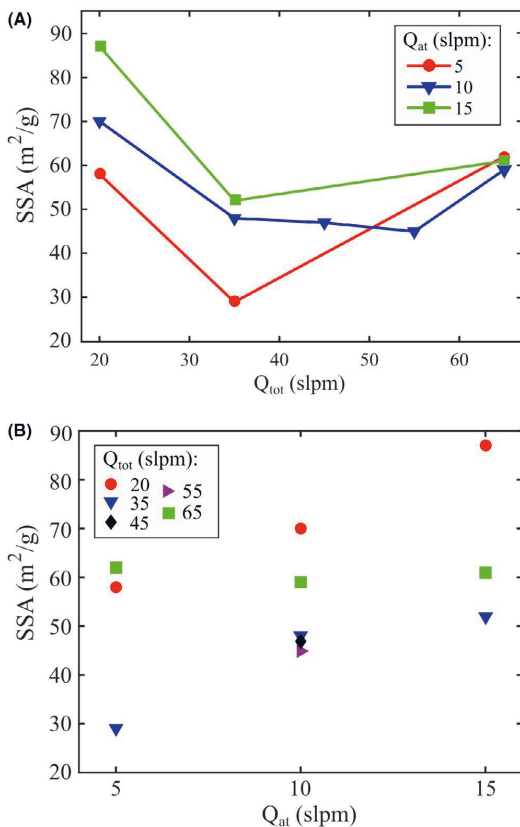


FIGURE 3 Specific surface areas as a function of (A)  $Q_{\text{tot}}$  and (B)  $Q_{\text{at}}$

Figure 4 shows TEM images of PPs from 20 slpm samples as a function of atomization flow. The average particle sizes were calculated by picking random areas dominated by the PP mode and measuring all discernible particles, amounting to a few hundred particles per sample. The average PP sizes were not calculated for other samples, since the individual particles became too difficult to distinguish, especially for higher total flows. Some examples of these are presented in Figure S5.

The PP size for 20 slpm samples ranged mostly from 3 to 7 nm. As the atomization flow increased, the particle size decreased. A somewhat similar trend was observed for 35 slpm samples, which implies that a higher atomization flow promotes a smaller PP size. This variation in the average PP size is probably one of the main factors explaining the differences in SSA between the different atomization flows, depicted in Figure 3B. However, all the calculated BET particle sizes are clearly greater than those calculated for the PP mode, so all samples most likely contain residual particles.

The RP mode should have a more pronounced effect on the SSA compared to the PP mode, since large particles raise it even in relatively small numbers. We assume increasing the total flow from 20 to 35 slpm caused an increase in the RP mode volume, thus lowering the SSA values, but for the higher total flows, the situation becomes trickier. As total flow increased to 45 and 55 slpm, the SSA values still decreased slightly, but with 65 slpm, they jumped up. The relatively high SSA of around  $60 \text{ m}^2/\text{g}$ , which applied to every 65 slpm sample, implies that most of the powder would consist of primary particles. However, all the TEM images point to a different direction, as the sample areas were dominated by residual particles. Figure 5 shows some TEM images of samples with 10 slpm atomization flow. More TEM images of 65 slpm samples are shown in Figure S6.

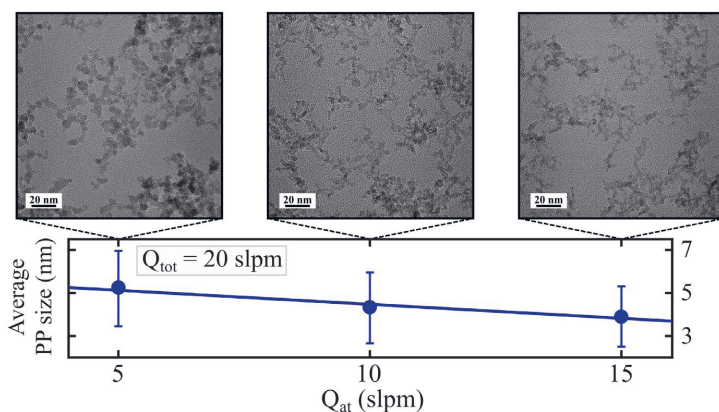


FIGURE 4 TEM images of primary particles from samples with total oxygen flow of 20 slpm. The average primary particles sizes were calculated arithmetically from a random area in the micrographs, and the error bars refer to standard deviations

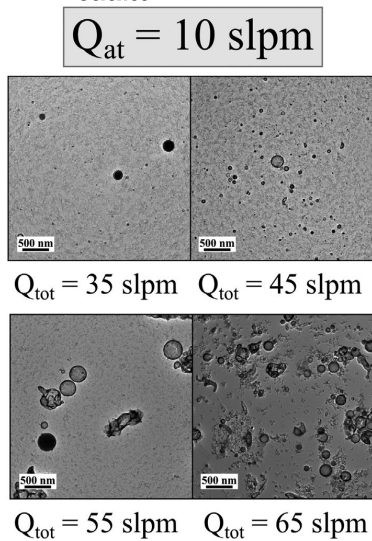


FIGURE 5 Transmission electron microscope images of residual particles in samples with 10 slpm atomization flow

It seems that as the total flow was raised, the number of irregularly shaped and hollow particles increased. Since hollow particles are often formed due to uneven evaporation, the temperature drop resulting from larger oxygen flow would understandably increase their number. For the 65 slpm samples, the PP mode seemed very scarce and hollow RPs dominated. We did not find many residual particles in the original 20 slpm TEM samples, but test samples heat-treated in 200 and 400°C revealed a RP mode with solid particles dominating (Figure S7). Presumably, the heat treatment should not have a great impact on the residual particle morphology. In other words, hollow particles remain hollow. We assume this increase of hollow particles to raise the SSA values, since hollow particles have a low effective density compared to solid particles. TEM imaging only covers a very small portion of the total sample volume, so this hypothesis cannot be completely verified. However, if this conclusion is correct, the hematite fraction could be more tightly linked to the number of hollow particles rather than residual particles, the PP mode consisting of primarily maghemite. This would also explain why no clear differences are observed between the widths of the XRD peaks corresponding to maghemite and hematite, because the shell of hollow particles could only contain relatively small crystallites.

To try to understand where the differences between the samples arise, we should examine the atomization and the flame structure. One of the main reasons for the discrepancies between the samples with the same total flow but

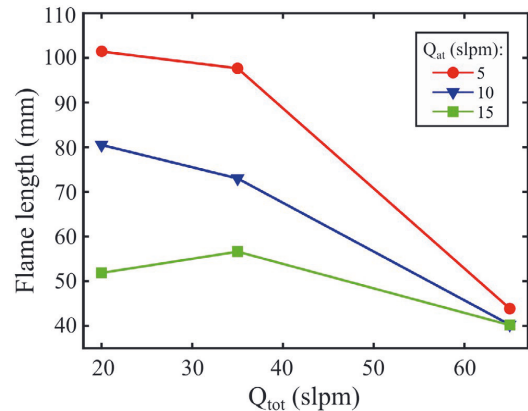


FIGURE 6 Flame length as a function of total flow for different atomization flows

differing atomization flows could emerge from the varying flame lengths. Even though the theoretical  $\phi$  was constant, the flame length did not correlate with it linearly, as has been stated for FSP by Mädler et al.<sup>25</sup> This relationship seems to be very dependent on the experimental setup. Figure 6 shows the measured flame lengths for the three total flow combinations.

For the highest total flow, the flames were very short for all cases, which was expected in very oxidic conditions. However, at lower total flows, the flame length became strongly dependent on the flow division. Growing atomization flow presumably increases turbulence in the flame zone, leading to flame contraction. The differences in average PP size observed between the different atomization flows probably stem from this phenomenon, since a shorter flame promotes a shorter residence time, and thus a lower PP size. Flame contraction also causes steeper temperature gradients compared to long flames. Short residence times and rapid quenching have been observed to be some of the governing factors in the phase formation of titanium oxide in FSP,<sup>26,27</sup> so they could promote hematite formation.

When estimating the residence time, the particle velocity also needs to be taken into account. We can use the atomization measurements to help examine the situation. Figure 7 shows the measured mean droplet velocities and diameters as a function of atomization flow for three different ethanol feed rates. The data point referring to droplet velocity at 1 ml/min feed rate and 3 slpm atomization flow was assumed to be a measurement error.

The droplet velocity behaved quite interestingly. With low atomization flows, the velocity increased as the flow was raised, but at around 6–7 slpm the velocity peaked, and the turbulence presumably started to take



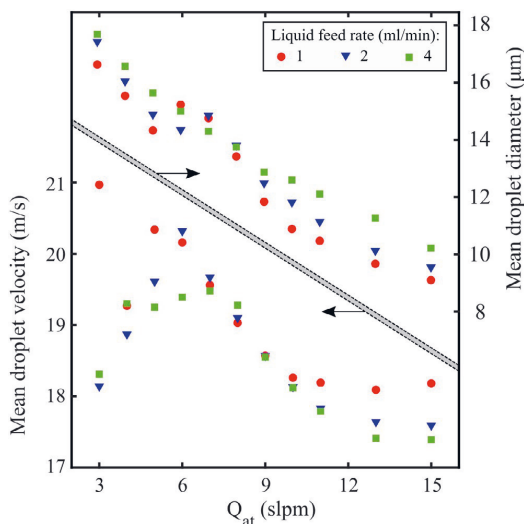


**FIGURE 7** Measured mean droplet diameter and velocity as a function of  $Q_{at}$  for three different feed rates of ethanol. The graph is divided into two parts referring to different y-axes

over. From there on, the velocity decreased quite linearly until 12–13 slpm. This means that even though the velocity of the gas emerging from the burner head theoretically grows when the atomization flow increases, the residence time of the particles in the flame does not necessarily drop as dramatically. This might allow most of the precursor still to evaporate and form nanoparticles with 15 slpm atomization flow, although the flame is very short.

As expected, the mean droplet size decreased with the increasing atomization flow. The data points for the highest atomization flows are most likely a bit overestimated due to the 4–5  $\mu\text{m}$  lower cut point of the instrument, since more sub-5  $\mu\text{m}$  particles are generated. The decrease in average droplet size also means that the residual particles with 15 slpm atomization flow are likely smaller on average compared to the lower flow rates, which should also contribute to their highest SSA values.

**TABLE 1** The additive-to-precursor ratios for mass ( $R_m$ ) and amount of substance ( $R_n$ ), the weight fractions of each phase, and SSA values for different samples with oxalic acid or citric acid as an additive.

Sample	$R_m$	$R_n$	Maghemite fraction (%)	Hematite fraction (%)	SSA ( $\text{m}^2/\text{g}$ )
Only MeOH	0	0	57.7	42.3	48
OxA 1	0.12	0.55	76.2	23.8	29
OxA 2	0.46	2.05	95.5	4.5	25
CitA 1	0.15	0.30	93.5	6.5	51
CitA 2	0.30	0.58	99.3	0.7	55
CitA 3	1.00	1.92	99.5	0.5	55

### 3.2 | Addition of citric acid and oxalic acid

The effect of citric acid and oxalic acid as additives was studied by dissolving various amounts of them in the precursor solution, while keeping other parameters fixed. The “middle point” parameters of 10 slpm atomizing flow and 35 slpm total flow were chosen for all the samples. The additive-to-precursor ratios with respect to mass ( $R_m$ ) and amount of substance ( $R_n$ ) for different samples are presented in Table 1 with the calculated phase compositions and measured SSA values. Figure 8 shows the XRD patterns of the different samples with the most important peaks referring to maghemite ( $\gamma$ ) and hematite ( $\alpha$ ) marked. The Rietveld plots and refinement parameters are presented in Figures S8 and S9 and Table S2.

Both additives dramatically decreased the amount of hematite that was otherwise formed. CitA was clearly the more efficient of the two additives in this respect, since 30% of the mass (around 60% of the amount of substance) of iron nitrate was adequate to eliminate basically the whole hematite phase, and already half of that amount erased most of it. Since no samples with lower amounts of CitA were prepared, we do not know how very small additions would behave. Much more OxA was required to eliminate the hematite phase, and even double the amount of substance compared to iron nitrate still left a noticeable (although barely) fraction in the sample. However, we are not aware whether a further increase in the amount of OxA would yield the same result as a lower amount of CitA. This difference could maybe be explained by inspecting the two molecules. CitA, having three carboxyl groups instead of two, and an additional OH group, would be assumed to have increased steric hindrance and be more prone to forming complexes than OxA. Therefore, a lower amount could provide the same effect.

The SSA results make an interesting distinction between the two additives. While the CitA addition, with all tested amounts, slightly increased the SSA, OxA addition dropped it to almost half of the additive-free precursor solution. There were no clearly observable differences in the PP size (shown in Figure S10), so the difference

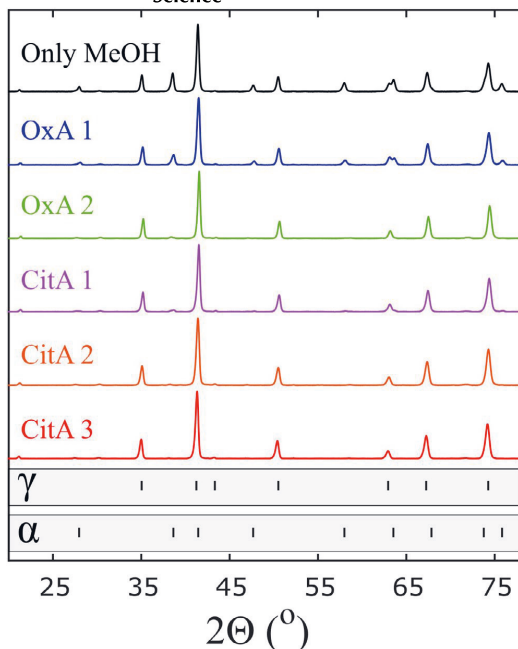


FIGURE 8 The XRD patterns of samples with the added oxalic acid or citric acid in the precursor solution. The growing number in the sample names refer to increasing amount of the additive. The main peaks of maghemite ( $\gamma$ ) and hematite ( $\alpha$ ) are marked on the bottom

most likely comes from larger particles. One possibility is that there are more hollow residual particles in the sample without additives, and the OxA addition reduces their number, simultaneously increasing the number of solid residual particles. Another possibility could be an additional mid-sized particle mode that seemed to be especially prevalent in the OxA 2 sample (Figure S11). The TEM sample showed an evenly spread collection of nanoparticles in the size range of about 10–50 nm. The origin of these particles is unknown, but they could explain the drop in SSA. The different types of intermediate complexes formed by the two additives could also have an effect here.

The results for CitA and OxA cannot be directly compared to the results for carboxylic acid addition in the previous study,<sup>15</sup> because the experimental setup was different, and the precursor concentration a little bit higher. What makes the two situations somewhat comparable, though, is that the chosen parameters with pure methanol as the solvent produced very similar phase compositions in both cases (42.3% vs 44.6% of hematite). Already the lowest amount (5 vol-% of the solvent mixture) of added 2-ethyl hexanoic acid (EHA), which translates to  $R_m$  and  $R_n$  values of 0.13 and 0.36, caused a complete elimination

of hematite. A further EHA addition seemed to reduce the RP mode, possibly due to the raised heat of combustion (HOC) of the precursor solution. EHA, as a solvent that has a significantly higher HOC than methanol, is a different type of additive compared to CitA and OxA that need to be dissolved and have lower HOC values per volume than methanol. The EHA substitution changed the particle distribution when increased in volume, while increasing the amount of CitA seemed to only have a very slight effect. Also, CitA can only be dissolved in limited amounts. On the positive side, it is quite a safe and readily accessible chemical, so it could be useful, if another way to eliminate residual particles would be discovered.

We are not aware of other flame synthesis studies performed with similar precursor solutions to ours, but there are some studies conducted with different synthesis methods from iron citrate, and also with CitA and OxA added to an iron precursor. In a reasonably low temperature (max 250°C) sol-gel synthesis, pure maghemite was obtained, when FeN-CitA mixture was used as the precursor.<sup>28</sup> A heat treatment of iron citrate at 500°C also resulted in pure maghemite.<sup>29</sup> The two studies that reported synthesis of pure hematite from FeN-CitA mixture, both had a calcination period of 4–6 h at 600°C in the end.<sup>30,31</sup> Since they performed no analyses before the calcination, we cannot be certain what kind of a phase composition was formed before it. Maghemite has been observed to transform into hematite at around 600°C.<sup>32</sup> Based on this literature, maghemite would likely be the more expected phase to be obtained with CitA, since LFS synthesis happens in a very short time period. However, chemical processes at high temperatures and short times are difficult to predict.

The results with OxA were more unexpected, because the literature we found on syntheses utilizing it resulted in hematite particles. Sol-gel and thermal decomposition syntheses from FeN-OxA mixtures have been performed at 400°C, resulting in pure hematite.<sup>33,34</sup> A chemical synthesis at 250–450°C from a FeN-OxA mixtures,<sup>35</sup> and thermolysis at 155°C,<sup>36</sup> both also resulted in pure hematite. These studies did not involve a calcination period at a high temperature, so a transformation from maghemite to hematite was very unlikely. Considering this literature, hematite would have been the more expected phase. The short times at high temperatures in flame synthesis, however, seem to change the process to yield mostly maghemite.

## 4 | CONCLUSIONS

We studied the underlying factors that determine the phase formation of iron oxide particles produced from iron nitrate in LFS synthesis. We continued from our previous paper<sup>15</sup> where another burner was used. The

previously used burner with a single oxygen flow and a single hydrogen flow was replaced with another burner that enabled adding a secondary oxygen flow between the atomizing flow and the hydrogen flow. This allowed us to explore how the process behaves in extremely low equivalence ratios (0.10–0.33), compared to what we studied before (0.32–1.76). We also studied how dividing the total oxygen flow differently between the two gas channels affected the iron oxide particles, when the equivalence ratio remained constant. The second part of the study focused on the effect of adding citric acid or oxalic acid to the precursor solution, while other parameters were kept constant. Phase control of iron oxide has previously been studied for at least atmospheric chemical vapor synthesis,<sup>37</sup> and FSP synthesis in a controlled atmosphere,<sup>38,39</sup> where the burner is in a somehow enclosed space, but not in an open flame synthesis process. The effect of using different precursor-solvent combinations on the phase composition of  $\text{Li}_4\text{Ti}_5\text{O}_{12}$  in FSP synthesis has been studied.<sup>40</sup> Also, EHA has earlier been added to iron nitrate solution,<sup>41</sup> but not from the perspective of the phase composition.

All sample powders consisted of maghemite or a mixture of maghemite and hematite. The maghemite fraction correlated quite linearly with the equivalence ratio through the whole range, varying from around 14% to 100%. In the previous study, the maghemite fraction saturated at around 90% when  $\varphi$  was raised. The curve was also clearly shifted toward lower  $\varphi$  values compared to the results with the other burner. The equivalence ratio of ca. 0.32 that earlier resulted in roughly 50/50 phase ratio produced even pure maghemite. This indicates that the correlation between  $\varphi$  and the maghemite fraction is strongly dependent on the experimental setup. The specific surface area did not correlate with  $\varphi$  in a simple manner. The highest SSA values were obtained with the lowest  $\varphi$ , then decreasing, but jumping up for the highest  $\varphi$ . This phenomenon might have been connected to the residual particle morphology. The number of hollow particles seemed to increase with  $\varphi$ , which would explain relatively high SSA values for the largest total oxygen flow.

Some variation was observed between the samples with a constant equivalence ratio but differing oxygen flow division. A larger atomization flow promoted a higher hematite fraction and SSA. The higher SSA was likely connected to the decreasing primary particle size and the higher hematite fraction possibly to flame contraction. However,  $\varphi$  was still the main factor determining the phase composition.

Adding both oxalic acid and citric acid lowered the hematite fraction in the samples. Citric acid was more efficient than the two, requiring a smaller amount to produce

pure maghemite. Oxalic acid addition significantly lowered the SSA compared to a pure methanol sample, whereas citric acid slightly increased it. The lowering of the SSA for oxalic acid was possibly due to the formation of a mid-sized particle mode in the size range of 10–50 nm.

We believe that this study provided valuable knowledge on the factors that govern phase formation of iron oxide particles in FSP synthesis, but a lot more research is needed to fully grasp the whole process. Especially, the nucleation mechanisms of different phases and the way the precursor chemistry affects the process remain far from complete understanding.

## ACKNOWLEDGEMENTS

M. Sorvali wants to acknowledge the TUT graduate school for financial support. This work made use of Tampere Microscopy Center facilities at Tampere University.

## ORCID

Miika Sorvali  <https://orcid.org/0000-0003-2697-4922>

## REFERENCES

- Gupta AK, Gupta M. Synthesis and surface engineering of iron oxide nanoparticles for biomedical applications. *Biomaterials*. 2005;26:3995–4021.
- Usov NA. Iron oxide nanoparticles for magnetic hyperthermia. *SPIN*. 2019;9(2):1940001.
- Jönkkäri I, Sorvali M, Huhtinen H, Sarlin E, Salminen T, Haapanen J, et al. Characterization of bidisperse magnetorheological fluids utilizing maghemite ( $\gamma\text{-Fe}_2\text{O}_3$ ) nanoparticles by flame spray pyrolysis. *Smart Mater Struct*. 2017;26(6):095004.
- Kciuk M, Turczyn R. Properties and application of magnetorheological fluids. *JAMME*. 2006;18(1–2):127–30.
- Laurent S, Forge D, Port M, Roch A, Robic C, Elst LV, et al. Magnetic iron oxide nanoparticles: synthesis, stabilization, vectorization, physicochemical characterizations, and biological applications. *Chem Rev*. 2008;108:2064–110.
- Nosrati H, Salehiabar M, Fridoni M, Abdollahifar M-A, Manjili HK, Davaran S, et al. New insight about biocompatibility and biodegradability of iron oxide magnetic nanoparticles: stereological and in vivo MRI monitor. *Sci Rep*. 2019;9:7173.
- Dutt M, Ratan A, Tomar M, Gupta V, Singh V. Mesoporous metal oxide- $\alpha\text{-Fe}_2\text{O}_3$  nanocomposites for sensing formaldehyde and ethanol at room temperature. *J Phys Chem Solids*. 2020;145:109536.
- Wei Q, Sun J, Song P, Yang Z, Wang Q. Metal-organic frameworks-derived porous  $\alpha\text{-Fe}_2\text{O}_3$  spindles decorated with Au nanoparticles for enhanced triethylamine gas-sensing performance. *J Alloy Compd*. 2020;831:154788.
- Tamirat AG, Rick J, Bubale AA, Su W-N, Hwang B-J. Using hematite for photoelectrochemical water splitting: a review of current progress and challenges. *Nanoscale Horiz*. 2016;1:243–67.
- Li S, Hu S, Xu K, Jiang W, Hu J, Liu J. Excellent visible-light photocatalytic activity of p-type  $\text{Ag}_2\text{O}$  coated n-type  $\text{Fe}_2\text{O}_3$  microspheres. *Mater Lett*. 2017;188:368–71.

11. Zhu J, Lu Y, Chen C, Ge Y, Jasper S, Leary JD, et al. Porous one-dimensional carbon/iron oxide composite for rechargeable lithium-ion batteries with high and stable capacity. *J Alloy Compd.* 2016;672:79–85.
12. Narsimulu D, Nagaraju G, Sekhar SC, Ramulu B, Hussain SK, Yu JS. Unveiling multi-channelled 3D porous iron oxide nanostructures with exalted capacity towards high-performance Li-ion battery applications. *J Alloy Compd.* 2020;846:156385.
13. Brázda P, Kohout J, Bezdička P, Kmječ T.  $\alpha$ -Fe<sub>2</sub>O<sub>3</sub> versus  $\beta$ -Fe<sub>2</sub>O<sub>3</sub>: controlling the phase of the transformation product of  $\epsilon$ -Fe<sub>2</sub>O<sub>3</sub> in the Fe<sub>2</sub>O<sub>3</sub>/SiO<sub>2</sub> system. *Cryst Growth Des.* 2014;14:1039–46.
14. Sakurai S, Namai A, Hashimoto K, Ohkoshi S. First observation of phase transformation of all four Fe<sub>2</sub>O<sub>3</sub> phases ( $\gamma \rightarrow \epsilon \rightarrow \beta \rightarrow \alpha$ -Phase). *J Am Chem Soc.* 2009;131:18299–303.
15. Sorvali M, Nikka M, Juuti P, Honkanen M, Salminen T, Hyvärinen L, et al. Controlling the phase of iron oxide nanoparticles fabricated from iron(III) nitrate by liquid flame spray. *Int J Ceramic Eng Sci.* 2019;1:194–205.
16. Aromaa M, Keskinen H, Mäkelä JM. The effect of process parameters on the Liquid Flame Spray generated titania nanoparticles. *Biomol Eng.* 2007;24:543–8.
17. Mäkelä JM, Keskinen H, Forsblom T, Keskinen J. Generation of metal and metal oxide nanoparticles by liquid flame spray process. *J Mater Sci.* 2004;39:2783–8.
18. Mäkelä JM, Haapanen J, Harra J, Juuti P, Kujanpää S. Liquid Flame Spray – A Hydrogen-Oxygen Flame Based Method For Nanoparticle Synthesis And Functional Nanocoatings. *KONA Powder Part J.* 2017;34:141–54.
19. Brobby KJ, Haapanen J, Tuominen M, Mäkelä J, Gunell M, Eerola E, et al. High-speed production of antibacterial fabrics using liquid flame spray. *Text Res J.* 2019;90(5–6):503–11.
20. Brobby KJ, Haapanen J, Mäkelä JM, Gunell M, Eerola E, Rosqvist E, et al. Effect of plasma coating on antibacterial activity of silver nanoparticles. *Thin Solid Films.* 2019;672:75–82.
21. Juuti P, Nikka M, Gunell M, Eerola E, Saarinen JJ, Omori Y, et al. Fabrication of fiber filters with antibacterial properties for VOC and particle removal. *Aerosol Air Qual Res.* 2019;19:1892–9.
22. Temerov F, Pham K, Juuti P, Mäkelä JM, Grachova EV, Kumar S, et al. Silver-decorated TiO<sub>2</sub> inverse opal structure for visible light-induced photocatalytic degradation of organic pollutants and hydrogen evolution. *ACS Appl Mater Interfaces.* 2020;12:41200–10.
23. Koivuluoto H, Matikainen V, Larjo J, Vuoristo P. Novel on-line diagnostic analysis for in-flight particle properties in cold spraying. *J Therm Spray Technol.* 2018;27:423–32.
24. Fischer RX, Messner T, Kassner D. BRASS 2003: the Bremen rietveld analysis and structure suite. *Z Kristallogr.* 2006;15(1).
25. Mädler L, Stark WJ, Pratsinis SE. Flame-made ceria nanoparticles. *J Mater Res.* 2002;17(6):1356–62.
26. Manuputty MY, Dreyer JAH, Sheng Y, Bringley EJ, Botero ML, Akroyd J, et al. Polymorphism of nanocrystalline TiO<sub>2</sub> prepared in a stagnation flame: formation of the TiO<sub>2</sub>-II phase. *Chem Sci.* 2019;10:1342–50.
27. Riad KB, Wood-Adams PM, Wegner K. Flame-made TiO<sub>2</sub>(B). *Mater Res Bull.* 2018;106:276–81.
28. Kotsyubynsky V, Ostafiychuk B, Moklyak V, Hrubiak A. Synthesis, characterization and electrochemical properties of mesoporous maghemite  $\gamma$ -Fe<sub>2</sub>O<sub>3</sub>. *Sol St Phen.* 2015;230:120–6.
29. Mou F, Guan J-G, Shi W, Sun Z, Wang S. Oriented contraction: a facile nonequilibrium heat-treatment approach for fabrication of maghemite fiber-in-tube and tube-in-tube nanostructures. *Langmuir.* 2010;26(19):15580–5.
30. Habibi MH, Kiani N. Preparation of single-phase  $\alpha$ -Fe(III) oxide nanoparticles by thermal decomposition. Influence of the precursor on properties. *J Therm Anal Calorim.* 2013;112:573–7.
31. Nandi AK, Pant A, Tripathi A, Newale SP, Gajbhiye VP, Jadhav AJ, et al. Large scale synthesis and characterization of  $\alpha$  Fe<sub>2</sub>O<sub>3</sub> nanoparticles for propellant applications. *Proc of ICANMEET-2013.* 2013:475–80.
32. Khan US, Amanullah, Manan A, Khan N, Mahmood A, Rahim A. Transformation mechanism of magnetite nanoparticles. *Mater Sci-Poland.* 2015;33(2):278–85.
33. Ba-Abbad MM, Takriff MS, Benamor A, Mohammad AW. Size and shape controlled of  $\alpha$ -Fe<sub>2</sub>O<sub>3</sub> nanoparticles prepared via sol-gel technique and their photocatalytic activity. *J Sol-Gel Sci Technol.* 2017;81:880–93.
34. Muruganandham M, Amutha R, Sathish M, Singh TS, Suri RPS, Sillanpää M. Facile fabrication of hierarchical  $\alpha$ -Fe<sub>2</sub>O<sub>3</sub>: self-assembly and its magnetic and electrochemical properties. *J Phys Chem C.* 2011;115:18164–73.
35. Pant P, Naik BD, Ghosh NN. Synthesis of  $\alpha$ -Fe<sub>2</sub>O<sub>3</sub> nano powder by simple chemical method. *Mater Technol.* 2009;24(4):213–6.
36. Yatsenko DA, Pakharukova VP, Tsybulya SV, Matvienko AA, Sidel'nikov AA. Phase composition and structure of nanocrystalline products of solid-phase oxidative thermolysis of iron oxalate dihydrate. *J Struct Chem.* 2012;53(3):548–56.
37. Ruusunen J, Ihalainen M, Koponen T, Torvela T, Tenho M, Salonen J, et al. Controlled oxidation of iron nanoparticles in chemical vapour synthesis. *J Nanopart Res.* 2014;15:2270.
38. Strobel R, Pratsinis SE. Direct synthesis of maghemite, magnetite and wustite nanoparticles by flame spray pyrolysis. *Adv Powder Tech.* 2009;20:190–4.
39. Kumfer BM, Shinoda K, Jeyadevan B, Kennedy IM. Gas-phase flame synthesis and properties of magnetic iron oxide nanoparticles with reduced oxidation state. *J Aerosol Sci.* 2010;41:257–65.
40. Meierhofer F, Li H, Gockeln M, Kun R, Grieb T, Rosenauer A, et al. Screening precursor-solvent combinations for Li<sub>4</sub>Ti<sub>5</sub>O<sub>12</sub> energy storage material using flame spray pyrolysis. *ACS Appl Mater Interfaces.* 2017;9:37760–77.
41. Rosebrock CD, Wriedt T, Mädler L, Wegner K. The role of microexplosions in flame spray synthesis for homogeneous nanopowders from low-cost metal precursors. *AIChE J.* 2016;62(2):381–91.

## SUPPORTING INFORMATION

Additional supporting information may be found online in the Supporting Information section.

**How to cite this article:** Sorvali M, Honkanen M, Hyvärinen L, Kuisma R, Larjo J, Mäkelä JM. Crystallographic phase formation of iron oxide particles produced from iron nitrate by liquid flame spray with a dual oxygen flow. *Int J Ceramic Eng Sci.* 2021;00:1–10. <https://doi.org/10.1002/ces2.10102>

# PUBLICATION

## III

**Characterization of bidisperse magnetorheological fluids utilizing maghemite ( $\gamma\text{-Fe}_2\text{O}_3$ ) nanoparticles synthesized by flame spray pyrolysis**  
Jönkkäri, I., Sorvali, M., Huhtinen, H., Sarlin, E., Salminen, T., Haapanen, J.,  
Mäkelä, J. M. and Vuorinen, J.

*Smart Materials and Structures* 26.(2017), 095004

DOI: 10.1088/1361-665X/aa7f7d

**Publication reprinted with the permission of the copyright holders**



# Characterization of bidisperse magnetorheological fluids utilizing maghemite ( $\gamma\text{-Fe}_2\text{O}_3$ ) nanoparticles synthesized by flame spray pyrolysis

I Jönkkäri<sup>1</sup>, M Sorvali<sup>2</sup>, H Huhtinen<sup>3</sup>, E Sarlin<sup>1</sup>, T Salminen<sup>4</sup>, J Haapanen<sup>2</sup>, J M Mäkelä<sup>2</sup> and J Vuorinen<sup>1</sup>

<sup>1</sup>Laboratory of Materials Science, Tampere University of Technology, PO Box 589, FI-33101 Tampere, Finland

<sup>2</sup>Aerosol Physics Laboratory, Laboratory of Physics, Tampere University of Technology, PO Box 692, FI-33101 Tampere, Finland

<sup>3</sup>Wihuri Physical Laboratory, Department of Physics and Astronomy, University of Turku, FI-20014 Turku, Finland

<sup>4</sup>Optoelectronics Research Centre, Tampere University of Technology, FI-33720 Tampere, Finland

E-mail: [ilari.jonkkari@tut.fi](mailto:ilari.jonkkari@tut.fi)

Received 21 April 2017, revised 19 June 2017

Accepted for publication 13 July 2017

Published 9 August 2017



CrossMark

## Abstract

In this study we have used liquid flame spray (LFS) process to synthesize  $\gamma\text{-Fe}_2\text{O}_3$  nanoparticles of two different average sizes. Different sized nanoparticles were generated with two different liquid precursor feed rates in the spray process, higher feed rate resulting in larger nanoparticles with higher saturation magnetization. The nanoparticles were used in bidisperse magnetorheological fluids to substitute 5% of the micron sized carbonyl iron particles. To our knowledge this is the first time particles synthesized by the LFS method have been used in magnetorheological fluids. The bidisperse fluids showed significantly improved sedimentation stability compared to a monodisperse suspension with the same solid concentration. The tradeoff was an increased viscosity without magnetic field. The effect of the nanoparticles on the rheological properties under external magnetic field was modest. Finally, the dynamic oscillatory testing was used to evaluate the structural changes in the fluids under magnetic field. The addition of nanoparticles decreased the elastic portion of the deformation and increased the viscous portion.

Keywords: magnetorheology, maghemite, bidisperse, flame spray pyrolysis, nanoparticle, sedimentation

(Some figures may appear in colour only in the online journal)

## 1. Introduction

Magnetorheological (MR) fluids are so-called smart materials that change their properties by external stimuli. With MR fluids the stimulus is an external magnetic field that induces a reversible transition from liquid- to solid-like behavior. The MR fluids are generally composed of spherical magnetic particles that are suspended in non-magnetic carrier fluid.

When the MR fluid is exposed to an external magnetic field, the particles form columnar structures in the direction of the field lines that resist the flow [1–3]. Since the carrier fluid and the particles have a large density mismatch, the particles tend to descend in the fluid over time. This sedimentation is problematic, since it can reduce the MR response, that is the change in rheological properties by magnetic field, or even prevent it completely. The redispersion of the particles may

also be difficult after sedimentation if they form a hard cake at the bottom. There are several ways how the sedimentation may be hindered. A conventional way is the usage of surfactants and thixotropic agents. Thixotropic agents function by forming structures in the carrier fluid at small shear rates that increase fluids viscosity and slow down the sedimentation. The structures break down when the shear rate increases. The surfactants function by steric repulsion. They are typically short molecule chains that can adhere on the particle surface from one end while the other is stretching out and preventing a direct contact with neighboring particles [4]. A more recent approach to reduce sedimentation is the usage of nanoparticles.

Suspensions that contain only well dispersed nanoparticles do not settle at all; thermal convection in the fluid creates thermodynamic forces that counteract gravitational forces causing the sedimentation. Ferrofluids that contain magnetic nanoparticles, surfactant and carrier fluid are stable against agglomeration and sedimentation, but have significantly lower MR response than conventional MR fluids with micron-sized particles [2, 5]. It has been shown in number of studies that addition of a low amount of nanoparticles with larger particles may reduce the sedimentation rate of the whole suspension without sacrificing the MR response [5–13]. When the nanoparticle concentration is kept small, the MR response remains at a satisfactory level or may even improve [6–9]. The nanoparticles in these so-called bidisperse fluids have most often been magnetite ( $\text{Fe}_3\text{O}_4$ ) due to its availability, well known synthetization and magnetic properties [5, 10–13]. Another magnetic iron oxide is the maghemite ( $\gamma\text{-Fe}_2\text{O}_3$ ) which has quite similar magnetic properties to  $\text{Fe}_3\text{O}_4$ . Both have an inverse spinel structure, but  $\gamma\text{-Fe}_2\text{O}_3$  has only  $\text{Fe}^{3+}$  iron cations whereas  $\text{Fe}_3\text{O}_4$  has both  $\text{Fe}^{3+}$  and  $\text{Fe}^{2+}$ . Also,  $\gamma\text{-Fe}_2\text{O}_3$  has a better chemical stability than  $\text{Fe}_3\text{O}_4$  and is more versatile as the particle morphologies may vary from spheres to ellipsoids over a wide size range from 2 to 1000 nm depending on how the particle is synthesized [14].

In the literature several synthetization routes both in liquid and gas phase have been presented. Thermal aerosol techniques offer a potential to generate spherical nanoparticles via a dry industrial process [15] and especially flame methods are considered optional for up-scaling [16]. The particles synthesized with these techniques tend to form aggregates, which are primary particles fused together with strong chemical or sintering forces [17]. In flame spray pyrolysis (FSP) liquid precursors are sprayed into the flame. In a specific FSP-method, liquid flame spray (LFS), hydrogen and oxygen act as atomizing and combustion gases [18]. Major advantage of the LFS process is the broad spectrum of metal or metal oxide nanoparticles, which can be created using different liquid precursors. The method is suitable for one- or multi-component nanoparticle synthesis [19]. Injected metal salt or organometallic precursor evaporates in the flame: the evaporated precursor molecules can react chemically or decompose thermally, then nucleate and re-condense in nanoparticle form of the final material [20].

In the present study we use  $\gamma\text{-Fe}_2\text{O}_3$  nanoparticles, synthesized by LFS process, together with micron-sized carbonyl iron (CI) particles to prepare bidisperse MR fluids with improved sedimentation stability. The nanoparticles were characterized by transmission electron microscopy (TEM), x-ray diffraction (XRD), Raman spectroscopy and SQUID magnetometry. The sedimentation stability of the MR fluids was studied by optical tracking of the interface between the clear carrier fluid and the particle suspension that formed in the fluids over time. The rheological characteristics of the fluids were examined with (on-state) and without magnetic field (off-state) via rotational rheometer.

## 2. Experimental

### 2.1. Materials

Three MR fluids were prepared with a total particle volume concentration  $\phi$  of 0.15. One MR fluid was monodisperse containing only micron-sized CI particles (BASF, HQ) while in the others 5% of the total particle concentration was substituted with  $\gamma\text{-Fe}_2\text{O}_3$  particles. The fraction of the nanoparticles was kept low since the fluids became too thick with higher concentrations. The substitution was done based on the volume fractions since the magnitude of the magnetorheological effect depends on the volume concentration of the magnetic particles [21]. Rhodorsil 47 v 50 silicone oil was used in all MR fluids as the carrier fluid. It has a viscosity of  $48 \pm 2.4$  mPa s and a density of  $0.96$  g cm<sup>-3</sup>. Two weight percent of lecithin was added to all MR fluids, since the magnetic nanoparticles need stabilization against agglomeration, as they possess a permanent magnetic moment. The lecithin has been used as a surfactant to improve dispersion stability of similar type of magnetic nanoparticles in silicone oil before [7]. The lecithin was added also into the MR fluid without nanoparticles to make sure that it is not causing the differences in sedimentation behavior and rheological properties between mono- and bidisperse fluids.

### 2.2. Synthetization of $\gamma\text{-Fe}_2\text{O}_3$ nanoparticles

The  $\gamma\text{-Fe}_2\text{O}_3$  nanoparticles were synthesized by LFS-method where hydrogen and oxygen act as atomizing and combustion gases. Gas flow rates in the flame for hydrogen and oxygen were  $40$  l min<sup>-1</sup> and  $20$  l min<sup>-1</sup>, respectively. The precursor for the  $\text{Fe}_2\text{O}_3$  was ferrocene ( $\text{Fe}(\text{C}_5\text{H}_5)_2$ , Alfa Aesar 99%) dissolved in xylene (VWR, technical grade), with metallic concentration of 29 mg(Fe)/ml. Ferrocene was chosen as the precursor compound since it has relatively high volatility and therefore it is not expected to produce undesired hematite residual particles, which would decrease the magnetic properties of the iron oxide nanopowder. Precursor feed rates were 3.0 and 8.3 ml min<sup>-1</sup> for samples Nano1 and Nano2 respectively. The aerosol nanoparticles were collected from the gas flow by a simple planar electrostatic precipitator (ESP) placed downstream of the flame. In the ESP, there are two steel plates with a distance of approximately 60 mm and the



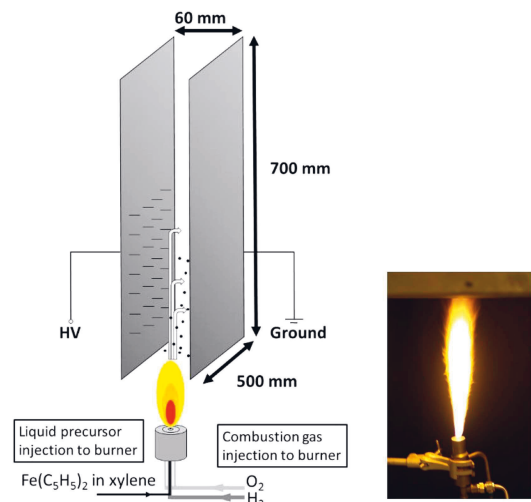


**Figure 1.** The LFS-process with ESP aerosol nanoparticle collector.

voltage between the plates is 20–30 kV. Distance between the burner and the plates was 380 mm. On the negative plate, there are corona needles to charge the particles. The collection plate is grounded. The LFS-process with ESP aerosol nanoparticle collector is illustrated in figure 1. The powder was finally gathered from the ESP collection plate using a special peeling tool, suitable for the nanoparticle collection. LFS-synthesized iron oxide nanoparticles are mainly in  $\gamma$ - $\text{Fe}_2\text{O}_3$  form [22].

### 2.3. Characterization of nanoparticles

TEM images of the nanoparticle were obtained to study the size, shape and agglomeration of the particles. The samples were prepared by mixing small fractions of nanoparticles with ethyl alcohol, pouring mixture on the TEM grid and letting the alcohol evaporate. The images were acquired using a JEOL JEM 2010 operating at accelerating voltage of 200 kV. The x-ray powder diffraction and Raman spectroscopy were used to study the composition of the iron oxides. The XRD measurements were done with Panalytical Empyrean Multipurpose Diffractometer using  $\text{Cu K}\alpha$  radiation ( $\lambda = 1.5405 \text{ \AA}$ ) and 45 kV and 40 mA cathode voltage and current, respectively. Raman spectra were measured with a Andor Shamrock 303 spectrometer and Andor Newton 940P cooled CCD detector. The wavelength of the excitation laser was 532 nm. Low laser power level was used to study iron oxides to avoid the heating of the sample that may cause structural phase conversions [23]. The magnetic measurements were made with a Quantum Design MPMS XL SQUID magnetometer. The virgin magnetizations as functions of the external magnetic field  $B$  and magnetic hysteresis curves at  $-2.5 \text{ T} \leq B \leq 2.5 \text{ T}$  were recorded at temperatures of 10 and 300 K.

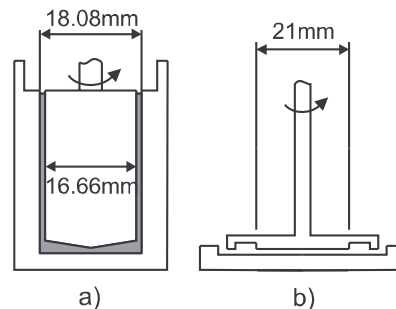


**Figure 2.** The concentric cylinder (a) and the plate–plate geometry (b) used to measure the off- and on-state properties, respectively.

### 2.4. Preparation of MR fluids

The MR fluids were prepared with a combination of sonication and mechanical mixing. Sonication was used since it has been proven to be an effective way to break down nanoparticle agglomerates, which are formed from the primary particles and aggregates by weak physical forces [24]. The aggregates generally have such strong bonds that they are not fragmented during sonication. Nanoparticles were first mixed with silicone oil and lecithin by the sonicator (Qsonica, Q700). The sonication was done in cycles where the suspension was sonicated for 10 s at 75% amplitude and then let rest for 30 s to avoid overheating. The total sonication time was 30 min. The mixing pot was cooled from outside with  $3^\circ\text{C}$  liquid circulation. After sonication, the CI particles were added to the suspension and mechanical mixing was maintained at 2000 rpm for 30 min.

### 2.5. Characterization of MR fluids

The rheological properties of the MR fluids were studied with Anton Paar MCR301 rotational rheometer. MR fluids are desired to have a low viscosity without magnetic field (off-state) and strong increase in rheological properties with the magnetic field (on-state) causing high relative change in the properties or high MR response. Therefore, the measurements were done in both the on- and the off-state.

The CC17 concentric cylinder geometry illustrated in figure 2(a) was used for the off-state measurements since it offers a good sensitivity when measuring low-viscosity fluids. The geometry consists of a rotating inner cylinder and a stationary outer cylinder leaving 0.71 mm wide annular gap between them where the sample is confined. The viscosity curves were measured with constant shear rate tests that had two phases: the shear rate was first increased logarithmically from  $0.01$  to  $1000 \text{ s}^{-1}$  (up curve) and then decreased back to  $0.01 \text{ s}^{-1}$  (down curve).

The on-state rheological properties were measured with MRD180/1T magneto-cell illustrated in figure 2(b). It applies 21 mm plate–plate geometry with a stationary bottom plate and a rotating top plate. Both plates were custom made from aluminum and had roughened surfaces to avoid wall slip which can cause error to the measured values [25]. The

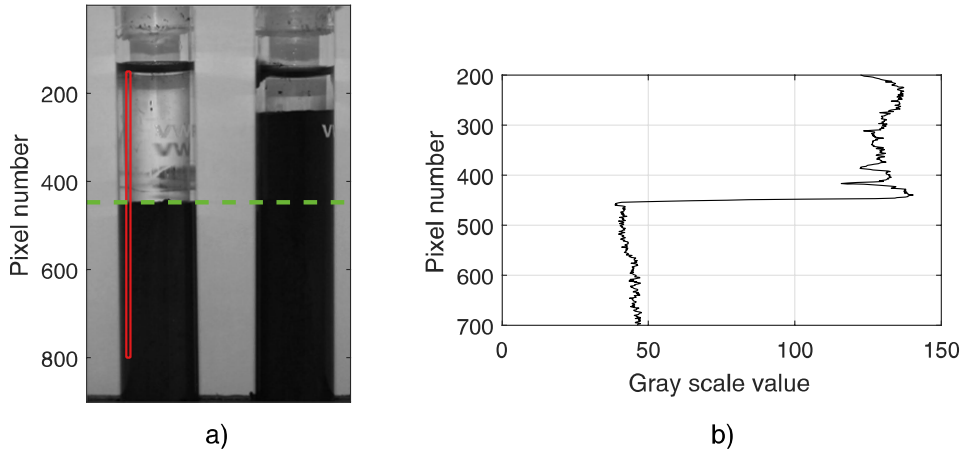


**Figure 3.** (a) A digital image of the test tubes where the scanned area is marked by a red box and the detected interface by a green dashed line. (b) The gradient in the grayscale values at the interface.

sample was confined in a 0.5 mm wide gap between the plates. The magneto-cell generates vertical and fairly uniform magnetic field that passes through the gap [25, 26]. The magnetic field strength was estimated by measuring the magnetic flux density from the channel underneath the bottom plate with a Hall probe. The temperature of the cell was held at 30 °C during the measurements with a circulating water bath. Two classes of on-state tests were done for the fluids: constant shear rate tests to determine the flow curves and oscillatory tests to study the viscoelastic characteristics and to evaluate the microstructure of the fluids. The flow curves were measured by increasing the shear rate logarithmically from 0.01 to 1000  $\text{l s}^{-1}$ . The dynamic yield stress was then evaluated from the flow curve by the Bingham model that was fitted to the data. The Bingham model is written as follows:

$$\tau_R = \tau_y + \eta_p \dot{\gamma}_R. \quad (1)$$

Here,  $\tau_y$  is the yield stress and  $\eta_p$  the plastic viscosity.

In the oscillatory tests the samples were subjected to sinusoidal oscillatory shear strain with a strain amplitude  $\gamma_0$  increasing from 0.01% to 100% at an angular frequency  $\omega$  of 1  $\text{rad s}^{-1}$ . In the linear viscoelastic regime, the resulting stress is also sinusoidal with amplitude  $\tau_0$  and phase shift  $\delta$ . The in-phase and out-of-phase components of the response are the storage modulus  $G'$  and the loss modulus  $G''$ :

$$G' = \frac{\tau_0}{\gamma_0} \cos \delta, \quad G'' = \frac{\tau_0}{\gamma_0} \sin \delta. \quad (2)$$

The moduli can be used to evaluate the microstructure of the MR fluid.

The sedimentation rate of the fluids was studied by optical tracking of the interface between the clear carrier fluid and the concentrated particle suspension that formed in the fluids over time after the mixing. The interface was tracked by using a house-built MATLAB<sup>®</sup> script to analyze digital images that were taken from the test tubes containing 5 ml of MR fluids every 60 min. The digital images were first converted to grayscale where each pixel gets a value from 0 to

255 depending on its intensity. The interface is seen numerically as a steep gradient in the grayscale values when the tube is scanned in vertical direction. The red box in the figure 3(a) shows the preselected area that was scanned by the Matlab script and the green dashed line the interface that was detected based on the gradient in the grayscale values shown in the figure 3(b). The interface position, which means the distance the interface has traveled from the top in millimeters, was then calculated based on the pixel numbers and known dimensions of the test tube.

### 3. Results and discussion

#### 3.1. Properties of the nanoparticles

The characterization was done for the nanoparticles after the synthesization without sonication or surface treatment. The size distribution and shape of the nanoparticles were studied from TEM images. The TEM images are shown in figure 4. The particle geometries were mostly spherical. The arithmetic average diameters for the Nano1 and Nano2 particles were 7.9 and 16.6 nm, respectively. The averages were determined by randomly measuring 200 particles from the images. The distribution of the particle diameters is shown in figure 5. The particle size distribution is located systematically at smaller diameters for Nano1. The images show that in both cases there are also particle aggregates, which is typical for nanoparticles produced by FSP methods [15].

The composition of the particles was studied with XRD and Raman spectroscopy. The XRD patterns of the particles are shown in figure 6. The diffraction peaks are wide as expected for nanoscale particles. The peak positions can be indexed with (111), (220), (311), (400), (422), (511) and (440) planes of the inverse spinel structure of  $\gamma\text{-Fe}_2\text{O}_3$ . The peak positions do not fit with crystallographic structure of the hematite ( $\alpha\text{-Fe}_2\text{O}_3$ ). The structures of the  $\gamma\text{-Fe}_2\text{O}_3$  and  $\text{Fe}_3\text{O}_4$

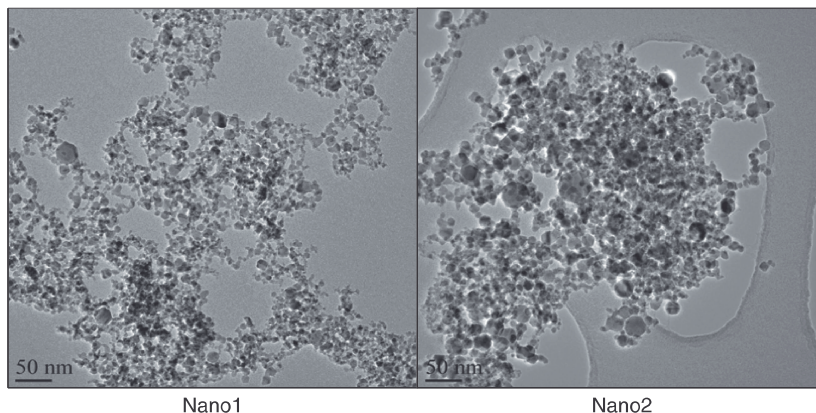


Figure 4. TEM images of Nano1 and 2 particles.

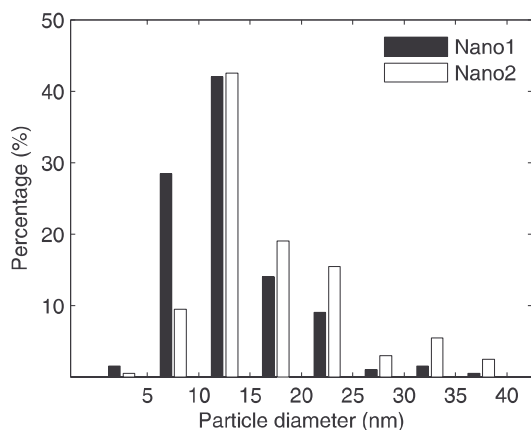


Figure 5. Distribution of the particle diameters of Nano1 and 2 particles.

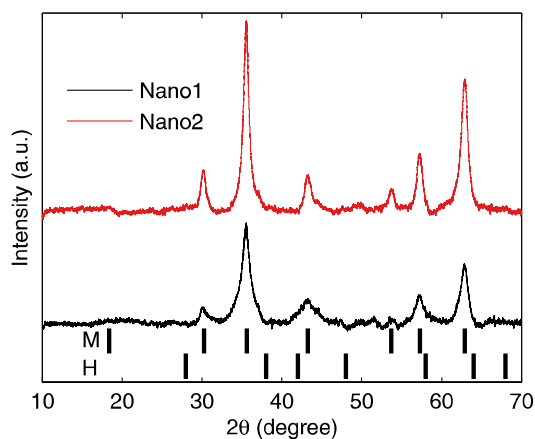


Figure 6. XRD patterns for the Nano1 and Nano2 particles. The peak positions for  $\gamma$ -Fe<sub>2</sub>O<sub>3</sub> (M) and  $\alpha$ -Fe<sub>2</sub>O<sub>3</sub> (H) are shown below the spectrum.

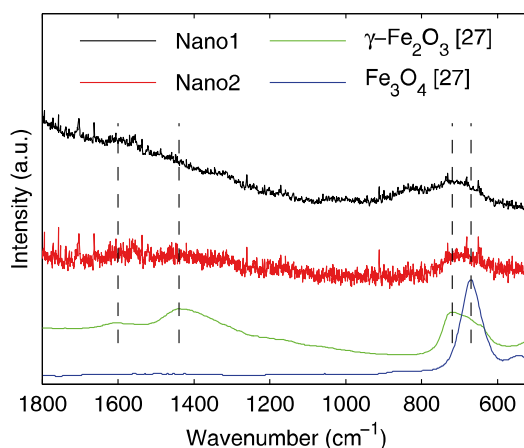
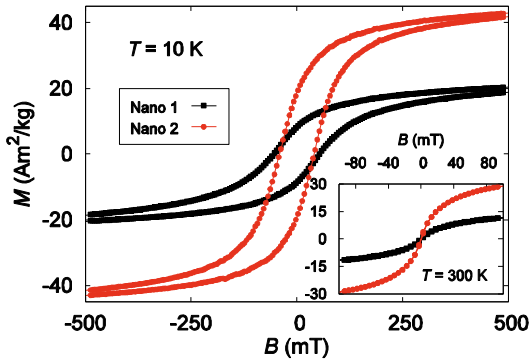


Figure 7. Raman spectrum for the Nano1 and Nano2 particles and the reference spectra for  $\gamma$ -Fe<sub>2</sub>O<sub>3</sub> and Fe<sub>3</sub>O<sub>4</sub> obtained from the research by Molchan *et al* [27].

are so similar to that they cannot be reliably distinguished based on the XRD data. Therefore, the composition of the particles was studied further by Raman spectroscopy. The Raman spectra of the Nano1 and Nano2 particles together with reference spectrum of the Fe<sub>3</sub>O<sub>4</sub> and  $\gamma$ -Fe<sub>2</sub>O<sub>3</sub> obtained from the research by Molchan *et al* [27] (reproduced by permission of The Royal Society of Chemistry) are shown in figure 7. Both samples gave low level of signal, meaning that the materials were poor Raman scatterers, and the signal-to-noise ratio was therefore low. The measured spectra have a slightly better fit on the spectrum of the  $\gamma$ -Fe<sub>2</sub>O<sub>3</sub>, especially around 700 cm<sup>-1</sup> where the strongest peaks exist. Based on the XRD patterns and Raman spectrum both nanoparticles samples are considered to be composed mainly of the  $\gamma$ -Fe<sub>2</sub>O<sub>3</sub>.

The magnetic hysteresis curves and virgin magnetizations at 10 and 300 K are shown in figures 8 and 9, respectively. At 10 K, the both Nano1 and Nano2 samples show a



**Figure 8.** The magnetic hysteresis loops of Nano1 and Nano2 samples measured at 10 K (main panel) and at 300 K (inset).

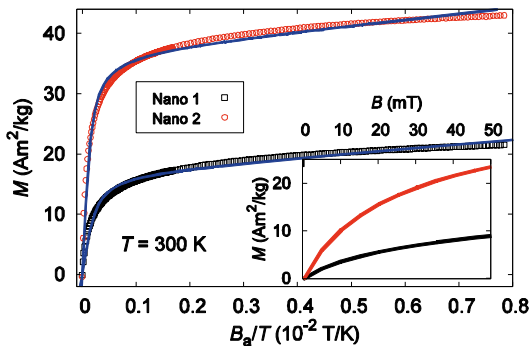


**Figure 9.** The magnetic virgin curves of Nano1 and Nano2 samples measured at 300 K. The blue solid curves in the main panel correspond to a fit to the Langevin function. The inset shows a closer look to the small magnetic field range up to 50 mT.

hysteretic behavior with relatively symmetric coercivity of 54 mT and 41 mT, respectively. At room temperature, the coercivity is zero, the remanent magnetization is lacking and the fit to the data of both samples is in good agreement with the Langevin function (main panel of figure 9), indicating a superparamagnetic behavior. The saturation magnetizations,  $M_S$ , at 300 K for the Nano1 and Nano2 are 22 and 43  $\text{Am}^2 \text{kg}^{-1}$ , respectively, being clearly lower than for bulk  $\gamma\text{-Fe}_2\text{O}_3$  of 74  $\text{Am}^2 \text{kg}^{-1}$  [14]. Similar results have been reported for iron nanoparticles earlier, e.g. Nurdin *et al* synthesized  $\gamma\text{-Fe}_2\text{O}_3$  nanoparticles by chemical co-precipitation method with saturation magnetization of 32  $\text{Am}^2 \text{kg}^{-1}$  at room temperature [28].

The size and the shape of a single particle should mainly effect the coercivity and remanent magnetization which are extrinsic magnetic properties [14].  $M_S$  is an intrinsic magnetic property, which depends mainly on the particles' composition and crystalline structure, but with nanoparticles it is also sensitive to the size. The surfaces of the nanoparticles have a thin layer where the electron spins and hence the magnetic moments are disordered, reducing the total  $M_S$ . The effect becomes stronger as the particle size decreases and the

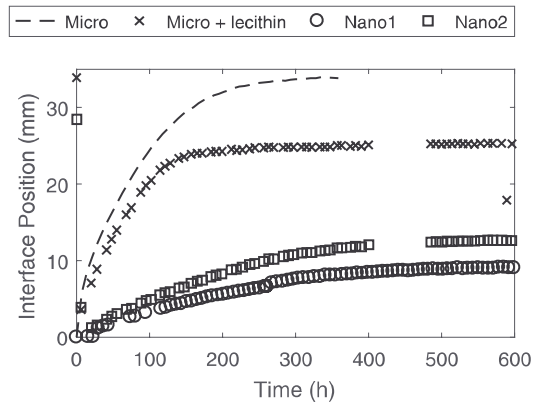


**Figure 10.** The sedimentation curves for the MR fluids. The curve for micro particles without lecithin is from our previous research [30].

portion of the disorder surface layer increases [29]. Since impurities was not detected in the compositional analysis of the particles it seems more plausible that the differences in magnetic properties of the Nano1 and Nano2 samples are mainly caused by the size related issues.

If the particle size distribution is assumed to be very narrow, the  $M(B_a/T)$  curves of superparamagnetic particles can be well fitted using a Langevin function:

$$M(B_a/T) = M_S * [\coth(uB_a/kT) - kT/uB_a], \quad (3)$$

where  $M_S$  is the saturation magnetization at 300 K,  $k$  is Boltzmann constant,  $u$  is the average magnetic moment of the particle,  $T$  is the temperature and  $B_a$  is applied magnetic field. From the magnetization data and the fit to the Langevin function, we can now calculate an average value for particle size and compare it with the TEM results. When using the  $M_S$  values given above, the mass of the samples and the fitting parameters  $u/k$  as 102 and 159  $\text{K T}^{-1}$  for Nano1 and Nano2, respectively, we can get the number of particles  $N = M_S/u$  as  $4.45 \times 10^{16}$  and  $5.68 \times 10^{16}$ , respectively. When using the density of pure  $\gamma\text{-Fe}_2\text{O}_3$  as  $\rho = 4900 \text{ kg m}^{-3}$  and assuming that the samples are impurity free, we can write the volume of the single particles as  $1.30 \times 10^{-26}$  and  $1.04 \times 10^{-26} \text{ m}^3$  for Nano1 and Nano2, respectively. These values give the estimation for the radii (in spherical particle case) as  $r_{\text{Nano1}} = 1.5 \text{ nm}$  and  $r_{\text{Nano2}} = 1.4 \text{ nm}$ , respectively. These values are clearly smaller than the ones determined from the TEM images.

### 3.2. Properties of the MR fluids

The sedimentation stability of the MR fluids was studied by tracking the interface between the clear carrier fluid and suspension that formed in all fluids over time. The interface level as a function of time is shown in figure 10. The average sedimentation rate during first 100 h of the measurement for the fluid containing micron sized CI particles and lecithin was  $0.042 \mu\text{m s}^{-1}$ , which is slightly less than in our previous

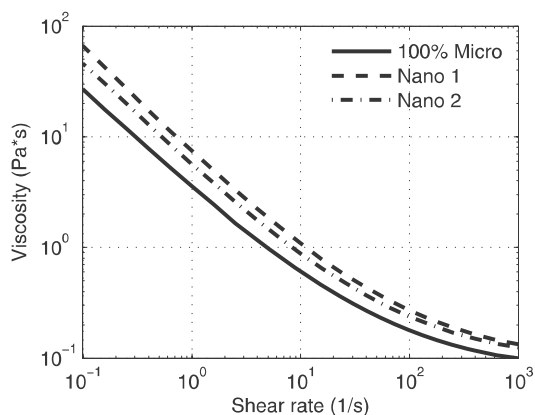


Figure 11. The off-state viscosity curves for the MR fluids.

research ( $0.055 \mu\text{m s}^{-1}$ ) for the similar type of fluid [30]. The likely explanation for the difference is the lecithin that was here added also in the monodisperse MR fluid, but was not used in the previous research. The lecithin generates steric repulsion between the particles by molecular chains crafted on the surfaces, which increases the distance between the adjacent particles and reduces their velocity during sedimentation. López-López *et al* reported improved sedimentation stability of mineral oil based MR fluids when oleic acid was used as a surfactant for CI particles at concentrations above 1 vol% [31]. The addition of the nanoparticles reduces the sedimentation rate significantly. The sedimentation rates for MR fluids with Nano1 and Nano2 particles were  $0.009$  and  $0.012 \mu\text{m s}^{-1}$ , respectively. Results are quite well in line with previous researches. For example, Ngatu and Wereley (2007) reported a sedimentation rate of  $0.0058 \text{ mm s}^{-1}$  for their MR fluid, having total iron particle loading of 70 wt% from which 10% were magnetite nanoparticles [7]. In our previous research we reported only modest improvements in sedimentation stability when the nanoparticle concentration was 5% [30]. The reason might be that the average particle diameters in here were 7.9 and 16.6 nm, which are about three to six times smaller than in our previous research (50 nm). The decrease in particle diameter increases the total surface area which increases the overall friction between the particles and the carrier fluid. What is also evident from the figure 10, is that the interface travel at the end of the measurement is smaller for the MR fluids with nanoparticles compared to the fluid with only larger CI particles. This means that also the packing density is smaller which is in contradiction to the theory, since the nanoparticles should be able to occupy the empty spaces between larger particles, thus increasing the packing density. It is known that the nanoparticles produced by FSP methods tend to form aggregates. The existence of aggregates is the likely explanation for the reduced packing density, since the arbitrary aggregates are not able to pack as tightly as individual particles. The low packing density may make the re-dispersing of the particles easier after long storage.

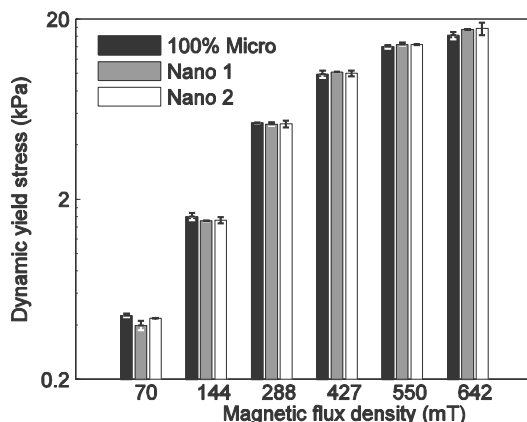


Figure 12. The averages and standard deviations of the dynamic yield stresses of MR fluids as function of magnetic flux density.

The off state viscosity curves for the MR fluids are shown in figure 11. The curves are from down phase of the measurement; the shear rate decreases from 1000 to  $0.01 \text{ s}^{-1}$  in logarithmical increments. It is obvious from the curves that all MR fluids show non-Newtonian behavior as the fluids are strongly shear thinning. This is likely due to hydrodynamic interactions between particles at moderate shear rates. It seems that the viscosities are about to reach a Newtonian plateau at  $1000 \text{ s}^{-1}$ , where the preferred flow structures of the suspensions are reached. Here the viscosities for the MR fluids containing nanoparticles are always higher than for the monodisperse MR fluid. The viscosity of the MR fluid with Nano1 particles is about 84% higher at small shear rates and the difference decreases to about 29% as the shear rate increases to  $1000 \text{ s}^{-1}$ . The corresponding values were 52% and 23% for the Nano2. Theoretically the viscosity of the bidisperse system should be smaller than that of the monodisperse system with the same particle concentration as there is a relationship between viscosity of the suspension and maximum packing density of the particles  $\phi_m$  as described in a model by Krieger and Dougherty [32]:

$$\frac{\eta_s}{\eta_f} = \left(1 - \frac{\phi}{\phi_m}\right)^{-[\eta]\phi_m}, \quad (4)$$

where  $\eta_f$  is the viscosity of the carrier fluid and  $[\eta]$  is the intrinsic viscosity which is equal to 2.5 for spheres. The particles in bidisperse system should reach higher maximum packing density than in the monodisperse system which would lead to smaller viscosity of the suspension. However, the sedimentation measurements revealed that the packing density in our bidisperse MR fluids were in fact smaller than in the monodisperse MR fluid at least in free settling. It can explain the unexpected viscosities as well.

The on-state dynamic yield stresses obtained from steady state measurements by a Bingham model fit are shown in figure 12. The figure shows the averages of two measurements and the standard error of the results. The measurements were done with 0.5, 1, 2, 3, 4 and 5 A coil currents that

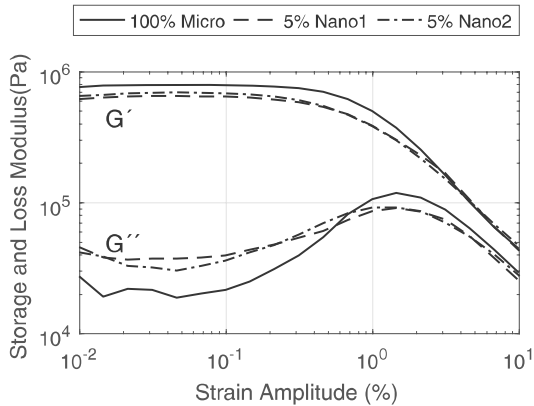


**Figure 13.** Amplitude sweeps for MR fluids at 427 mT flux density containing only micron sized particles and 5% and 15% of magnetite nanoparticles.

resulted to 70, 144, 288, 427, 550 and 642 mT flux densities, respectively. The dynamic yield stress represents the stress needed to continuously break the particle structures in presence of the magnetic field. The yield stresses have a strong dependence on the magnetic flux density as expected for MR fluids. The relationship follows the power-law. At moderately small flux densities ( $B < 300$  mT) the relationship is about  $\tau \sim B^{2.2}$  and at intermediate field strengths ( $400 \text{ mT} < B < 600 \text{ mT}$ ) the power index decreases to about 1.75 because of partial magnetic saturation of the particles. These are quite well in line with the values 2 and 1.5 given by the literature for monodisperse MR fluids [33]. The dynamic yield stresses of the bidisperse fluids are slightly lower at low flux densities and slightly higher at intermediate flux densities compared to the monodisperse fluid. The yield stress is  $-12 \dots +7\%$  with Nano1 particles and  $-4 \dots +9\%$  with Nano2. The Nano2 particles have higher saturation magnetization which can explain the slightly better values. The difference, however, is generally within the standard error of the results. The increase of the yield stress is believed to be caused by the smaller particles filling the voids between microparticles locally enhancing the magnetic field [7, 8]. Leong *et al* [34] used  $\gamma\text{-Fe}_2\text{O}_3$  nanoparticles to prepare bidisperse MR fluids. They used higher total solid concentration than in our research (80.89 wt%) and the saturation magnetization of their nanoparticles was also higher ( $73.8 \text{ Am}^2 \text{ kg}^{-1}$ ). In their research, the dynamic yield stress was higher for a bidisperse MR fluid with 5% nanoparticle concentration compared to a completely monodisperse fluid over the whole flux density range. The increase was about 8% with the highest flux density of 710 mT, which is well in line with our result of 7%–9% increase in dynamic yield stress at 642 mT.

The amplitude sweeps for the MR fluids at 427 mT flux density are shown in figure 13. The nanoparticles have similar effect at all flux densities and therefore we have chosen only the 427 mT flux density to discuss the results. The storage  $G'$  and loss moduli  $G''$  have a linear region at low amplitudes. Here the  $G'$  is considerably higher than the  $G''$  meaning that the deformation is mainly elastic and the

MR fluid behaves in a solid like manner. The deformation happens by stretching and tilting of the particle chain structures. Beyond the linear region the  $G'$  shows a steady decrease while the  $G''$  first passes through a distinct maximum and then a decrease. The change in loss modulus begins at lower strain amplitudes than the storage modulus. This means that the loss modulus is more sensitive to the deformation or the structural changes of the fluid. The end of the linear region is related to the yield stress; as the stress amplitude rises above the yield stress of the MR fluid, the chain structures begin to break and the deformation changes from mainly solid to more viscous. The peaking of the  $G''$  is called strain overshooting and it has been observed with electrorheological (ER) and MR fluids before [35, 36]. Sim *et al* explained that the overshooting is caused by the reformation process of the particle structures. Reformation comprises both destruction of the old structures and formation of new ones that dissipates energy and is seen as increase of  $G''$ . At higher shear rates (amplitudes) the formation of the new structures is reduced and the structures break into smaller clusters or individual particles [36].

The elastic portion of the deformation decreases and viscous portion increases as part of the micron-sized particles is replaced with nanoparticles. This shows as a decrease in the storage modulus  $G'$  and an increase in the loss modulus  $G''$ . The observations are surprising, since the dynamic yield stresses were higher for the bidisperse MR fluids at high flux densities. Wereley *et al* [8] observed similar effects as the elastic limit yield stress, determined from the storage modulus, decreased with increasing iron nanoparticle concentration even though the dynamic yield stress increased.

#### 4. Conclusions

In this paper we have experimentally studied the properties of two  $\gamma\text{-Fe}_2\text{O}_3$  nanoparticles, synthesized by LFS-method, and the properties of bidisperse MR fluids utilizing these nanoparticles. To our knowledge this is the first research where the nanoparticles in the MR fluid have been synthesized by the LFS-method. The synthesis of the nanoparticles was done with precursor feed rates of 3.0 and 8.3  $\text{ml min}^{-1}$ , which led to average particle sizes of 7.9 and 16.6 nm, respectively. The compositions of both samples were verified to be  $\gamma\text{-Fe}_2\text{O}_3$  by XRD and Raman spectroscopy. The saturation magnetization of the smaller particles was  $22 \text{ Am}^2 \text{ kg}^{-1}$ , which was lower than  $43 \text{ Am}^2 \text{ kg}^{-1}$  measured for the larger particles and considerably lower than that of the pure  $\gamma\text{-Fe}_2\text{O}_3$  ( $74 \text{ Am}^2 \text{ kg}^{-1}$ ). The difference is likely caused by the particle sizes as no substantial amount of impurities was detected.

The substitution of 5% of micron-sized particles with nanoparticles in MR fluids offered significant reduction in sedimentation rate; the sedimentation rates of bidisperse fluids with 7.9 nm and 16.6 nm nanoparticles were 0.009 and 0.012  $\mu\text{m s}^{-1}$  respectively which is a significant improvement to the 0.042  $\mu\text{m s}^{-1}$  of monodisperse fluid. However, the off-state viscosity of these bidisperse fluids increased 52%–84% at low shear rates and 23%–29% at high shear rates compared to



the monodisperse fluid. The higher viscosity at low shear rates is probably contributing to the improved sedimentation rate. The dynamic yield stress of the bidisperse MR fluids decreased at the lowest flux densities and increased at the highest flux densities compared to the monodisperse MR fluid. The MR fluid with larger nanoparticles had slightly higher yield stresses, which can be explained by the higher saturation magnetization of particles. The oscillatory testing revealed that the nanoparticles made the response of the MR fluid more viscous.

It was shown, that  $\gamma\text{-Fe}_2\text{O}_3$  nanoparticles synthesized by LFS-method can be used to prepare a bidisperse MR fluids with improved sedimentation stability while still maintaining good MR properties. The drawback was increased off-field viscosity which was likely caused by nanoparticle aggregates characteristic for the particles synthesized with flame spray processes.

## Acknowledgments

The Jenny and Antti Wihuri Foundation is acknowledged for the financial support.

## References

- [1] Bossis G, Volkova O, Laci S and Meunier A 2002 Magnetorheology: fluids, structures and rheology *Ferrofluids: Magnetically Controllable Fluids and Their Applications* ed S Odenbach (Berlin, Heidelberg: Springer Berlin Heidelberg) pp 202–30
- [2] Carlson J D and Jolly M R 2000 MR fluid, foam and elastomer devices *Mechatronics* 10 555–69
- [3] de Vicente J, Klingenberg D J and Hidalgo-Alvarez R 2011 Magnetorheological fluids: a review *Soft Matter* 7 3701–10
- [4] Ashtiani M, Hashemabadi S H and Ghaffari A 2015 A review on the magnetorheological fluid preparation and stabilization *J. Magn. Magn. Mater.* 374 716–30
- [5] Chaudhuri A, Wang G and Wereley N M 2005 Substitution of micron by nanometer scale powders in magnetorheological fluids *Int. J. Mod. Phys. B* 19 1474–80
- [6] Chin B D, Park J H, Kwon M H and Park O O 2001 Rheological properties and dispersion stability of magnetorheological (MR) suspensions *Rheol. Acta* 40 211–9
- [7] Ngatu G T and Wereley N M 2007 Viscometric and sedimentation characterization of bidisperse magnetorheological fluids *Trans. Magn.* 43 2474–6
- [8] Wereley N M, Chaudhuri A, Yoo J H, John S, Kotha S, Suggs A, Radhakrishnan R, Love B J and Sudarshan T S 2006 Bidisperse magnetorheological fluids using Fe particles at nanometer and micron scale *J. Intell. Mater. Syst. Struct.* 17 393–401
- [9] Rosenfeld N, Wereley N M, Radhakrishnan R and Sudarshan T S 2002 Behavior of magnetorheological fluids utilizing nanopowder iron *Int. J. Mod. Phys. B* 16 2392–8
- [10] Lopez-Lopez M T, Kuzhir P, Laci S, Bossis G, Gonzalez-Caballero F and Duran J D G 2006 Magnetorheology for suspensions of solid particles dispersed in ferrofluids *J. Phys.: Condens. Matter* 18 2803–13
- [11] Shimada K, Akagami Y, Fujita T, Miyazaki T, Kamiyama S and Shibayama A 2002 Characteristics of magnetic compound fluid (MCF) in a rotating rheometer *J. Magn. Magn. Mater.* 252 235–7
- [12] Patel R 2011 Mechanism of chain formation in nanofluid based MR fluids *J. Magn. Magn. Mater.* 323 1360–3
- [13] Viota J L, Duran J D G, Gonzalez-Caballero F and Delgado A V 2007 Magnetic properties of extremely bimodal magnetite suspensions *J. Magn. Magn. Mater.* 314 80–6
- [14] Serna C J and Morales M P 2004 Maghemite ( $\gamma\text{-Fe}_2\text{O}_3$ ): a versatile magnetic colloidal material *Surface and Colloid Science* ed E Matijevic and M Borkovec (Boston, MA: Springer US) pp 27–81
- [15] Ulrich D G 1971 Theory of particle formation and growth in oxide synthesis flames *Combust. Sci. Technol.* 4 47–57
- [16] Kammler H K, Mädler L and Pratsinis S E 2001 Flame synthesis of nanoparticles *Chem. Eng. Tech.* 24 583–96
- [17] Teleki A, Wengeler R, Wengeler L, Nirschl C H and Pratsinis S E 2008 Distinguishing between aggregates and agglomerates of flame-made  $\text{TiO}_2$  by high-pressure dispersion *Powder Technol.* 181 292–300
- [18] Mäkelä J M, Keskinen H, Forsblom T and Keskinen J 2004 Generation of metal and metal oxide nanoparticles by liquid flame spray process *J. Mater. Sci.* 39 2783–8
- [19] Haapanen J, Aromaa M, Teisala H, Tuominen M, Stepien M, Saarinen J J, Heikkilä M, Toivakka M, Kuusipalo J and Mäkelä J M 2015 Binary  $\text{TiO}_2/\text{SiO}_2$  nanoparticle coating for controlling the wetting properties of paperboard *Mater. Chem. Phys.* 149–150 230–7
- [20] Mäkelä J M, Hellsten S, Silvonen J, Vippola M, Levänen E and Mäntylä T 2006 Collection of liquid flame spray generated  $\text{TiO}_2$  nanoparticles on stainless steel surface *Mater. Lett.* 60 530–4
- [21] Carlson D J 2008 Magnetorheological fluids *Smart Materials* ed M Schwartz (Boca Raton, FL: CRC Press) ch 17
- [22] Harra J, Nikkanen J-P, Aromaa M, Suhonen H, Honkanen M, Salminen T, Heinonen S, Levänen E and Mäkelä J M 2013 Gas phase synthesis of encapsulated iron oxide–titanium dioxide composite nanoparticles by spray pyrolysis *Powder Technol.* 243 46–52
- [23] Li Y-S, Church J S and Woodhead A L 2012 Infrared and Raman spectroscopic studies on iron oxide magnetic nanoparticles and their surface modifications *J. Magn. Magn. Mater.* 324 1543–50
- [24] Mandzy N, Grulke E and Druffel T 2005 Breakage of  $\text{TiO}_2$  agglomerates in electrostatically stabilized aqueous dispersions *Powder Technol.* 160 121–6
- [25] Jönkkäri I, Kostamo E, Kostamo J, Syrjälä S and Pietola M 2012 Effect of the plate surface characteristics and gap height on yield stress of a magnetorheological fluid *Smart Mater. Struct.* 21 75030–40
- [26] Laun H M, Schmidt G, Gabriel C and Kielburg C 2008 Reliable plate–plate MRF magnetorheometry based on validated radial magnetic flux density profile simulations *Rheol. Acta* 47 1049–59
- [27] Molchan I S, Thompson G E, Lindsay R, Skeldon P, Likodimos V, Romanos G E, Falaras P, Adamova G, Iliev B and Schubert T J S 2014 Corrosion behaviour of mild steel in 1-alkyl-3-methylimidazolium tricyanomethanide ionic liquids for  $\text{CO}_2$  capture application *RSC Adv.* 4 5300–11
- [28] Nurdin I, Johan M R, Yaacob I I, Ang B C and Andriyana A 2014 Synthesis, characterization and stability of superparamagnetic maghemite nanoparticle suspension *Mater. Res. Innov.* 18 200–3
- [29] Jun Y W, Seo J W and Cheon J 2008 Nanoscaling laws of magnetic nanoparticles and their applicabilities in biomedical sciences *Acc. Chem. Res.* 41 179–89
- [30] Jönkkäri I, Matti I and Syrjälä S 2015 Sedimentation stability and rheological properties of ionic liquid-based bidisperse magnetorheological fluids *J. Intell. Mater. Syst. Struct.* 26 2256–65

- [31] López-López M T, De Vicente J, González-Caballero F and Durán J D G 2005 Stability of magnetizable colloidal suspensions by addition of oleic acid and silica nanoparticles *Colloids Surf. A* **264** 75–81
- [32] Krieger I M and Dougherty T J 1959 A mechanism for non-Newtonian flow in suspensions of rigid spheres *Trans. Soc. Rheol.* **3** 137–52
- [33] Bossis G, Laci S, Meunier A and Volova O 2002 Magnetorheological fluids *J. Magn. Magn. Mater.* **252** 224–8
- [34] Leong S A N, Mazlan S A, Samin P M and Idris A 2016 Ubaidillah, performance of bidisperse magnetorheological fluids utilizing superparamagnetic maghemite nanoparticles *AIP Conf. Proc.* **1710** 030050
- [35] Li W H, Du, H and Guo N Q 2004 Dynamic behavior of MR suspensions at moderate flux densities *Mater. Sci. Eng. A* **371** 9–15
- [36] Sim H G, Ahn K H and Lee S J 2003 Three dimensional dynamics simulation of electrorheological fluids under large amplitude oscillatory shear flow *J. Rheol.* **47** 879–95



# PUBLICATION

## IV



**Fabrication of ultrathin multilayered superomniphobic nanocoatings by  
liquid flame spray, atomic layer deposition, and silanization**  
**Sorvali, M., Vuori, L., Pudas, M., Haapanen, J., Mahlberg, R., Ronkainen, H.,  
Honkanen, M., Valden, M. and Mäkelä, J. M.**

*Nanotechnology* 29.(2018), 185708  
DOI: 10.1088/1361-6528/aaaffc

**Publication reprinted with the permission of the copyright holders**



# Fabrication of ultrathin multilayered superomniphobic nanocoatings by liquid flame spray, atomic layer deposition, and silanization

Miika Sorvali<sup>1</sup> , Leena Vuori<sup>2</sup>, Marko Pudas<sup>3</sup>, Janne Haapanen<sup>1</sup>, Riitta Mahlberg<sup>4</sup>, Helena Ronkainen<sup>4</sup>, Mari Honkanen<sup>5</sup>, Mika Valden<sup>2</sup> and Jyrki M Mäkelä<sup>1</sup> 

<sup>1</sup> Aerosol Physics, Laboratory of Physics, Faculty of Natural Sciences, Tampere University of Technology, PO Box 692, FI-33101 Tampere, Finland

<sup>2</sup> Surface Science, Laboratory of Photonics, Faculty of Natural Sciences, Tampere University of Technology, PO Box 692, FI-33101 Tampere, Finland

<sup>3</sup> Picosun Oy, FI-02430 Masala, Finland

<sup>4</sup> VTT Technical Research Center of Finland, PO Box 1000, FI-02044 Espoo, Finland

<sup>5</sup> Materials Characterization, Laboratory of Materials Science, Faculty of Engineering Sciences, Tampere University of Technology, PO Box 589, FI-33101 Tampere, Finland

E-mail: miika.sorvali@tut.fi

Received 14 December 2017, revised 6 February 2018

Accepted for publication 16 February 2018

Published 9 March 2018



CrossMark

## Abstract

Superomniphobic, i.e. liquid-repellent, surfaces have been an interesting area of research during recent years due to their various potential applications. However, producing such surfaces, especially on hard and resilient substrates like stainless steel, still remains challenging. We present a stepwise fabrication process of a multilayered nanocoating on a stainless steel substrate, consisting of a nanoparticle layer, a nanofilm, and a layer of silane molecules. Liquid flame spray was used to deposit a TiO<sub>2</sub> nanoparticle layer as the bottom layer for producing a suitable surface structure. The interstitial Al<sub>2</sub>O<sub>3</sub> nanofilm, fabricated by atomic layer deposition (ALD), stabilized the nanoparticle layer, and the topmost fluorosilane layer lowered the surface energy of the coating for enhanced omniphobicity. The coating was characterized with field emission scanning electron microscopy, focused ion beam scanning electron microscopy, x-ray photoelectron spectroscopy, contact angle (CA) and sliding angle (SA) measurements, and microscratch testing. The widely recognized requirements for superrepellency, i.e. CA > 150° and SA < 10°, were achieved for deionized water, diiodomethane, and ethylene glycol. The mechanical stability of the coating could be varied by tuning the thickness of the ALD layer at the expense of repellency. To our knowledge, this is the thinnest superomniphobic coating reported so far, with the average thickness of about 70 nm.

Keywords: nanocoating, liquid flame spray, atomic layer deposition, superomniphobic, silanization, aerosol synthesis, multilayered

(Some figures may appear in colour only in the online journal)

## Introduction

Since surfaces are often in contact with water or other liquids, controlling their wettability has already been an interesting research area for several decades. A surface is considered hydrophobic if it forms with a water droplet at a contact angle (CA) greater than  $90^\circ$  and superhydrophobic when this angle exceeds  $150^\circ$ . If this water-repellency is extended to also cover other liquids, the terms superomniphobic and superamphiphobic are introduced. We will use the former in this paper, but the two are basically equivalent in meaning. True superrepellency also requires either CA hysteresis, i.e. the difference between the advancing and receding CAs, or the smallest inclination angle of the surface that makes the droplet roll off, the sliding angle (SA), to be lower than  $10^\circ$  [1–3]. These two requirements are often considered analogous to each other and therefore both not studied. Interest in superrepellent surfaces has been growing continuously during the last decade [4–6]. This is mainly due to the tremendous potential that superomniphobic surfaces hold for i.e. microfluidic [7], antifouling [8, 9], self-cleaning [1, 9], filtration [10, 11], drag reduction [1, 12], chemical shielding [13], droplet manipulation [14], and corrosion protection [15] applications.

The basic principles, used today, governing the spreading of a liquid droplet on a surface were discovered by Wenzel [16], and Cassie and Baxter [17]. They found two possible wetting states exist for the droplet: the Wenzel state and the Cassie–Baxter state. The latter of the two describes a superrepellent surface, and the equation governing the degree of wetting is called the Cassie–Baxter equation, written as follows:

$$\cos \theta^* = f_{SL} \cos \theta + f_{SL} - 1, \quad (1)$$

where  $\theta^*$  is the apparent CA,  $\theta$  is the equilibrium CA, and  $f_{SL}$  is the area fraction of the solid–liquid interface compared to the whole surface area shadowed by the droplet. The roughness of the surface affects the area fraction term, and  $\theta$  contains the effect of the surface material. Equation (1) can often be used in explaining changes in wettability [13, 18, 19].

Superrepellency is most often achieved with a so-called hierarchical surface structure that consists of a nanostructure on top of a microstructure and is combined with a surface modification that lowers the surface energy. With careful enough manipulation of the surface asperities, it is possible to reach even extremely strong superomniphobicity without paying too much attention to the surface chemistry [6], but practical reasons usually limit the extent to which this can be accomplished.

A multitude of different techniques have been utilized in fabricating hierarchical surface structures [20–24], but the materials used always limit the possible fabrication methods. For hard and resistant substrate materials, like stainless steel, modification of the surface structure is often very difficult or even impossible, in which case a coating might be required [25]. The vast number of applications, containing stainless steel surfaces, that could benefit from superomniphobicity,

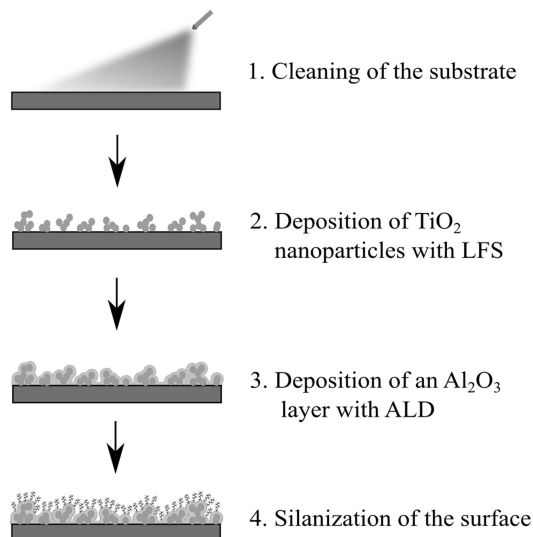


**Figure 1.** The entire fabrication process of the coating presented schematically in steps.

makes studying the matter meaningful. Some papers have been published presenting superomniphobic coatings on steel surface, but the coatings were mainly quite thick and had plenty of room for improvement in performance and durability. Also, only a few of them used stainless steel as a substrate [26–28]. Slippery liquid-infused porous surfaces have also been used to achieve strongly omniphobic coatings on steel [29].

A common problem with nanocoatings is their poor mechanical stability, and finding new solutions to reinforce them is a challenging task. One possibility to tackle this problem is by using layered structures that have not been very extensively studied regarding superomniphobic coatings. The main challenge is to strengthen the nanoparticle layer without suppressing the functionality it produces. Atomic layer deposition (ALD) has earlier been shown to enhance the mechanical durability of nanoparticle films and nanocolloidal crystals [30–32]. It was therefore chosen for this study as the method for nanoparticle layer reinforcement.

The goal of this study was to produce a new kind of superomniphobic coating on stainless steel, exploiting a layered nanostructure. Superoleophobic surfaces have been made using nanoparticles synthesized by flame spray pyrolysis, and combined with a top layer of a fluorosilane [33]. However, the herein used combination of the three chosen fabrication methods has not been studied before, to the best of our knowledge. We were striving for a very thin coating with strong repellency against various liquids. Even though the coating method is applied to stainless steel in this study, a variety of substrate materials could be chosen. In general, liquid flame spray (LFS) offers an economically efficient, well scalable, and flexible way to fabricate nanomaterials.

Figure 1 describes schematically the stepwise fabrication process of the coating.

The process can be divided into four distinct steps. First, the steel substrate was cleaned with various solvents. Secondly, TiO<sub>2</sub> nanoparticles were deposited on the substrate via LFS to provide a suitable surface topography. Thirdly, the nanoparticle layer was coated with a thin Al<sub>2</sub>O<sub>3</sub> layer using ALD in order to reinforce the deposited nanoparticle layer, and lastly the surface was covered with fluorosilane molecules for lowering the surface energy. The coating materials used were mainly chosen due to experimental experience, assisting in controlling their synthesis processes and the end product properties. All the steps along with the characterization methods are described in more detail in the following section.

## Experimental section

### Materials

Austenitic stainless steel plates ( $\phi$  17 cm, thickness of 0.6 mm) were acquired from Fiskars Finland Oy Ab and cleaned with acetone (99.5+%, VWR International), isopropanol (IPA, 99.8%, VWR International) and deionized (DI) water prior to the actual coating process. The samples were dried with a lint-free cloth and pressurized air. TiO<sub>2</sub> nanoparticles were synthesized from titanium(IV) isopropoxide (TTIP, 97+%, Alfa Aesar) dissolved in IPA. The precursors for the ALD process were trimethylaluminum (TMA, Volatec Oy) and water. (heptadecafluoro-1,1,2,2-tetrahydrodecyl) trichlorosilane (HDF, 97+%, Gelest) dissolved in hexane (95%, Sigma-Aldrich) was used for silanization. Test liquids for CA and SA measurements were DI water, diiodomethane (DIM, 99%, Sigma-Aldrich), ethylene glycol (EG, 99.8%, Sigma-Aldrich), commercial olive oil (OO), and hexadecane (HDEC, 99%, Sigma-Aldrich). The set of test liquids were selected primarily on the basis of their surface tension. The surface tension values in 20 °C for the DI water, DIM, EG, OO, and HDEC are 71.99 (25 °C) [34], 50.88 (20 °C) [35], 47.99 (25 °C) [34], 32.0 (20 °C) [36], and 27.49 (20 °C) [35] mN/m, respectively.

### LFS

LFS is an aerosol synthesis method for producing a variety of metal and metal oxide nanoparticles and coatings. It can be classified as a specific type of flame spray pyrolysis method, and several publications have been written describing the synthesis process in detail [37–42]. However, there are no earlier publications with the experimental setup used in this paper. The setup consisted of a burner, a so-called residence tube and the substrate to be coated, as presented in figure 2.

In LFS synthesis, a liquid precursor solution is fed to a burner along with hydrogen and oxygen flows. The hydrogen flow atomizes the liquid jet and also acts as a combustion gas. The atomized droplets go through a complex combination of mechanisms in the flame, including precursor decomposition

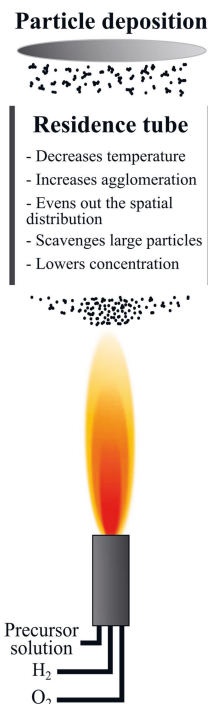


**Figure 2.** A schematic representation of the LFS coating setup with the description of the effect of the residence tube.

and particle nucleation, resulting in nanoparticle formation. In this study, a precursor solution with metallic Ti concentration of 50 mg ml<sup>-1</sup> was fed to the flame at a feed rate of 12 ml min<sup>-1</sup>, and the hydrogen and oxygen flows used were set to 50 and 15 l min<sup>-1</sup>, respectively.

What distinguishes the rest of the process in this study from a more conventional LFS synthesis is the addition of a residence tube between the burner and the substrate. It modifies the particle flow emerging from the flame and lowers the temperature on the substrate. Maximum temperatures of about 2600 °C have been measured close to the burner [38], whereas the temperatures measured after the residence tube have ranged from around 200 to 500 °C. The residence tube promotes agglomeration and leads to some particle losses to the walls, but also scavenges large particles and evens out the spatial distribution, which should help in producing a uniform coating across the substrate area [43, 44]. In the particle deposition, the substrate was placed on the end of the residence tube for a specific coating time, chosen to be 6 s for the final coating.

### ALD

ALD is a specific type of chemical vapor deposition method, where the substrate is exposed to isolated gas pulses in a cyclic manner [45]. ALD can be used to coat objects of practically all geometries, and the resulting layer is extremely

even and conformal. One of the most common industrial branches utilizing the method nowadays is electronics, but the method has also proven to be suitable for producing different kinds of passivation and protective layers [46, 47].

Here, the LFS-coated samples were first oxidized with mixtures of oxygen (grade 5) and nitrogen flows at 300 °C. First, a mixture with approximately 12% oxygen was used for 15 min, after which the oxygen fraction was raised to 36% for 1 min. The specific parameter values were arbitrarily selected, ensuring sufficient oxidation of all organic contaminants on the surface. An Al<sub>2</sub>O<sub>3</sub> layer with a thickness of 10 nm was then deposited on top of the nanoparticle layer, also at 300 °C. The whole process was performed with a Picosun P-1000 ALD system.

### *Silanization*

Liquid phase deposition (LPD) of the HDF silane was performed on the ALD-coated samples. Freshly prepared samples were silanized in the as-received state. For samples that had to be stored for an extended time period, a UV light treatment of 30 min was applied before the silanization process. This was done in order to decrease the amount of organic impurities that readily accumulate on surfaces during storage in atmospheric conditions, thereby promoting the adherence of silane molecules on the topmost Al<sub>2</sub>O<sub>3</sub> layer. UV-C lamps with the peak intensity at 254 nm wavelength were chosen, because they have been observed to decompose organic material without the presence of an additional photocatalyst.

HDF was dispersed into hexane at a ratio of 1:1000 and stirred for 10 min, after which the samples were immersed in the solution for 10 min. Subsequently, they were rinsed with hexane and DI water, followed by drying with a nitrogen flow. The details of a successful silanization process are described elsewhere [47, 48].

### *Surface properties analysis*

The wettability of the surface was studied using CA measurements and SA testing. Test liquids in the amount of 4–6  $\mu$ l droplets were placed on the surface and filmed at the same time. The static CAs were determined, when the shape of the droplet had stabilized, and the accuracy of the measurement was estimated to be around  $\pm 1^\circ$ . SAs were tested on a tilted surface by adjusting the inclination angle to a certain value, placing a liquid droplet on the surface and observing if it rolls off or sticks to it.

Microscratch testing was performed mainly to assess the adhesion of the coating to the substrate. The method is typically used for evaluating cohesion and adhesion of thin films and coatings [49]. The testing was based on a Rockwell diamond stylus (diameter of 20  $\mu$ m and cone angle of 120°) sliding on the coated surface with a continuously increasing load (0.03–1 N). The reported load values (or pressure values derived from them) were averaged over three scratches. Friction force, penetration depth, and acoustic emission were also measured during the scratching procedure.

### *Surface characterization*

A Zeiss UltraPlus field emission scanning electron microscope (FESEM) was used for imaging the surface after every fabrication step and after microscratch testing. Cross-sectional milling with Ga<sup>+</sup> ions and SEM imaging was performed with a Zeiss Crossbeam 540 focused ion beam scanning electron microscope (FIB-SEM). In this study, a gold layer was sputtered on the surface for improving electrical conductivity, and a Pt layer on top of that to ensure the protection of the coating during the milling process. The FIB-SEM used was equipped with an energy-dispersive x-ray spectroscopy (EDS) detector, so elemental mapping was also conducted across the produced coating layer alongside cross-sectional imaging.

X-ray photoelectron spectroscopy (XPS) was utilized for analyzing the elemental composition of the surface between the coating steps. The XPS measurements were conducted with non-monochromatic Al K $\alpha$  radiation ( $h\nu = 1486.6$  eV), and the spectra were recorded in a fixed analyzer transmission mode at normal emission and 20.0 eV pass energy. The binding energy was calibrated to 285.0 eV for aliphatic carbon, and the photoelectron peaks were fitted with a combination of Gaussian and Lorentzian line shapes and Shirley background, using CasaXPS software version 2.3.16 [50].

## **Results and discussion**

### *Determination of parameters and superomniphobicity*

The amount of LFS-generated TiO<sub>2</sub> nanoparticles and the thickness of the ALD coating were iterated on the basis of crude mechanical stability testing (observing the effect of the insertion and subsequent removal of a scotch tape with FESEM) and CA measurements. Common problems with porous nanoparticle layers are the weak cohesion between the particles and their poor adhesion to the substrate. The goal of the iteration was to find a balance between liquid repellency and particle layer stability, having an emphasis on the repellency. Too short an LFS coating time led to a fairly robust coating, but to an inadequate surface roughness for producing effective repellency. With a long coating time, good repellency could be achieved, but the resulting coating was very fragile and unstable, meaning most of the material came off in the scotch tape test. A coating time of 6 s was determined suitable. In addition to these problems, too short a coating time led to a net-like microscale structure with a larger aggregate/agglomerate size, and thus lowered the number concentration of secondary particles on the surface. This possibly resulted from some surface treatment done to the steel substrate during its manufacturing process. Once the coating time was increased, the net-like structure got buried under the additional particles, thus increasing the surface coverage of the bare steel significantly.

The role of the ALD layer was to attach the particles more strongly to the substrate and to each other, but without covering the favorable topography and porosity produced by them. A similar effect has earlier been observed in the case of

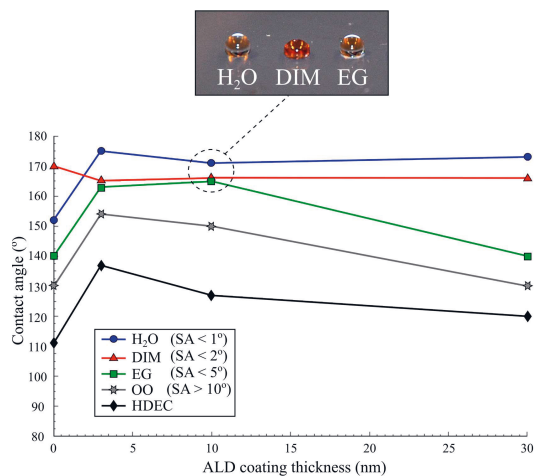


**Figure 3.** CA as a function of ALD coating thickness for different test liquids. SA values are presented in the legend for each liquid, corresponding the ALD thickness of 10 nm. The photo above, presenting droplets of three liquids lying on the surface, was not taken from a CA measurement.

solar cells, where the ALD coating increased the mechanical stability of the nanoparticle layer, but lowered its porosity [51]. The first priority in determining the ALD coating thickness was achieving strong omniphobicity. The effect of the ALD coating thickness to the CA was studied for the chosen LFS coating time (6 s), and figure 3 describes the CA as a function of the thickness along with the measured SA values for the 10 nm ALD samples. The SA value for the HDEC was not measured, since OO with a higher surface tension did not fulfill the SA requirement for superrepellency. All of the measured samples were silanized.

The 3 nm Al<sub>2</sub>O<sub>3</sub> layer raised the CA in most cases compared to the samples with no ALD coating. This behavior implies that Al<sub>2</sub>O<sub>3</sub> might be a more favorable substrate for LPD of HDF silane than stainless steel or TiO<sub>2</sub>, which led to a higher-quality silane layer, indicated by the greater CA values. Since a large part of the surface was not covered with nanoparticles after only LFS coating, most of the silane molecules probably adsorbed on the steel surface. Stainless steel is generally a difficult substrate material to silanize without pretreatment [52]. Another possible explanation for this difference could be the stabilizing effect of the ALD layer. If the LFS particle layer without ALD was too unstable, the silanization process might have rendered the surface structure more unfavorable for omniphobicity by raising the fraction of the solid–liquid interface. Based on equation (1), this would reduce the CAs. The one measurement point (0 nm for DIM) that deviates from the trend can be considered a measurement error or an anomaly.

As the ALD coating thickness was increased from 3 nm, the CA values began to decrease continuously. This was presumably caused by the Al<sub>2</sub>O<sub>3</sub> covering the surface nanostructures that were formed by the nanoparticles. When

additional material was deposited on top of the very porous structure, the pores started to fill up, lowering the porosity and the specific surface area. According to the theoretical formulations, this should reduce the apparent CAs by increasing the solid–liquid area fraction. Simultaneously, the mechanical durability increased (observed earlier with the scotch tape tests), so some kind of a compromise between liquid repellency and durability has to be made, when optimizing the parameters with a certain application in mind. This study does not cover the fine tuning of the parameters from the perspective of mechanical stability, nor are we trying to find optimal parameters for a specific application.

The difference in repellency between the 3 and 10 nm samples was not too great, so 10 nm was chosen over 3 nm as the more optimal thickness in complete performance of the coating. On the other hand, a 30 nm ALD layer already had a reasonably large negative impact on the repellency, at least on the liquids with lower surface tension, so it was discarded as the final coating thickness. If repellency towards high-surface tension liquids would suffice, a thicker ALD layer would likely be a better option.

As already was stated in the introduction section, perfect superomniphobicity is practically impossible to reach. However, our coating fared quite well amongst other reported superomniphobic coatings. Reaching CAs of over 150° for the DI water, DIM, EG, and OO, and with significantly lower SA values than 10° for the first three, we can regard our final coating superomniphobic to a certain extent.

#### Surface topography after different steps

Imaging of the surface after each coating step provides insight into the actual role of the different layers. The LFS nanoparticle layer was supposed to be responsible for producing a surface structure that is essential for effective omniphobicity. The ALD layer should work as a stabilizing layer on top of the particle layer without covering the topography. The function of silanization was to lower the surface energy, and it was assumed not to affect the surface structure to a large degree. Figure 4 shows FESEM images after each fabrication step with the chosen parameters. Samples were cut from random locations of the sample plates.

The deposited nanoparticles were dispersed very uniformly across the whole imaged area of the samples, and everything from single primary particles to about micron-sized agglomerates in length are observed. Quite a significant portion of the steel surface still remained uncovered. The surface coverage can be estimated, based on graphical analysis (ImageJ) from different FESEM images using automatic thresholding, to be around 30%. Manual thresholding led to a bit higher percentage of surface coverage, but the user bias is also difficult to quantify in this case. In this sense, automatic thresholding can be seen as the more reliable approximation. This value applies approximately for the samples representing all different steps.

An accurate value is, however, difficult to obtain due to differences in contrast between the FESEM images. Also, a little bit of an oxide particle (probably mostly iron oxide)

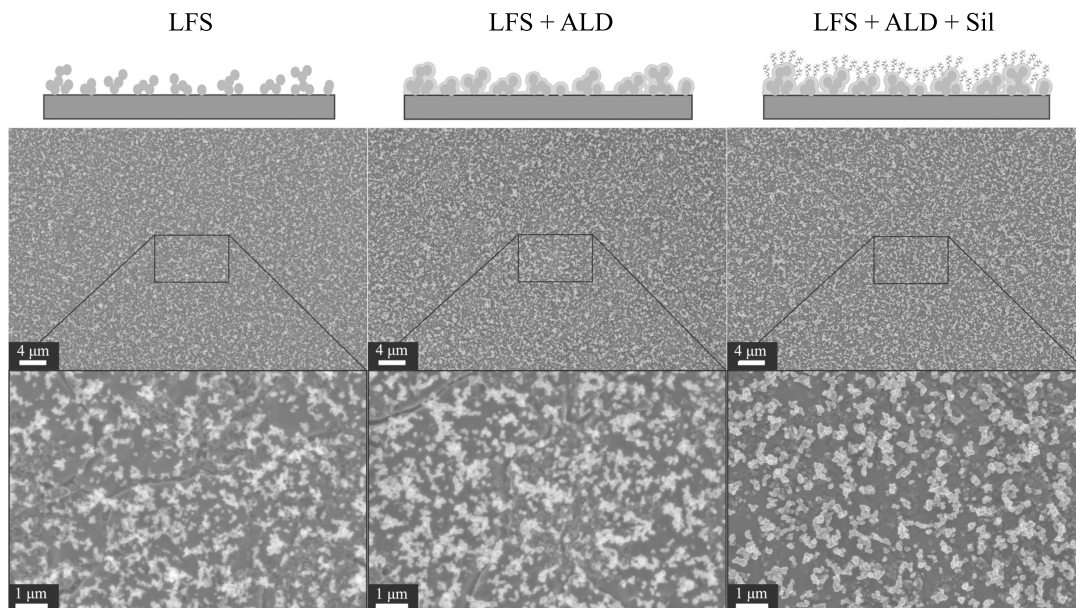


**Figure 4.** FESEM images of the sample surfaces after every step in the fabrication process. The LFS coating time was 6 s and the ALD coating thickness 10 nm.

structure was observed forming on top of the steel surface during the oxidation process before the ALD coating. The oxide particles were of roughly similar size as the titanium dioxide primary particles, which makes distinguishing the real background from the actual coating material more challenging. The precise effect of the oxide structure to the coating properties is unknown, but for example, in case of depositing a similar ALD layer on top of  $\text{MoS}_2$ , oxidizing the surface in advance was observed to improve the quality of the forming ALD layer [53].

The visual difference that the thin ALD coating caused to the LFS-coated surface is reasonably small. The primary particle size seems to be roughly 50 nm (considering some nanometers from sample carbonization) and the  $\text{Al}_2\text{O}_3$  coating increased it slightly. Otherwise, the ALD process did not significantly affect the surface topography, as was expected. Also, the silanization process did not drastically modify the surface structure of the coating. Even though slight discrepancies can be seen between the images representing different steps (figure 4), it has to be accounted for that they are not images of the same sample after each fabrication step, but rather just representing a set of parameters. Some larger differences were observed in the case of certain samples (possibly damaged), but figure 3 can be considered to represent the process fairly well.

#### Surface elemental analysis by XPS

Based on the FESEM images, the surface structure does not undergo drastic changes during the hierarchical sample fabrication process, but the XPS results reveal that each coating

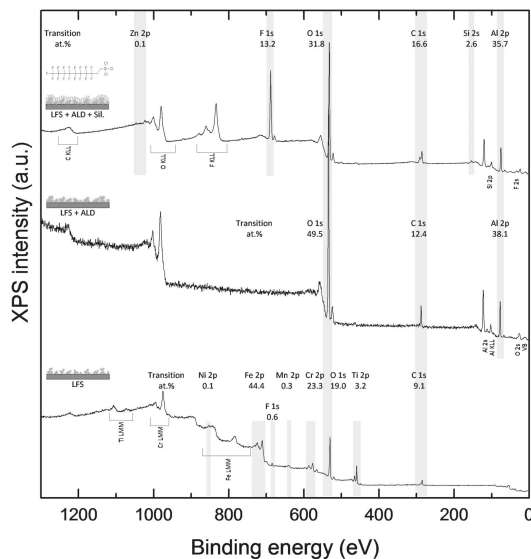


**Figure 5.** XPS survey spectra and the relative elemental surface concentrations of the samples after each fabrication step.

step alters the surface chemistry significantly. The survey spectra and the relative elemental surface concentrations, calculated from the high-resolution spectra, are presented in figure 5.

The survey spectrum of the LFS sample (after the first coating step) shows that the outermost surface (up to  $\sim 10$  nm



information depth) consisted of both TiO<sub>2</sub> nanoparticles and stainless steel. XPS measurements from small areas at different locations reveal that there are local differences in the Fe concentration. This is in good accordance with the FESEM images (figure 4) that display only a partial surface coverage of the steel surface. Apart from a typical amount of organic contamination and a trace amount of fluorine, the surface was free of impurities. This implies that no additional contamination was produced in the flame, which is usually the case in a normal high-velocity and high-temperature LFS process. The organic contaminants originated from the exposure to atmospheric conditions and consist mostly of C–C, C–O, and C=O bonds observed in both the C 1s and O 1s spectra. The relatively high Fe/Ti atomic ratio (even regarding the low surface coverage) can be attributed to the different information depths of Ti 2p and Fe 2p transitions (~6 and 4.5 nm, respectively). For Ti, this discrepancy leads to a larger information volume with a lower relative atomic fraction than for Fe.

The assumption that was made earlier about the evenness and the conformity of the ALD coating, are strongly supported by the XPS measurements after the second fabrication step. The only observed signals came from the Al<sub>2</sub>O<sub>3</sub> layer and surface impurities, and no Fe or Ti could be detected. Since the ALD layer thickness (10 nm) was very close to the XPS information depth, the coating material had to be very uniform to attenuate the signal from the nanoparticles completely. The contaminants originated again from the atmospheric exposure during the time between the ALD coating and the XPS measurement.

The survey spectrum of the final multilayered coating (LFS + ALD + Sil) shows the nanomolecular nature of the HDF silanization process. Signals were observed from both the silane molecules (CF<sub>2</sub> and CF<sub>3</sub> bonds observed in the C 1s and F 1s spectra, and Si as a new element on the surface) and the underlying Al<sub>2</sub>O<sub>3</sub> layer. The presence of strong Al signal verifies that the HDF (molecular length of 1–2 nm) overlayer is of nanomolecular nature. As there was no Cl visible in the XPS spectrum, it can be assumed that the hydrolysis of the silane molecules proceeded sufficiently to form a network of covalent bonds with the Al<sub>2</sub>O<sub>3</sub> substrate. The presence of chlorine would have implied that some of the molecules were completely, or at least partially, unhydrolyzed, which typically leads to a chemically less robust topmost layer. The uniform coverage of silane molecules throughout the sample was confirmed by inspecting high-resolution F 1s spectra from several small (~10 μm) detection areas. The analysis of the high-resolution C 1s spectrum reveals a contribution from the organic impurities, in addition to the CF<sub>2</sub> chain, to the C 1s intensity. A trace amount of Zn was also observed, probably caused by the coating cycles of ZnO that were done with the ALD system before the coating of the measured samples. This is, nevertheless, insignificant considering the final coating.

### Cross-sectional imaging

Cross-sectional imaging was performed to study the thickness and the topographical features in more detail, and with the EDS analysis we wanted to study the distribution of the Al<sub>2</sub>O<sub>3</sub> in the coating. A gold layer was sputtered on top of the sample to enhance electrical conductivity. Also, a layer of platinum had to be deposited on top of the coating to ensure that the true structure was being imaged. Both of these pretreatments are visible in figure 6 that presents cross-sectional SEM images with two different magnifications.

The small bright dots, visible in figure 6(b), are Au particles originating from the sputtering, and the Pt layer, well visible in figure 6(a), has a thickness of about 1–2 μm. From a larger perspective, the coating seems quite even across the sample area, but the higher magnification reveals the undulating surface topography produced by the nanoparticle agglomerates. The thickness of the coating varies generally between the minimum value of ca. 10–15 nm, probably corresponding to areas with only ALD and silane layers, and the maximum value of about 160–200 nm (a wide estimation due to uncertainties), based on the SEM images. If we approximate the area of the coating in the images graphically, and calculate the thickness of a hypothetical, completely even layer with the same cross-sectional area, we get an average value of around 70 nm. This is in no sense an accurate measure and it varies roughly ±10 nm between different images, but it gives an idea of the size scale.

Since the resolution of the SEM images is not adequate to make accurate approximations, the EDS results can be used to support the observed thickness values. They showed an Al Kα signal coming from the entire length of the cross section that has been interpreted as the coating thickness from the SEM images. This also supports the hypothesis that the ALD layer covers the titania agglomerates across the whole particle layer, and penetrates deep into the porous layer. This transport inside the layer is probably essential for the reinforcing function of the ALD coating. Considering both the calculated average value and the estimated maximum thickness of around 180 nm, the produced coating is the thinnest reported superomniphobic coating, as far as we know. However, the deposition of the platinum layer might densify some of the larger agglomerates, thus compressing the layer a little.

### Microscratch testing

The microscratch testing was performed to assess the adhesion of the coating to the substrate and its performance under load. Figure 7 presents optical and FESEM images of one of the scratches produced on the surface. The discrepancies between different scratches were quite minor, so one scratch represents all of them very well. The pressure values were calculated by dividing the normal force pushing down the diamond tip by half of the area of the circle (20 μm in diameter) projected by the tip on the sample surface. Therefore, in every case the pressure values are approximations based on averaging over the entire scratch width, as they are presented to give an impression of the order of magnitude. Only about a

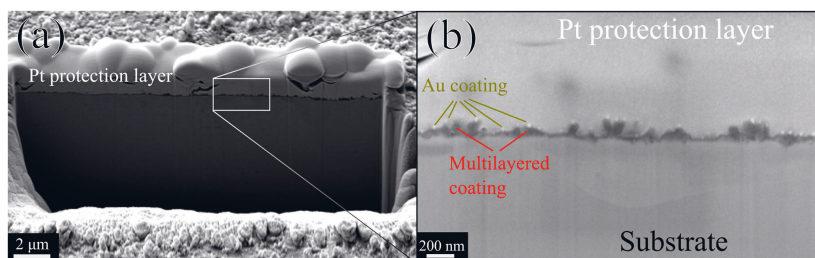


**Figure 6.** SEM images of (a) the hole milled with FIB using  $\text{Ga}^+$  ions and (b) the coating cross section. Different parts of the sample are labeled with text.

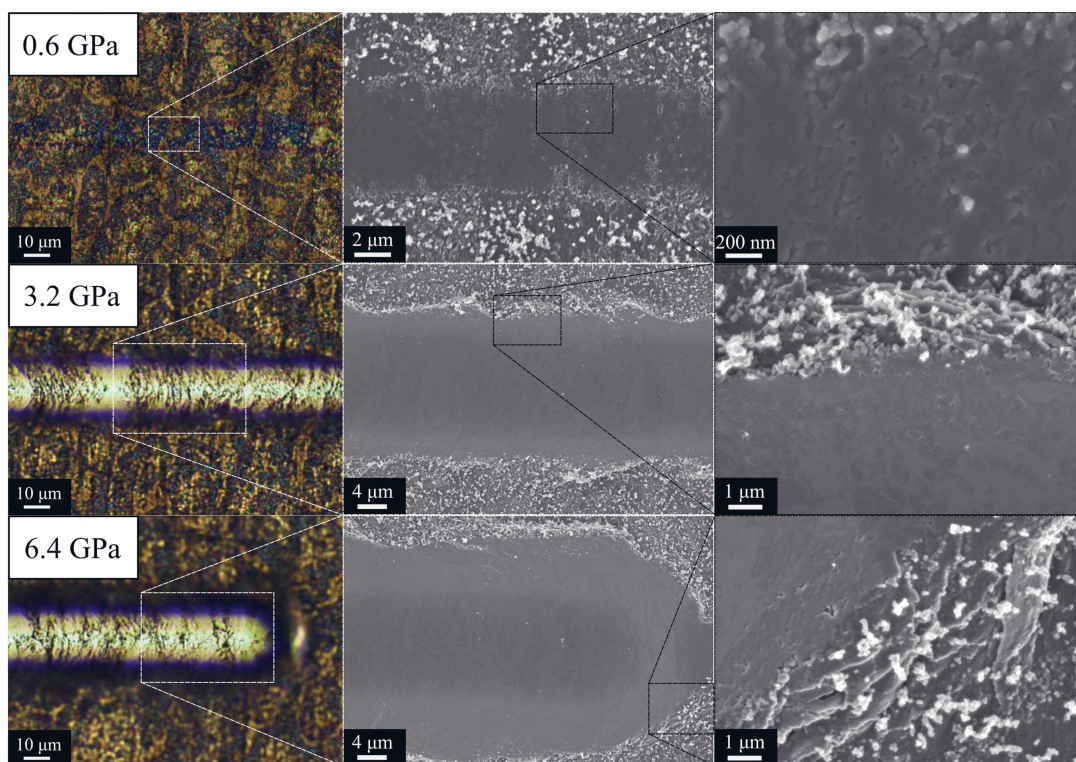


**Figure 7.** Optical and FESEM images of the scratch made in microscratch testing. The pressure values were calculated by dividing the normal force with the projected area of the diamond tip. The contact pressures refer to normal loads of 0.1, 0.5, and 1 N.

half of the circle area contributes to the real pressure values, since the rear half of the moving tip does not come in contact with the surface. The lowest reported pressure value is definitely lower than the actual average value, because the whole tip area has not come in contact with the surface due to low penetration, thus underestimating the average pressure.

Already with the lowest pressures, a clear scratch groove formed. In the groove, the surface smoothed and the roughness was lost, which is generally detrimental for effective omniphobicity. This implies that the coating is not especially durable against mechanical pressing or abrasion.

However, it seems that the coating material is not really detaching from the substrate, but rather just flattening under pressure. The FESEM images with the highest magnifications show the squashed nanoparticle agglomerates on the track of the diamond tip. Based on this observation, the adhesion of the particles to the substrate can be considered fairly good. The mechanical stability could possibly be enhanced by promoting the interparticle cohesion or by choosing a harder nanoparticle material. However, the latter option could further weaken the layer, if the cohesion between the particles in the agglomerates is lowered.

As the normal force was increased, the bottom of the scratch smoothed down further and the substrate material started piling up on the edges. Deducing from the lower pressure parts of the scratch, the particles formed a very thin layer on the bottom of the scratch. The pile-up did not seem to affect the coating topography on the edges significantly, but mostly just shape the underlying substrate. Since the coating is extremely thin, no cracking or delamination occurred, which can also be a sign of the particle agglomerates not being very strongly interconnected to each other, but rather just attached to the substrate. In a way, this fulfills the goal, because we were attempting to minimize the amount of material used in producing the favorable surface structure and chemistry. All in all, the surface topography that is necessary for an efficient omniphobicity is lost too easily for the coating to be suitable for applications experiencing moderate to high wear. If weaker repellency would be adequate, the thicker ALD layer could help with this problem.

The measurements performed during the scratching did not reveal anything very surprising. There was no acoustic emission throughout the scratching process, and the coating had no notable effect on the penetration depth of 5  $\mu\text{m}$  into the stainless steel substrate. The measured friction coefficient, reaching the end value of 0.35, seemed to oscillate a little in the beginning, possibly due to the coating topography and reorganizing of its surface structure, but this should have no significant effect on any properties we were interested in regarding this study.

## Conclusions

We fabricated a new type of superomniphobic coating on stainless steel, consisting of three nanolayers. First, a  $\text{TiO}_2$  nanoparticle layer was deposited on a cleaned steel substrate by LFS with a residence tube added to the experimental setup. The nanoparticle layer was then reinforced with a thin layer of  $\text{Al}_2\text{O}_3$  produced with ALD, and the surface was lastly covered with fluorosilane molecules in a liquid phase deposition process. The topographical and chemical structures were characterized with SEM and XPS methods. The analyses showed that underlying nanoparticles determined the physical surface structure, whereas the silanization dominated the surface chemistry. The ALD process produced an extremely uniform and conformal 10 nm thick middle layer, thus having no significant impact on the surface structure. Based on the literature we found on the subject, the multilayered coating was thinner than any superomniphobic coating reported so far, with a calculated average thickness of about 70 nm. The final coating expressed strong omniphobicity, forming CAs greater than  $150^\circ$  for DI water, DIM, EG, and OO, with SAs below  $5^\circ$  for the first three of the mentioned test liquids. The adhesion between the coating material and the substrate seemed reasonably good based on microscratch testing, but the surface structure could not stand much pressure without losing the roughness that is essential for an effective omniphobicity.

If this combination of methods were to be used for a practical application, the parameters would have to be tuned for the specific application, while making a compromise between the repellency and the mechanical stability. This is caused by the effect of ALD thickness on both of these properties. Producing a thicker layer of  $\text{Al}_2\text{O}_3$  enhances the durability of the coating, simultaneously weakening the repellency. In the future, combinations of other materials utilizing a similar structure could be also studied.



## Acknowledgments

The work was performed within the DIMECC HYBRIDS (Hybrid Materials) program. We are grateful to Fiskars Finland Oy Ab for providing the stainless steel substrates used in this study. We would also like to thank Prof Minnamari Vippola from Materials Science at TUT for interpreting some of the results.

### Funding sources

We want to acknowledge the financial support of the Finnish Funding Agency for Innovation (Tekes, grant number 1236/13) and all of the participating companies. Janne Haapanen acknowledges financial support from the Academy of Finland, project 'Nanostructured large-area antibacterial surfaces (nLABS, grant no 278 846).' The study was funded by the Finnish Funding Agency for Innovation (Tekes, grant 1236/13). Some of the work hours were funded from a project by the Academy of Finland.

## ORCID iDs

Miika Sorvali  <https://orcid.org/0000-0003-2697-4922>  
 Jyrki M Mäkelä  <https://orcid.org/0000-0002-6757-35>

## References

- [1] Bhushan B and Jung Y C 2011 Natural and biomimetic artificial surfaces for superhydrophobicity, self-cleaning, low adhesion, and drag reduction *Prog. Mater. Sci.* **56** 1–108
- [2] Sun T, Feng L, Gao X and Jiang L 2005 Bioinspired surfaces with special wettability *ACC Chem. Res.* **38** 644–52
- [3] Antonini C, Villa F, Bernagozzi I, Amirfazli A and Marengo M 2013 Drop rebound after impact: the role of the receding contact angle *Langmuir* **29** 16045–50
- [4] Ellinas K, Tserepi A and Gogolides E 2011 From superamphiphobic to amphiphilic polymeric surfaces with ordered hierarchical roughness fabricated with colloidal lithography and plasma nanotexturing *Langmuir* **27** 3960–9
- [5] Tuteja A, Choi W, Mabry J M, Mckinley G H and Cohen R E 2008 Robust omniphobic surfaces *PNAS* **105** 18200–5
- [6] Liu T and Kim C-J 2014 Turning a surface superrepellent even to completely wetting liquids *Science* **346** 1096–100
- [7] Lai Y-K, Tang Y-X, Huang J-Y, Pan F, Chen F, Zhang K-Q, Fuchs H and Chi L-F 2013 Bioinspired  $\text{TiO}_2$  nanostructure films with special wettability and adhesion for droplets manipulation and patterning *Sci. Rep.* **3** 3009

- [8] Genzer J and Efimenko K 2006 Recent developments in superhydrophobic surfaces and their relevance to marine fouling: a review *Biofouling* **22** 339–60
- [9] Brown P S and Bhushan B 2015 Mechanically durable, superomniphobic coatings prepared by layer-by-layer technique for self-cleaning and anti-smudge *J. Colloid. Interface Sci.* **456** 210–8
- [10] Ge D, Yang L, Wang C, Lee E, Zhang Y and Yang S 2015 A multi-functional oil-water separator from a selectively pre-wetted superamphiphobic paper *Chem. Commun.* **51** 6149–52
- [11] Wang N, Zhu Z, Sheng J, Al-Deyab S S, Yu J and Ding B 2014 Superamphiphobic nanofibrous membranes for effective filtration of fine particles *J. Colloid. Interface Sci.* **428** 41–8
- [12] Lee C and Kim C-J 2011 Underwater restoration and retention of gases on superhydrophobic surfaces for drag reduction *Phys. Rev. Lett.* **106** 014502
- [13] Vahabi H, Wang W, Movafaghi S and Kota A K 2016 Free-standing, flexible, superomniphobic films *ACS Appl. Mater. Interfaces* **8** 21962–7
- [14] Vahabi H, Wang W, Davies S, Mabry J M and Kota A K 2017 Coalescence-induced self-propulsion of droplets on superomniphobic surfaces *ACS Appl. Mater. Interfaces* **9** 29328–36
- [15] Jin C, Li J, Han S, Wang J and Sun Q 2014 A durable, superhydrophobic, superoleophobic, and corrosion-resistant coating with rose-like ZnO nanoflowers on a bamboo surface *Appl. Surf. Sci.* **320** 322–7
- [16] Wenzel R N 1936 Resistance of solid surfaces to wetting by water *Ind. Eng. Chem.* **28** 988–94
- [17] Cassie A B D and Baxter S 1944 Wettability of porous surfaces *Trans. Faraday Soc.* **40** 546–51
- [18] Wang W, Salazar J, Vahabi H, Joshi-Imre A, Voit W E and Kota A K 2017 Metamorphic superomniphobic surfaces *Adv. Mater.* **29** 1700295
- [19] Vahabi H, Wang W, Popat K C, Kwon G, Holland T B and Kota A K 2017 Metallic superhydrophobic surfaces via thermal sensitization *Appl. Phys. Lett.* **110** 251602
- [20] Ganesh V A, Dinachali S S, Nair A S and Ramakrishna S 2013 Robust superamphiphobic film from electrospun TiO<sub>2</sub> nanostructures *ACS Appl. Mater. Interfaces* **5** 1527–32
- [21] Jiang D, Fan P, Gong D, Long J, Zhang H and Zhong M 2016 High-temperature imprinting and superhydrophobicity of micro/nano surface structures on metals using molds fabricated by ultrafast laser ablation *J. Mater. Process. Tech.* **236** 56–63
- [22] Kumar R T R, Mogensen K B and Bøggild P 2010 Simple approach to superamphiphobic overhanging silicon nanostructures *J. Phys. Chem. C* **114** 2936–40
- [23] Li H and Yu S 2016 A stable superamphiphobic Zn coating with self-cleaning property on steel surface fabricated via a deposition method *J. Taiwan Inst. Chem. E* **63** 411–20
- [24] Muthiah P, Bhushan B, Yun K and Kondo H 2013 Dual-layered-coated mechanically-durable superomniphobic surfaces with anti-smudge properties *J. Colloid Interface Sci.* **409** 227–36
- [25] Chen K, Wu Y, Zhou S and Wu L 2016 Recent development of durable and self-healing surfaces with special wettability *Macromol. Rapid Commun.* **37** 463–85
- [26] Motlagh N V, Birjandi F C, Sargolzaei J and Shahtahmassebi N 2013 Durable, superhydrophobic, superoleophobic and corrosion resistant coating on the stainless steel surface using a scalable method *Appl. Surf. Sci.* **283** 636–47
- [27] Li H, Yu S and Han X 2016 Fabrication of CuO hierarchical flower-like structures with biomimetic superamphiphobic, self-cleaning and corrosion resistance properties *Chem. Eng. J.* **283** 1443–54
- [28] Li H and Yu S 2016 Facile fabrication of micro-nano-rod structures for inducing a superamphiphobic property on steel surface *Appl. Phys. A* **122** 30
- [29] Tesler A B, Kim P, Kolle S, Howell C, Ahanotu O and Aizenberg J 2015 Extremely durable biofouling-resistant metallic surfaces based on electrodeposited nanoporous tungstite films on steel *Nat. Commun.* **6** 8649
- [30] Dafinone M I, Feng G, Brugarolas T, Tettey K E and Lee D 2011 Mechanical reinforcement of nanoparticle thin films using atomic layer deposition *ACS Nano* **5** 5078–87
- [31] Zhang L, Prosser J H, Feng G and Lee D 2012 Mechanical properties of atomic layer deposition-reinforced nanoparticle thin films *Nanoscale* **4** 6543–52
- [32] Zhang D, Zhang L, Lee D, Cheng Z and Feng G 2015 Reinforcing nanocolloidal crystals by tuning interparticle bonding via atomic layer deposition *Acta Mater.* **95** 216–23
- [33] Wong W S Y, Liu G, Nasiri N, Hao C, Wang Z and Tricoli A 2017 Omnidirectional self-assembly of transparent superoleophobic nanotextures *ACS Nano* **11** 587–96
- [34] Lide D R 2007 *CRC Handbook of Chemistry and Physics* 88th edn (Boca Raton, FL: CRC Press, Taylor & Francis Group)
- [35] Körösi G and Kováts E S 1981 Density and surface tension of 83 organic liquids *J. Chem. Eng. Data* **26** 323–32
- [36] Jones A Z Surface Tension—Definition and Experiments. *Thought Co* Mar. 13, 2017, <http://thoughtco.com/surface-tensiondefinition-and-experiments-2699204>
- [37] Mäkelä J M, Haapanen J, Harra J, Juuti P and Kujanpää S 2017 Liquid flame spray—a hydrogen-oxygen flame based method for nanoparticle synthesis and functional nanocoatings *KONA Powder Part. J.* **34** 141–54
- [38] Tikkanen J, Gross K A, Berndt C C, Pitkänen V, Keskinen J, Raghu S, Rajala M and Karthikeyan J 1997 Characteristics of the liquid flame spray process *Surf. Coat. Technol.* **90** 210–6
- [39] Mäkelä J M, Keskinen H, Forsblom T and Keskinen J 2004 Generation of metal and metal oxide nanoparticles by liquid flame spray process *J. Mater. Sci.* **39** 2783–8
- [40] Pitkänen A, Mäkelä J M, Nurminen M, Oksanen A, Janka K, Keskinen J, Keskinen H, Liimatainen J K, Hellstén S and Määttä T Numerical study of silica particle formation in turbulent H<sub>2</sub>/O<sub>2</sub> flame *IFRF Combust. J.* **2005** 200509
- [41] Aromaa M, Keskinen H and Mäkelä J M 2007 The effect of process parameters on the liquid flame spray generated titania nanoparticles *Biomol. Eng.* **24** 543–8
- [42] Keskinen H, Aromaa M, Heine M-C and Mäkelä J M 2008 Size and velocity measurements in sprays and particle producing flame sprays *Atomization Sprays* **18** 1–26
- [43] Teisala H, Tuominen M, Aromaa M, Mäkelä J M, Stepien M, Toivakka M and Kuusipalo J 2010 Development of superhydrophobic coating on paperboard surface using the liquid flame spray *Surf. Coat. Technol.* **205** 436–45
- [44] Tuominen M, Teisala H, Aromaa M, Stepien M, Mäkelä J M, Saarinen J J, Toivakka M and Kuusipalo J 2014 Creation of superhydrophilic surfaces of paper and board *J. Adhes. Sci. Technol.* **28** 864–79
- [45] Miikkulainen V, Leskelä M, Ritala M and Puurunen R 2013 Crystallinity of inorganic films grown by atomic layer deposition: overview and general trends *J. Appl. Phys.* **113** 021301
- [46] Elliott S D, Dey G, Maimaiti Y, Ablat H, Filatova E A and Fomengia G N 2016 Modeling mechanism and growth reactions for new nanofabrication processes by atomic layer deposition *Adv. Mater.* **28** 5367–80
- [47] Vuori L, Hannula M, Lahtonen K, Jussila P, Ali-Löytty H, Hirsimäki M, Pärna R, Nömmiste E and Valden M 2014 Controlling the synergetic effects in (3-aminopropyl) trimethoxysilane and (3-mercaptopropyl) trimethoxysilane coadsorption on stainless steel surfaces *Appl. Surf. Sci.* **317** 856–66

- [48] Vuori L, Leppiniemi J, Hannula M, Lahtonen K, Hirsimäki M, Nömmiste E, Costelle L, Hytönen V P and Valden M 2014 Biofunctional hybrid materials: bimolecular organosilane monolayers on FeCr alloys *Nanotechnology* **25** 435603
- [49] Kilpi L, Ylivaara O M E, Vaajoki A, Malm J, Sintonen S, Tuominen M, Puurunen R L and Ronkainen H 2016 Microscratch testing method for systematic evaluation of the adhesion of atomic layer deposited thin films on silicon *J. Vac. Sci. Technol. A* **34** 01A124
- [50] Fairley N 2009 CasaXPS: Spectrum Processing Software for XPS, AES and SIMS (Version 2.3.16). *Casa Software Ltd Cheshire SK9 6N, UK* (<http://casaxps.com/>)
- [51] Mayon Y O, Duong T, Nasiri N, White T P, Tricoli A and Catchpole K R 2016 Flame-made ultra-porous TiO<sub>2</sub> layers for perovskite solar cells *Nanotechnology* **27** 505403
- [52] Jussila P, Ali-Löytty H, Lahtonen K, Hirsimäki M and Valden M 2010 Effect of surface hydroxyl concentration and morphology of aminopropylsilane thin films on austenitic stainless steel *Surf. Interface Anal.* **42** 157–64
- [53] Yang J, Kim S, Choi W, Park S H, Jung Y, Cho M-H and Kim H 2013 Improved growth behavior of atomic-layer-deposited high-k dielectrics on multilayer MoS<sub>2</sub> by oxygen plasma pretreatment *ACS Appl. Mater. Interfaces* **5** 4739–44





